Reliability Analysis of Modular Multilevel Converter for Offshore Wind Power Transmission Systems

Liu, Hui

DOI (link to publication from Publisher):
10.5278/vbn.phd.engsci.00105

Publication date:
2016

Document Version
Publisher's PDF, also known as Version of record

RELIABILITY ANALYSIS OF MODULAR MULTILEVEL CONVERTER FOR OFFSHORE WIND POWER TRANSMISSION SYSTEMS

BY
HUI LIU

DISSERTATION SUBMITTED 2016

AALBORG UNIVERSITY
DENMARK

Reliability Analysis of Modular Multilevel Converter for Offshore Wind Power Transmission Systems

by

Hui Liu

A Dissertation Submitted to
the Faculty of Engineering and Science at Aalborg University
for the Degree of Doctor of Philosophy in Electrical Engineering

AALBORG UNIVERSITY
DENMARK

2016
Denmark

Dissertation submitted: May 2016

PhD supervisor: Professor Frede Blaabjerg
Aalborg University

Assistant PhD supervisor: Professor Poh Chiang Loh

PhD committee: Professor Zhe Chen (chairman)
Aalborg University

Professor Hui ”Helen” Li
Florida State University

Professor Rosario Miceli
University of Palermo

PhD Series: Faculty of Engineering and Science, Aalborg University

ISSN (online): 2246-1248
ISBN (online): 978-87-7112-567-2

Published by:
Aalborg University Press
Skjernvej 4A, 2nd floor
DK – 9220 Aalborg Ø
Phone: +45 99407140
aauf@forlag.aau.dk
forlag.aau.dk

Printed in Denmark by Rosendahls, 2016

Public Defence of PhD Dissertation

Thesis Title:
Reliability Analysis of Modular Multilevel Converter for Offshore Wind Power Transmission Systems

Ph.D. Defendant:
Hui Liu

Supervisor:
Prof. Frede Blaabjerg

Co-supervisor:
Prof. Poh Chiang Loh

Assessment Committee:
Professor Zhe Chen (Chairman)
Department of Energy Technology
Aalborg University
Pontoppidanstraede 101
9220 Aalborg, Denmark

Professor Hui "Helen" Li,
Electrical and Computer Engineering Department, FAMU-FSU College of Engineering
Florida State University
2525 Pottsdamer Street, Tallahassee, Florida 32310, US

Professor Rosario Miceli,
Department of Electrical, Electronics and Telecommunication Engineering, Chemistry, Automation and Mathematical Modeling
University of Palermo
Viale delle Scienze 90128, Palermo, Italy

Defence Date and Place:
Thursday, June 16, 2016
Pontoppidanstræde 111, auditorium, Aalborg University

Copyright Statements

Acknowledgement

This thesis is a summary of the PhD project "Reliability Analysis of Modular Multilevel Converter for Offshore Wind Power Transmission Systems". The research work is supported by China Scholarship Council (CSC). Acknowledgements are given to the institution as well as the Department of Energy Technology which supported me for conference participation and study abroad. Special thanks to Mr. Chenggang Liu and Yun Zhang from the Embassy of The People's Republic of China in The Kingdom of Denmark for their kind support and tremendous help.

This research project was carried out under the supervision of Prof. Frede Blaabjerg and Prof. Poh Chiang Loh from the Department of Energy Technology, Aalborg University, Denmark. First and foremost, I would like to show my deepest gratitude to my supervisor, Prof. Frede Blaabjerg, for his professional and constructive guidance with his open-mindedness and earnestness during the PhD project. His encouragement supported me to get through the difficulties during the project one by one. His guidance not only help me to complete my PhD project but also deeply influence my research style, which I do believe will continuously support me in my career and through my future life. I would also show my appreciation to my co-supervisor, Prof. Poh Chiang Loh, for his patient guidance, fruitful discussion and paper revision. Thank Dr. Ke Ma for his passionate care to my project.

I would take this opportunity to thank Prof. Luis Romeral for his support during my study abroad in the Center of Motion Control and Industrial Applications (MCIA), University of Catalonia, Barcelona, Spain. The thanks will also go to the colleagues in MCIA-UPC, especially Mr. Tomas Michalski, Mr. Anderson Machado, and Dr. Vicent Sala, for their kind assistance.

I also want to thank all my colleagues from the Department of Energy Technology for the warm environment.. Thank Dr. Xiongfei Wang, Dr. Yongheng Yang, Dr. Dao Zhou and Dr. Zian Qin, for their kind help to my project. Best wishes to my friends – Min Huang, Dan Wu, Zian Qin, Helong Li, Jie Gong, Pinting Lin and all the other friends. We enjoyed the parties, Spring Festival and many other activities together. The life hence became more interesting and colorful. My appreciations are extended to John K. Pedersen, Tina Larsen, Corina Busk Gregersen, Eva Janik and Casper Jørgensen for their assistance in different ways.

The sincerest gratitude goes to my parents, my brother and sister in law for their endless love and support. Finally, my love is given to my son, who brings so much happiness to my life.

Hui Liu
March 5, 2016
Aalborg East

Abstract

Modular Multilevel Converter based High Voltage Direct Current (MMC-HVDC) configuration is a promising solution for renewable energy transmission. However, the large number of power electronic components in the MMC may increase the probability of failures and lower the reliability of the whole MMC system. Therefore, researches on the loading conditions, lifetime, failure mechanism, and fault diagnosis of MMC are of great importance for the reliability improvement. The focus of this thesis is dedicated to provide reliability analysis of MMC in the above mentioned aspects, some more practical mission profiles including the typical grid faults conditions will be considered.

The content of this thesis is organized as follows: Chapter 1 presents the introduction and motivation of the whole project. The emerging challenges and the structure of the thesis are also introduced. The power loss, thermal performance as well as lifetime evaluation of MMC considering different wind speeds are studied in Chapter 2. The thermal performance of power devices in MMC under various grid voltage dips is presented in Chapter 3. In Chapter 4, an observer model of MMC which can be used to estimate the capacitor voltage in each module is proposed. Chapter 5 proposes a fault diagnosis method for both open-circuit fault and short-circuit fault of the semiconductors in the MMC. The thesis is finally concluded in Chapter 6, before the proposal for the future research topics in this area.

The contributions of this project from the author's point of view can be concluded as: the investigation of power loss and thermal loading of the power semiconductors in MMC under different wind speed conditions with lifetime assessment, the analysis of operating and loading status of power device in MMC under different grid faults, the study of a robust fault diagnostic method for MMC.

Abstrakt

Modular Multi-level Converter baserede High Voltage Direct Current (MMC-HVDC) systemer er en lovende løsning for transmissionen af en stor mængde vedvarende energi og mere effektiv el-net integration over en lang distance. MMC-HVDC indebærer en væsentlig forøget antal effektelektroniske komponenter, som kan øge sandsynligheden for fejl og give lavere pålidelighed af hele MMC-HVDC systemet. Derfor er studier af belastningsforhold, levetid, fejl mekanismer, og fejldiagnose af MMC af betydning for at øge pålideligheden af energiomsætningen generelt. Fokus i denne afhandling er dedikeret at bidrage med nogle pålideligheds analyser af MMC-HVDC systemer fra de ovennævnte aspekter, især MMC-HVDC systemets belastning herunder de typiske net-fejl vil blive undersøgt.

Indholdet af denne afhandling er organiseret som følger: Kapitel 1 præsenterer en indførelse i og motivation for hele projektet, diskuterer de nye udfordringer med vedvarende energi, og også introducerer også strukturen i afhandlingen. Effekt-tab, termisk ydeevne samt levetids evaluering af MMC undersøges i kapitel 2 ved forskellige vindhastigheder baseret på effekttab og termisk cykling af effektkomponenterne, og den termiske ydeevne i MMC under forskellige net-spændingsdyk præsenteres i kapitel 3. I kapitel 4, er en observer model af MMC foreslået, som kan anvendes til at estimere kondensator spænding i hvert enkelt modul med anvendelse af et reduceret antal sensorer. Kapitel 5 foreslår en fejldiagnose metode i MMC-HVDC til både at detektere åbne kredsløbs-fejl og kortslutnings-fejl af halvlederkomponenter i MMC omformeren. Afhandlingen afsluttes i kapitel 6 med nogle konklusioner på analyserne, samt giver forslag til de fremtidige forskningsemner indenfor området.

Bidragene fra dette projekt kan konkluderes til at være: Gennemgang af eksisterende fejl diagnose metoder til de effektelektroniske enheder i MMC omformeren; Undersøgelse af effekttab og termisk belastning af effekt-halvlederne i MMC under forskellige vindhastigheder inklusiv en levetidsvurdering; Analyse af drifts- og belastning forhold af de effektelektroniske enheder i MMC under forskellige net-fejl og undersøgelse af en robust fejldiagnosticering og fejllokalisering strategi for MMC, som overordnet set kan gøre omformeren mere pålidelig.

Contents

1 Introduction

This chapter presents the background and motivation of this research project. It also includes a short state-of-the-art of the MMC technologies and research topics, followed by the objectives and limitations of this PhD thesis. Afterwards the structure of this thesis is presented to give a better understanding about the flow of this research work. All the publications related to this work are listed at the end of this chapter.

1.1 Background

Wind energy, like other forms of energy based on renewable resources, is widely available throughout the world and can contribute to the reduction of the energy-import dependence for many countries. As it entails no fuel price risk or constraints, it may also improve the security of power supply. Additionally, wind power does not emit pollutants.

Offshore wind power possess many advantages such as stronger and more stable wind, fewer disturbance and larger capacity factor, which make the expansion of wind power plant from onshore to offshore particularly attractive for countries with coastal areas, such as China, several European countries and the US, where larger and larger offshore wind energy installation capacity is achieved, as shown in Fig. 1.1 [1-4].

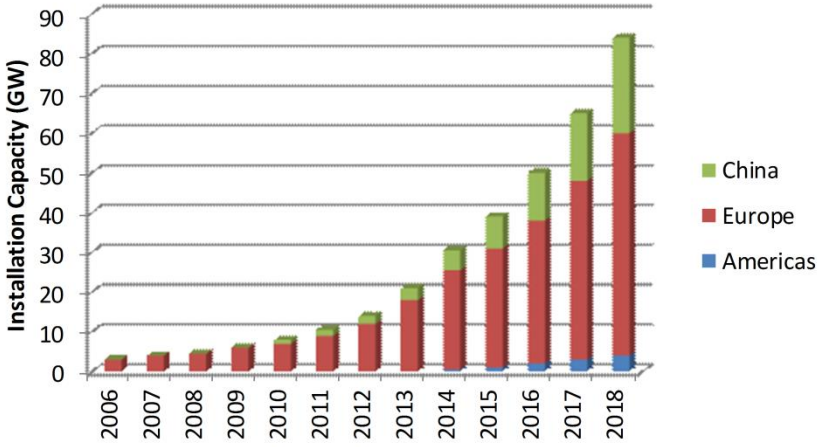

Fig. 1.1. Offshore wind energy installation capacity world-wide share in 2013 [4].

Nevertheless, the high installation and generation level of offshore wind power imposes new challenges to the power conversion and transmission as the existing energy conversion and transmission system is low voltage rating and low efficiency. MMC-HVDC systems, which offer a series of merits over other existing transmission systems such as higher voltage rating levels and high efficiency, are gradually replacing the traditional transmission technology in connecting offshore wind power plants located at longer distances from suitable connection points in the transmission grids. Recently, many projects based on MMC-HVDC have been established or are planned and some of them are summarized in Table 1.1 [5-16] in the Appendix, where the key features like location, power and voltage ratings, cable types, commission time as well as manufacturers are shown. However, due to the high maintenance/repair cost at the distant offshore plant, the reliability has become one of the challenges for MMC systems, where generally a large number of power switching devices are used and each of these devices may be considered as a potential failure site, especially under harsh operating conditions. Therefore, research on the reliability analysis for MMC systems is of great significance and of practical engineering value.

1.2 State of the art of reliability research on MMC

Recently, literatures related to the reliability of MMC are focused on the control strategies [17-24], sub-module topologies with fault ride-through capability [25-30] and different kinds of control approaches under AC grid faults or DC bus faults [31-44]. However, the emphasis of them is put on the control methods under normal conditions or external faults, while research on the internal failures of devices in MMC is rare. Therefore, this project mainly focuses on the loading/lifetime estimation of the devices and internal fault diagnosis of the MMC system, where the high voltage power conversion of offshore wind farm will be the application.

1.2.1 Overview of lifetime estimation of switching devices in MMC

According to the statistics carried by [45], the proportion of various stresses that contribute to the lifetime of power electronic components is shown in Fig. 1.2. It can be seen that there are 55% of the component failures caused by the temperature or thermal stress due to the Thermal Expansion Coefficient (CTE) mismatch between adjacent layers in the power semiconductor modules. Power loss variation of the converter will lead to temperature cycling in the device, and the temperature cycling may affect the connections between the layers. When the power cycling and temperature cycling come to a certain number, the layer connection will wear out [46-50], which means the device comes to the end of lifetime. Unlike other types of converters, the semiconductors in the MMC bear different stress and have different

thermal cycling, correspondingly suffer various lifetimes which are quite meaningful for the guide-lines of heatsink design and maintenance. In this project, the thermal loading and lifetime of the different semiconductors of the MMC are investigated.

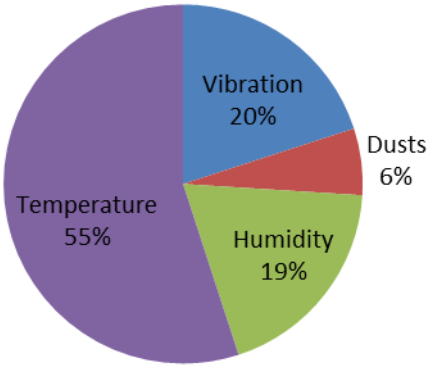

Fig. 1.2. Critical stresses contribute to the failures of power electronic components [45].

It has been proved that the thermal stress and lifetime of IGBT modules can be mathematically correlated, as summarized in [51-54], where a series of lifetime models are introduced. Normally the parameters of these lifetime models need to be acquired experimentally by accelerating or aging tests, in which the power devices are running at various thermal loadings and the failures are observed and recorded. Afterwards some mathematical functions which are able to transfer certain thermal cycling of components into the corresponding lifetime information [15, 16, 55, 56] are used to fit these recoding points e.g. Coffin-Masson model [53].

1.2.2 Overview of fault diagnosis of switching devices in MMC

Once the semiconductor fails due to the end of lifetime or other reasons, the faulty semiconductor should be detected as soon as possible in order to avoid damage to other parts in the MMC system where the diagnosis and localization of the faulty sub-module is difficult due to large number of used series-connected identical modules [57-62]. There have been some researches related to this topic, as introduced in the follows:

The most original method is sending the sampled signals such as device current, device voltage as well as gating signals to the system operators who detect faults by observing and analyzing those signals [23]. The faulty sub-module can be localized at the same time However, the needed detection and localization time as well as the

detection and diagnosis accuracy of this method heavily depends on the experience of the operators which makes the expansion of the method to other project is difficult.

To make the fault detection and fault diagnosis method easy to be extended and transplanted to other applications, those methods with obvious fault features or detecting faults automatically are proposed.

In [63], the value of the switching frequency component of the output phase voltage is monitored to judge if the system operation condition is normal or not. This method is based on the principle that the magnitude of the switching frequency harmonics of the output phase voltage becomes larger after the occurrence of a fault due to the unbalanced cancellation of the switching frequency harmonics. Then the faulty cell can be located according to the angle of the switching frequency component of the output phase voltage. However, this method is complex to implement and it is easy to obtain a wrong diagnosis in the transient operation due to the small angle difference of the switching frequency component of the output phase voltage, especially when there is large number of modules. Moreover, the faulty switching device cannot be located in this method. In [64], the abnormal operation is detected by monitoring the root mean square value of the output phase voltage, then the faulty cell and faulty switch is detected by comparing the real output voltage with the pretended faulty switch output voltage. However, it is not accurate enough as the same root mean square value of the output phase voltage may be caused by different faults.

A Sliding Mode Observer (SMO) based fault detection method for MMC is proposed in [65] which detects whether the MMC was operating normally or not by monitoring the differences between the observed arm current values. If the difference exceeds the predefined threshold values and lasts for a certain period, the abnormal system is reported. Once the system is abnormal, the sub-modules are replaced one by one by the redundant sub-module and the arm current was observed at the same time. If the arm current tracks the normal wave, the corresponding sub-module has a fault. The inaccuracy of this method can be avoided only with very precise MMC model, which may be difficult to achieve. Through the comparison between the measured state value and the estimated state value by Kalman Filter (KF), the open-circuit fault in the MMC can be detected [66]. Then the faulty sub-module can be determined if the error between the capacitor voltage in this sub-module and the minimum capacitor voltage is larger than a predefined threshold. This method is time-saving. However, the short-circuit fault cannot be detected in this method. In [67] and [68], Fast Fourier Transform (FFT) is used to extract features from the output phase voltage and the Genetic Algorithm optimized

Principle Component Neural Network (PC-GA-NN) is proposed to detect the faulty module. In [69], the output voltage is transformed by Discrete Fourier Transform (DFT) to select the main harmonic information which is then used to train the Back Propagation Neural Network (BPNN). After that, the fault identification task is performed by the trained BPNN. In [70], the NN is used to diagnose open-circuit and short-circuit faults of the switches in the MMC. It was emphasized that if an open-circuit fault occurred in one of the switches, the output phase voltage would be affected and one of the voltage levels would be missed. Meanwhile, when a short-circuit fault occurred, the peak of the phase current increased to about 1.5 times of the normal operation. Based on this mechanism, the output phase voltages were used to detect the system operation condition. Then the faulty cell and faulty switch can be detected based on the principle that the output voltage has different numbers in different cycles under the faulty condition. The detection time by using this approach is as long as one fundamental period which is too long in order to isolate fault, especially for the short-circuit fault. The major drawback of the NN is the long training time for all the fault conditions.

To avoid those drawbacks, fault diagnosis and fault localization method with high accuracy and high efficiency is urgent considering both fault diagnosis time as well as cost.

1.3 Project motivation

1.3.1 Configuration of MMC system for study

A two-terminal AC network connected offshore wind energy transmission system which consists of farm-side converter, grid-side converter and power transmission lines is chosen as a case study in this project, as shown in Fig. 1.3. Both the farm-side converter and the grid-side converter employ three-phase MMC. The DC link voltage in this system is maintained by the sum of sub-module voltages in the converter leg and there is no bulky DC link capacitor as in the other type of VSC-HVDC systems [71, 72].

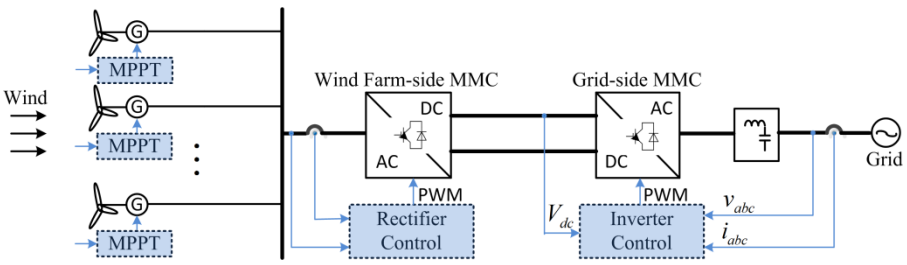

Fig. 1.3. Wind power transmission system with MMC.

MMC is elementarily assembled by connecting multiple power electronic arms together to form a three-phase converter. Each arm is, in turn, formed by several series-connected sub-modules built with power electronics components such as Insulated Gate Bipolar Transistors (IGBTs), diodes and capacitors. In series with each arm is an inductor for filtering the switching harmonics. Depending on how the arms are configured, different MMC topologies can be derived like the single-star, single-delta and double-star configurations [55, 56].

Additionally, depending on the demanded output waveform and cost, the configuration of each sub-module can also be different [73, 74]. Two examples are half-bridge and full-bridge topologies.

In this project, the double-star and half-bridge configuration as shown in Fig. 1.4(a) and (b), respectively, are used. In this topology, the three phases are parallel with the DC source and each phase consists of two arms which are comprised by series-connected half-bridge Sub-Modules (SM). The half-bridge sub-module contains two IGBTs S_1, S_2, two diodes D_1, D_2 and capacitor C.

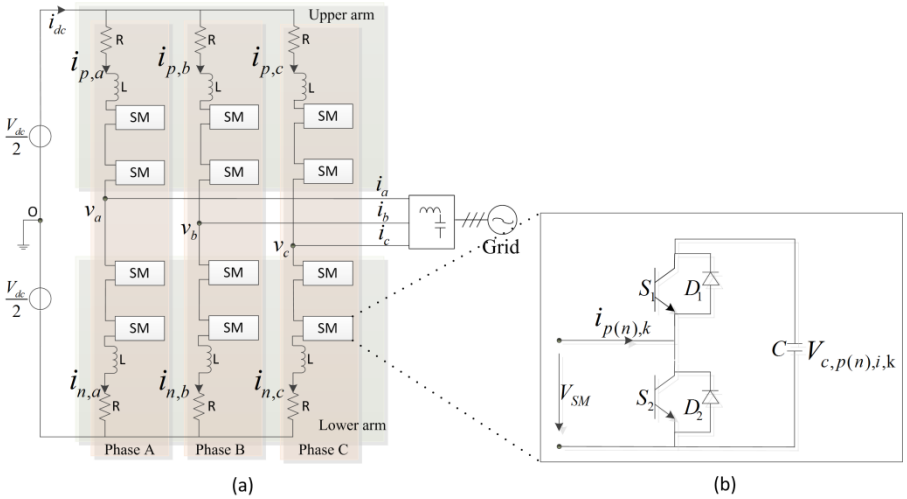

Fig. 1.4. The structure of Module Multilevel Converter (MMC) (a) structure of MMC; (b) structure of half-bridge sub-module.

1.3.2 Project motivation

With more national objectives which have been initiated to solve the emerging energy crisis, more distributed generation systems, especially offshore wind power generation system employing MMC are installed as listed in Table 1.1 in Appendix. As a result, the reliability of the MMC needs to be high in order to decrease the cost of maintenance, and thereby further lower the cost of energy.

According to a survey as presented in Fig. 1.5 [75], the probability of failure of the power devices is 31 %, while the capacitor is in the second one with 21 %. The probability of failure of the driving units is 18 % and the probability of control & protection units fail is much less which is 8 %. Other devices such as inductors and resistors have a lower chance to fail. It can be seen that the power device has been the most failure-happened and life-limited components in the MMC system. Therefore, the emphasis of this thesis will be focused on the power devices in the MMC to help improving the reliability of MMC.

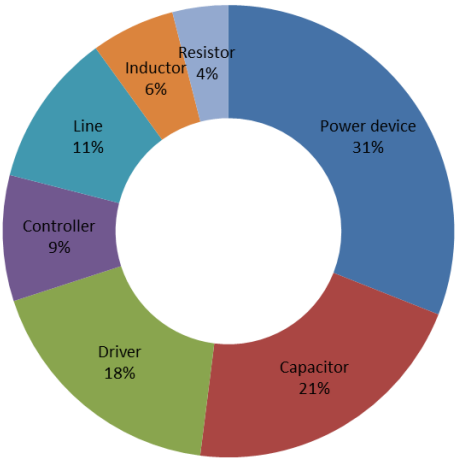

Fig. 1.5. Failure rate overview of MMC per year [75].

If the power devices come to the end of life or experience any kind of fault, they are expected to be detected, diagnosed and localized as early and fast as possible in order to reduce the maintenance time and avoid damage to other parts in the MMC system. It is also expected that the fault diagnosis method can effectively and precisely locate the faulty modules and faulty power devices, even under multiple module fault situation without increasing the implementation complexity. It is important that the diagnosis method should be valid under all kinds of driving signal generating methods and system control strategies, even under some external disturbances and fault situations in order to avoid false diagnosis.

Therefore, the emphasis of this thesis is focused on two parts which are related to the reliability of MMC systems: the loss distribution, thermal loading and lifetime of the different semiconductors of the MMC are investigated in order to provide guide-lines for heatsink design and schedule maintenance; additionally, the fault analysis, electrical model and mathematical model establishment, fault feature extraction are conducted in order to diagnose different power device faults. The analysis results can

be used to maintain normal operation of the MMC, to evaluate the health status and reliability of the MMC and also to improve the design.

1.4 Research objectives and limitations

1.4.1 Research questions and objectives

In order to study the reliability of MMC for offshore wind energy transmission systems when different mission profiles are taken into consideration, the following challenges need to be dealt with:

How the reliability performance of the MMC is affected by internal factors such as open-circuit and short-circuit fault in different power devices?

Is there any fault diagnosis method which can detect and diagnose the faults in MMC under all conditions to improve the reliability of the MMC?

With those two main research questions, this PhD project is objected to evaluate and improve the reliability of the MMC for wind energy transmission systems considering both the mission profiles and the fluctuation of environmental factors. The primary goal of this project will be focused on the discussion of the factors that affect the lifetime of the MMC under different operation conditions, and consequently, the lifetime of the MMC will be evaluated to research its reliability. Furthermore, effective fault feature extraction methods, accurate fault diagnosis strategies will be developed considering the feasibility and cost constraint to detect and localize the faults happened in the transmission system as soon as possible.

The objectives of this project are formulated as:

1. *Lifetime estimation of MMC considering the mission profile of one year wind speed*

There are various factors affecting the lifetime of the MMC. Besides the characteristics of the semiconductor devices, the working environments along with the mission profiles of the converters are also important factors. Therefore, the working conditions of the MMC for wind power application are analyzed. Then the topology of the MMC is introduced based on which the dynamic power losses are calculated. Afterwards the thermal profile in the power semiconductor devices is studied, and then the rain flow counting algorithm is applied to map the lifetime information of the MMC converter.

2. *Power loss and thermal distribution analysis under different grid faults*

This part focuses on the analysis of the loading states of power devices in the MMC-HVDC system under various LVRT conditions. The MMC operation performance under various grid faults are simulated and analytically solved. The corresponding loss distribution and thermal behavior of the power semiconductor devices when considering the LVRT are presented.

3. *Modelling of the MMC*

A non-linear state observer based on the measurement of output currents and output voltages is proposed and elaborated in order to detect faults. The necessary and sufficient condition for MMC observability verification is presented as well as gain matrix calculation is proposed for efficient calculation. No extra sensors are needed by applying this technique which not only decreases the investment but also avoids unpredictable failures of sensors and uncertainties caused by various noise sources in the system. The effectiveness and the robustness of the proposed state observer are verified under different operation profile such as the fluctuation of the transmission power, DC disturbance as well as AC disturbances.

4. *Fault detection, fault diagnosis and fault localization of the devices*

Regarding the most common sub-module faults in the MMC, the corresponding observer are analyzed which makes the estimation of the capacitor voltages possible. A fault detection, diagnosis and localization method based on state observer for both open-circuit fault, short-circuit fault, multiple faults and capacitor degradation is proposed for an MMC to improve the reliability. The proposed method can effectively and precisely locate the faulty modules and faulty switching devices, even under multiple module fault situation without increasing the implementation and calculation complexity. The method is valid under all the driving signal generating methods and system control strategies, even under various grid faults, and the threshold used to detect the fault condition in this method is stable even when fluctuations of transmission power and disturbance of DC or AC voltages are happening.

1.4.2 Project limitations

There are several MMC topologies available in the literature, but only one of them, the double-star with half bridge cell is considered in this project. The lifetime evaluation methods as well as the fault detection strategies developed in this project can be adopted for different topologies and other renewable energy systems, but minor adaptations and modifications might be necessary with a better knowledge of

the mission profiles. Only the wind speed and the grid faults are considered in this project when analyzing the thermal of the MMC. However, there are many other mission profiles like the fluctuation of ambient temperature, different modulation methods, different control strategies and so on, which should be taken into account.

Although the discussions in this project are based on a high power level of MMC systems, a relatively downscaled MMC system with the power of 18 MW is considered with a DC link voltage of 31.8 kV and sub-module number of 12 for study. All the developed control strategies are conducted in this system at this power level. The interactive effect of large-scale (maybe thousands of sub-modules per arm) aggregated MMC systems at transmission system level with a very large number of sub-modules also calls for further investigations.

1.5 List of publications

The selected publications are a collection of relevant disseminations based on this project. It includes several peer-reviewed journal papers (published or accepted) and conference contributions, as listed below:

J1. F. Blaabjerg, **H. Liu**, P. C. Loh, "Monitoring and Control of Marine Energy Generation Systems," *IEEE* ***Instrumentation & Measurement Magazine***, vol. 17, no. 2, pp. 27-32, 2014.

J2. **H. Liu**, P. C. Loh, F. Blaabjerg, "Sub-module Short Circuit Fault Diagnosis in Module Multilevel Converter based on WT and ANFIS," ***Electronic power components and systems***, 43:8-10, pp. 1080-1088, 2015.

J3. **H. Liu**, K. Ma, Z. A. Qin, P. C. Loh, F. Blaabjerg, "Lifetime Estimation of MMC for Offshore Wind Power HVDC Application," ***Journal of Emerging and Selected Topics in Power Electronics***, vol. 4, no. 2, pp. 504-511, 2016.

J4. **H. Liu**, K. Ma, P. C. Loh, F. Blaabjerg, "Online Fault Identification for Modular Multilevel Converter Based on Adaptive Observer," ***Energies***, vol. 8, no. 7, pp. 7140-7160, 2015.

J5. **H. Liu**, K. Ma, P. C. Loh, F. Blaabjerg, "Loading Analysis of Modular Multilevel Converter for Offshore HVDC Application under Various Grid Faults," ***Electronic Power Components and Systems***, 2016. (Submitted)

J6. **H. Liu**, P. C. Loh, F. Blaabjerg, "Fault Diagnosis and Fault-tolerant Control of MMC-HVDC System: A Review," ***Electronic Power Components and Systems***, 2016. (Submitted)

C1. **H. Liu**, P. C. Loh, F. Blaabjerg, "Review of Fault Diagnosis and Fault-tolerant Control for Modular Multilevel Converter of HVDC," Proc of the 39th Annual Conference of the IEEE Industrial Electronics Society (IECON), pp. 1242-1247, 2013.

C2. **H. Liu**, P. C. Loh, F. Blaabjerg, "Generalized Modular Multilevel Converter and Modulation," Proc of the International Power Electronics Conference (IPEC-Hiroshima 2014 - ECCE-ASIA), pp. 1634-1638, 2014.

C3. **H. Liu**, P. C. Loh, F. Blaabjerg, "Sub-module Short Circuit Fault Diagnosis in Modular Multilevel Converter based on WT an ANFIS," Proc of the International Conference on Wind energy Grid-Adaptive Technologies (WEGAT), Chungbuk University, Korea, 2014.

C4. **H. Liu**, K. Ma, P. C. Loh, F. Blaabjerg, "Lifetime Estimation of MMC for Offshore Wind Power HVDC Application," Proc of the International Power Electronics and Application Conference and Exposition (PEAC), pp. 35-40, 2014.

C5. **H. Liu**, K. Ma, P. C. Loh, F. Blaabjerg, "Design of State Observer for Modular Multilevel Converter," Proc of 6th International Symposium on Power Electronics for Distributed Generation Systems (PEDG), pp. 1-6, 2015.

C6. **H. Liu**, K. Ma, P. C. Loh, F. Blaabjerg, "A Sensorless Control Method for Capacitor Voltage Balance and Circulating Current Suppression of Modular Multilevel Converter," Proc of IEEE Energy Conversion Congress & Expo (ECCE), pp. 6376-6384, 2015.

Since these papers have provided technical explanations and validation results for the thesis, the relationship between the publications listed above and the chapters of this thesis is summarized in Table 1.2.

TABLE 1.2 RELATIONSHIP BETWEEN PUBLICATIONS AND CHAPTERS OF THE THESIS

Chapter No.	***Chapter Title***	***Relevant Publication No.***
1	Introduction	J1, J6, C1, C2
2	MMC Lifetime Estimation	J3, C4
3	MMC Thermal under Grid Faults	J5
4	MMC State Observer	J4, C5
5	MMC Fault Diagnosis	J2, J4, C6
6	Conclusion	-

2 Lifetime Estimation of the devices in MMC Under Different Wind Speeds

The lifetime of MMC is decided by the lifetime of the used semiconductors. There are various factors affecting the lifetime of the semiconductors. Besides the characteristics of the semiconductor devices in the converter, the working environment along with the mission profile of the converters is also quite important to the lifetime. Therefore, this chapter focuses on the lifetime of semiconductors used in MMC under certain mission profile.

The working region and the mission profile are first analyzed in this chapter. Then the topology of MMC is introduced based on which the dynamic power losses are calculated. Then the thermal profile is studied with the variation of the power losses and the datasheet based electro-thermal model. Finally, based on the thermal loadings, the lifetime estimation is carried using rain flow analysis algorithm to find out which devices are suffering the most stress in the worst case scenarios.

To illustrate the lifetime estimation procedure of the MMC, the offshore wind power generation HVDC transmission system as shown in Fig. 1.3 is basically designed as a study case, and 9 wind turbines with 2 MW rated power is composed of an offshore wind farm. A 1-year offshore wind speed curve sampled at per hour from Zhoushan, Zhejiang Province, China is displayed in Fig. 2.1, which is considered as the wind speed applied to the wind turbines in this chapter. Both the wind farm-side converter and the grid-side converter employ three-phase MMC, it is detailed shown in Fig. 1.4. Each phase of the MMC contains 24 identical half-bridge modules with the Infineon IGBT module *FZ1200R45KL3_B5* ($T_J = 125\,℃$) chosen as power semiconductor devices. The system specifications are basically designed according to Table 2.1.

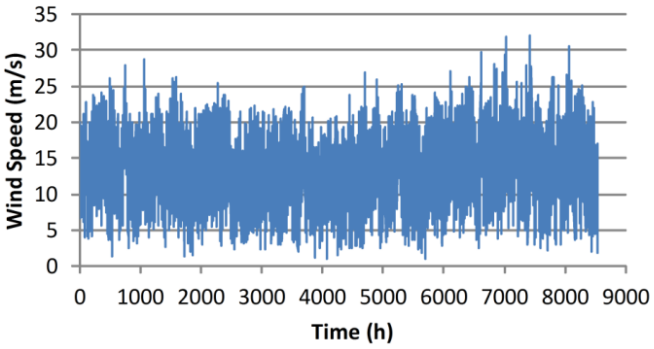

Fig. 2.1. Annual wind speed measured at Zhoushan (the wind speed is sampled per hour).

TABLE 2.1 SPECIFICATIONS OF THE STUDIED MMC SYSTEM

Parameter	***Value***
System rated active power P	18 MW
Rated DC-link voltage Vdc	31.8 kV
Rated AC grid voltage Vac	14 kV
Number of Wind Turbine (WT) n	9
WT rated active power p	2 MW
Cut in wind speed	3 m/s
Cut out wind speed	23 m/s
Rate wind speed	11 m/s
Converter type	MMC
Number of sub-module per arm N	12
Sub-module type	Half-bridge
Arm inductor L	4 mH (0.15 $p.u.$)
Arm resistor R	0.0628 Ω
Sub-module Capacitor C	0.8 mF
Switching frequency f_s	1 kHz
Fundamental frequency f	50 Hz
Modulation index M	0.9
Power factor	1

With Maximum Power Point Tracking (MPPT) control, the absorbed wind power by each wind turbine is calculated in Fig. 2.2, assuming that the mechanical dynamics of the wind turbine can achieve steady state characteristic at each of the sample shown in Fig. 2.1 which is very feasible with this sample rate. Then the transmission power of the MMC-HVDC during one year is nine times of the power in Fig. 2.2.

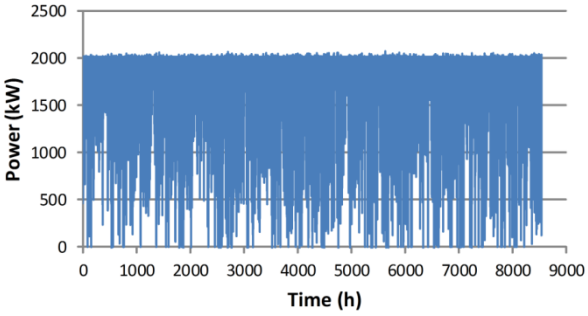

Fig. 2.2. Annual produced power from one 2 MW wind turbine using the mission profile in Fig. 2.2.

As the wind farm-side converter can share a similar analysis approach with the grid-side converter, for simplicity only the grid-side converter is analyzed in this Chapter. A Carrier Phase Shift Pulse Width Modulation (PSPWM) scheme [76] is applied as the modulation of the MMC. As shown in Fig. 2.3 (take four modules in each arm as an example), PSPWM is a carrier-based modulation method and the gating signals $S_{p(n)i}$ for sub-modules are generated by comparing the reference signals $v_{ref_jp(n)}$with those carriers $C_{p(n)i}$. When the PSPWM is employed to the MMC

with N sub-modules per arm, N triangular carriers are required in each arm. All carrier signals in PSPWM have the same amplitude, frequency and DC offset.

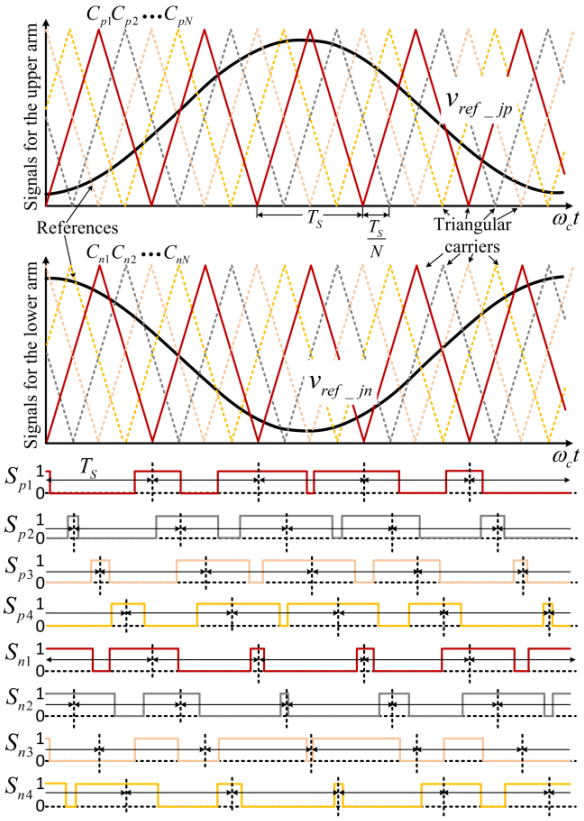

Fig. 2.3. Principle of PSPWM.

2.1 Power loss distribution of the devices in MMC

2.1.1 Operation principle of MMC

Compared to the two-level or three-level voltage source converters, the power loss calculation of the MMC is relatively more complicated. Therefore, the MMC working principle along with its power loss calculations are briefly introduced in this section.

The working principle of the i_th sub-module (SM) in the MMC can be divided into four stages depending on the gating signal of the sub-module $g_{p(n),i,k}$ (g_{S1}, g_{S2}, g_{D1}, g_{D2} denoting the on-off state of S_1, S_2, D_1 and D_2, respectively) and the current

direction $i_{p(n),k}$ $(k = a, b, c, p = upper\ arm, n = lower\ arm)$. As shown in Fig. 2.4, the following can be obtained for the operation:

1) From $t_1$to t_2, the arm current $i_{p(n),k}$ is positive, if S_1 is turned on, S_2 is turned off, the current flows through D_1 and capacitor, the capacitor is charged as illustrated in Fig. 2.5 (a) and $\mathrm{P_{SM}} = \mathrm{P_{D_1}}$; otherwise, S_1 is turned off, S_2 is turned on, the current goes through S_2 (Fig. 2.5 (b)) and $\mathrm{P_{SM}} = \mathrm{P_{S_2}}$;
2) In the next stage from $t_2$to t_3, the arm current $i_{p(n),k}$ is negative, when S_1 is turned off, S_2 is turned on, the current flows through D_2 (Fig. 2.5 (c)), $\mathrm{P_{SM}} = \mathrm{P_{D_2}}$; oppositely, when S_1 is on, S_2 is off, the current goes through S_1 and capacitor, the capacitor is discharged as shown in Fig. 2.5 (d), $\mathrm{P_{SM}} = \mathrm{P_{S_1}}$.

where $\mathrm{P_{SM}}$ is the power loss of the sub-module, $\mathrm{P_{D_1}}$, $\mathrm{P_{S_2}}$, $\mathrm{P_{D_2}}$, $\mathrm{P_{S_1}}$ are the losses in D_1, S_2, D_2, S_1 respectively. This can be represented as shown in Table 2.2 and the loss is calculated as presented in the next section.

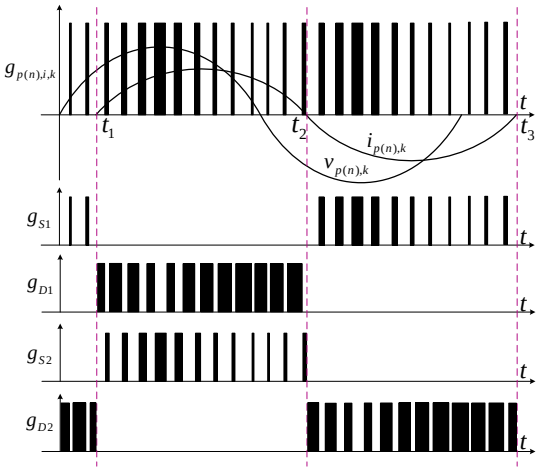

Fig. 2.4. On-off state pattern for devices in the same sub-modules shown in Fig. 1.3 in the MMC.

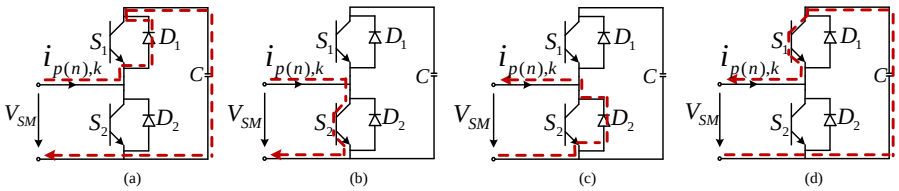

Fig. 2.5. Four working stages of the sub-module in the MMC: (a) positive arm current and S_1 on; (b) positive arm current and S_2 on; (c) negative arm current and S_2 on; (d) negative arm current and S_1 on.

TABLE 2.2 FOUR WORKING REGIONS OF THE SUB-MODULE IN MMC

State no.	*Time*	*Current*	*Status*	*Gating Signal*	*Power Loss*
1*st*	$t_1 \rightarrow t_2$	$i_{p(n),k} > 0$	S_1on, S_2off	$g_{p(n),i,k} = 0$	$P_{SM} = P_{D_1}$
2*nd*		$i_{p(n),k} > 0$	S_1off, S_2on	$g_{p(n),i,k} = 1$	$P_{SM} = P_{S_2}$
3*rd*	$t_2 \rightarrow t_3$	$i_{p(n),k} < 0$	S_1on, S_2off	$g_{p(n),i,k} = 0$	$P_{SM} = P_{S_1}$
4*th*		$i_{p(n),k} < 0$	S_1off, S_2on	$g_{p(n),i,k} = 1$	$P_{SM} = P_{D_2}$

2.1.2 Loss distribution of MMC

Once the operation profiles of the grid converter have been clarified, it is possible to analyze the loss distribution in the power semiconductor devices of the MMC. A power loss model, based on the average switching losses and conduction losses as described in [77], is used in this thesis. In the power loss model, a series of information provided in the devices datasheet by the manufacturer is used.

For the calculation of the switching losses, the curve of $E_{sw}\left(i_k(t), T_{ref}\right)$, which is the switching loss of the power devices (E_{on} and E_{off} for S_1 and S_2 and E_{rec} for D_1 and D_2) under the different load current $i_k(t)$ and the tested junction temperature T_{ref}, is extracted to calculate the switching loss of the devices under other junction temperatures $E_{sw}\left(i_k(t), T_j\right)$ by

$$E_{sw}\left(i_k(t), T_j\right) = E_{sw}\left(i_k(t), T_{ref}\right) \cdot [1 + K_{T\_sw} \cdot (T_j - T_{ref})] \tag{2.1}$$

K_{T_sw} is the temperature coefficient.

Once the switching losses have been clarified as expressed in equation (2.1), the dynamic switching loss can be obtained as given below

$$P_{sw}(t) = f_s \cdot E_{sw}(i_k(t), T_j) \cdot (V_{dc}/2V_{ref})^{K_v} \tag{2.2}$$

Where f_s is the switching frequency, K_v is the voltage coefficient, V_{ref} is the tested voltage on the datasheet.

The averaged switching loss of the devices S_1, S_2, D_1 and D_2 can be calculated by

$$P_{sw\_ave} = f_o \cdot \int_0^{1/f_o} P_{sw}(t)dt \tag{2.3}$$

where f_o is the fundamental frequency.

Similarly, to calculate the conduction loss of the devices, the characteristic of the conduction voltage $v_{con}\left(i_k(t), T_{ref}\right)$ under the tested reference junction temperature

in the datasheet is fitted and the conduction voltages under different junction temperatures are calculated as

$$v_{con}\left(i_k(t), T_j\right) = \left[V_{con} + K_{T\_con_1} \cdot \left(T_j - T_{ref}\right)\right] + i_k(t) \cdot [r_{con} + K_{T\_con_2} \cdot \left(T_j - T_{ref}\right)] \tag{2.4}$$

V_{con}, $K_{T\_con_1}$, r_{con}, $K_{T\_con_2}$ are coefficients.

Then the instantaneous conduction loss can be represented by

$$P_{con}(t) = v_{con}(i_k(t), T_j) \cdot i_k(t) \cdot D(m, t) \tag{2.5}$$

where $D(m, t)$ is a function of the modulation index m, which is related to the modulation method applied.

The average conduction loss in one fundamental period is

$$P_{con\_ave} = f_o \cdot \int_0^{1/f_o} P_{con}(t)dt \tag{2.6}$$

It should be noted that the coefficients K_{T_sw}, K_v, V_{con}, $K_{T\_con_1}$, r_{con}, $K_{T\_con_2}$ are obtained by fitting the parameters to the corresponding curves in the datasheet.

2.1.3 Simulation results

From the above analysis it can be concluded that the power loss is affected by the loading current, conduction voltage, switching frequency, fundamental frequency, conduction time as well as modulation strategy. As can be seen from Fig. 2.3, with the PSPWM, the switching frequency, fundamental frequency and the conduction time are the same for all the modules in each fundamental period. Moreover, the arm currents $i_{p(n),k}$ for the six arms in the MMC and the capacitor voltages $v_{c,p(n),i,k}$ in the six arms are shown in Fig. 2.6 and Fig. 2.7, respectively. It can be seen that the currents flowing through those modules and the voltages of those module are the same in each fundamental period which can lead to the same power loss in a fundamental period among those modules. However, from Fig. 2.4 and Fig. 2.5, it can be seen that the conduction time and the loading current for the devices in the same module is unequal which means the power loss of the devices in the same module may be not the same. Therefore, to analyze power loss of those devices, Fig. 2.8 is given.

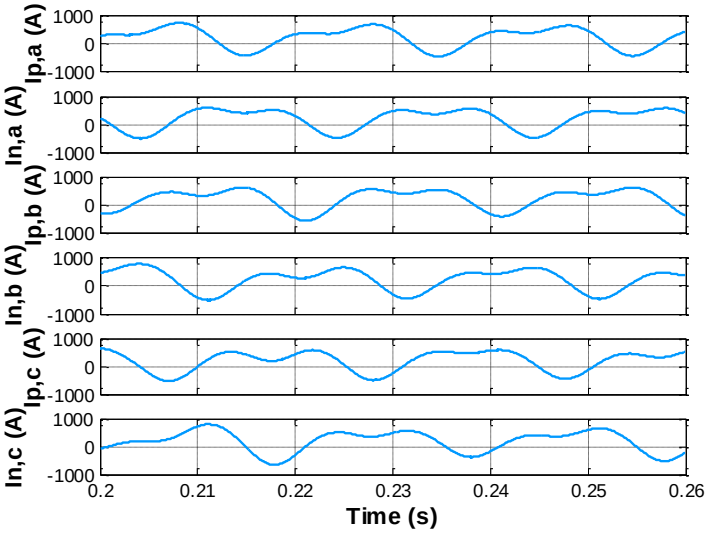

Fig. 2.6. Arm currents of MMC using the test conditions in Table 2.1 at rated wind speed.

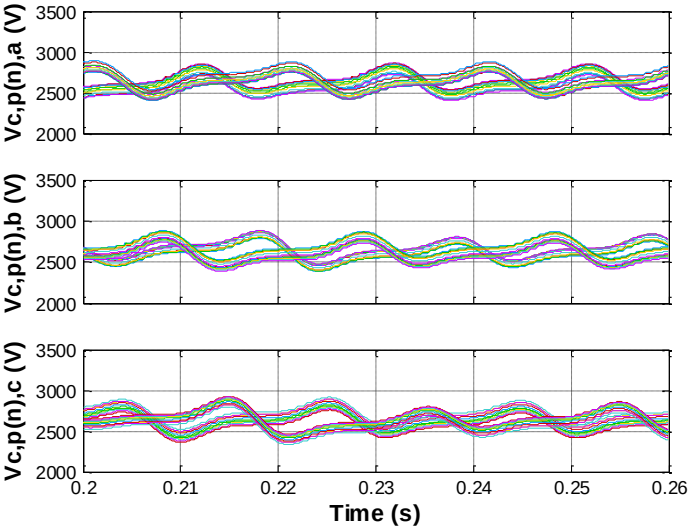

Fig. 2.7. Capacitor voltages in modules of MMC using the test conditions in Table 2.1 at rated wind speed.

In Fig. 2.8, the upper arm current in phase a ($I_{p,a}$), the gating signal ($g_{p,1,a}$), the capacitor voltage and current ($V_{c,p,1,a}$ and $I_{c,p,1,a}$), the currents flowing through the four semiconductors in the first module in upper arm ($I_{S1,p,1,a}$, $I_{S2,p,1,a}$, $I_{D1,p,1,a}$ and $I_{D2,p,1,a}$) in phase a are shown. As can be seen, when the arm current i_{ap} is positive, the current go through D_1, S_2 and when the arm current $I_{p,a}$ is negative, the current

flow through D_2, S_1 depending on the status of the gating signal $g_{p,1,a}$. The results agree with the definition in Table 2.2 and the currents flowing through the four semiconductors also illustrate the different conduction time and loading current.

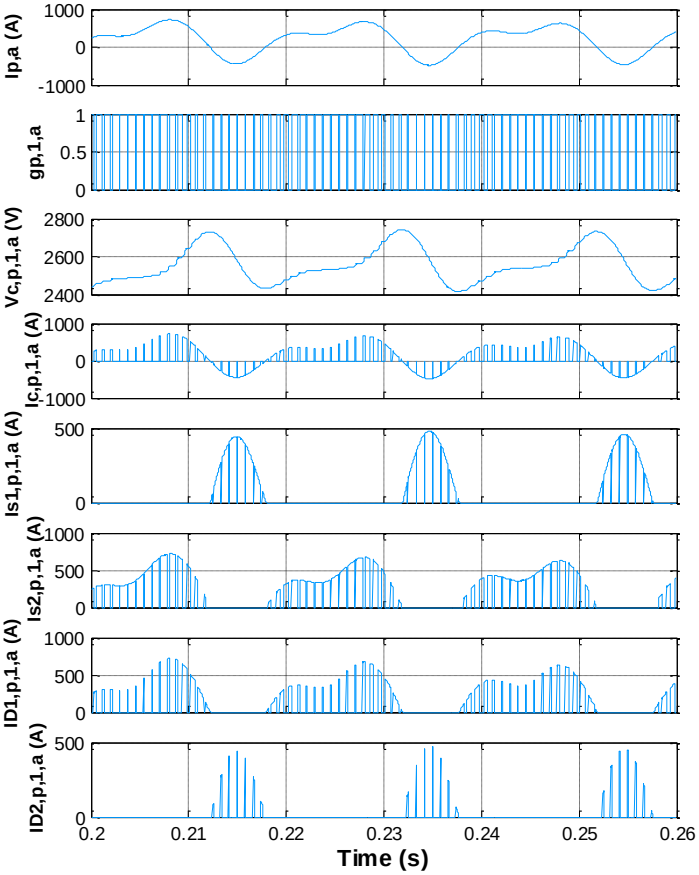

Fig. 2.8. Simulation results of working principle of MMC using the test conditions in Table 2.1 at rated wind speed.

By using the equations (2.1)-(2.8), the power loss of the four semiconductors in the same module is calculated and shown in Fig. 2.9. Under rated wind speed, S_2 and D_1 produce more power loss than S_1 and D_2. Moreover, the power loss under different wind speeds are also obtained and shown in Fig. 2.9. It can be seen that all the losses in each of the power device are changing with the variation of the wind speed. Larger wind speed generates larger power loss as expected when the current wind speed is lower than the rated wind speed and larger than the cut in wind speed. When the wind speed is higher than the rated wind speed and lower than the cut out wind speed, the power loss for each device is maintained constant because the wind power generator

works at the rated speed even when the wind speed is higher than the rated wind speed.

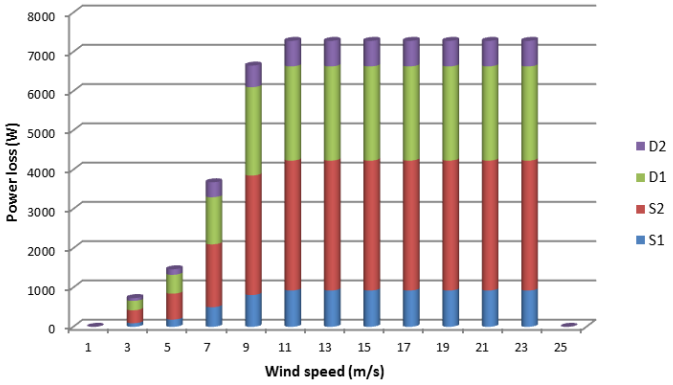

Fig. 2.9. Power loss of semiconductors in a sub-module using the test conditions in Table 2.1 under various wind speed.

2.2 Thermal analysis of the devices in MMC

2.2.1 Principle of thermal distribution

The thermal distribution of the MMC can be obtained based on the power loss calculated above and the dynamic electro-thermal model denoted by the thermal equivalent circuit diagrams shown in Fig. 2.10.

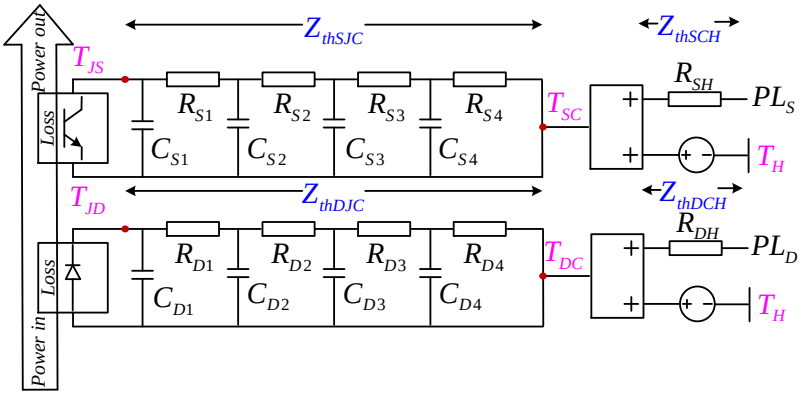

Fig. 2.10. Electro-thermal network model of the power semiconductor devices.

In Fig. 2.10, T_{JS} and T_{JD} are the junction temperatures of IGBT and Diode, respectively; T_{SC} and T_{DC} are the case temperature of IGBT and Diode; T_H heatsink

temperature; The Z_{thSJC} and Z_{thDJC} are the IGBT impedance and Diode impedance from junction to case, composed of the equivalent thermal resistance $R_{S(D)i}$ and thermal capacitance $C_{S(D)i}$ networks, which are generally described by Cauer [52]; The equivalent impedance can be obtained from the datasheet. Thermal resistances can be directly read, whereas the thermal capacitances can be calculated from $\tau_{S(D)i} = R_{S(D)i}C_{S(D)i}$ which are also given in the datasheet of the device. Z_{thSCH} and Z_{thDCH} are the impedances of IGBT and Diode from case to heatsink. PL_S And PL_D are the power loss of IGBT and Diode. The junction temperature calculation can be expressed as

$$T_{JS} = Z_{thSJC} \cdot PL_S + T_C \tag{2.7}$$

$$T_{JD} = Z_{thDJC} \cdot PL_D + T_C \tag{2.8}$$

$$T_{SC} = Z_{thSCH} \cdot PL_S + T_H \tag{2.9}$$

$$T_{DC} = Z_{thDCH} \cdot PL_D + T_H \tag{2.10}$$

Because the temperature of the heat sink T_H is normally much lower and more stable compared with the junction temperature T_{JS} and T_{JD} in a properly designed converter system, the heat sink temperature is considered as a constant value at 40 ºC in this paper. However, the heat sink temperature may strongly depend on the operation site and the design of the heat sink system. Here a fourth-order Cauer model is employed as described in Table 2.3 and using $R_{SH} = 0.009\ K/W$, $R_{DH} = 0.014\ K/W$.

TABLE 2.3 SPECIFICATION OF THE FOURTH-ORDER CAUER MODEL

Device	***Parameter***	***Value***			
	i	1	2	3	4
IGBT	$R_{Si}\ (K/W)$	0.002075	0.0129	0.007028	0.002002
	$C_{Si}\ (J/K)$	0.614	1.1	4.186	293.4
Diode	$R_{Di}\ (K/W)$	0.00576	0.02564	0.01379	0.002803
	$C_{Di}\ (J/K)$	0.1908	0.5418	2.51	210.5

2.2.2 Simulation results

The junction temperature of the power devices in the sub-module can be obtained under the rated wind speed as shown in Fig. 2.11, where three fundamental cycles are indicated. As expected, S_2 and D_1 have higher temperature compared to S_1 and D_2 due to they consume more power than S_1 and D_2 under the same cooling conditions. In each fundamental period, the temperature of the power devices experience rising and falling period. S_2 and D_1 share the same rising period which is the falling period of S_1 and D_2. The appearance of a sawtooth wave during the rising period of the temperature is generated by alternatively triggering of S_2 and D_1 or S_1 and D_2, respectively.

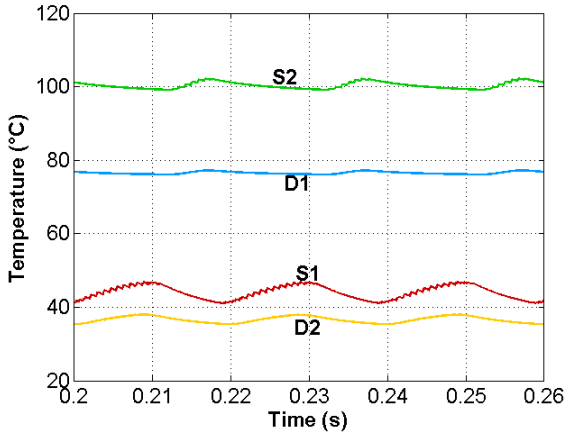

Fig. 2.11. Junction temperature of the power semiconductors in a sub-module in MMC within three cycles using the test condition in Table 2.1.

The temperature of the devices in the same sub-module under various wind speed are shown in Fig. 2.12, where the temperatures of the devices are following the fluctuation of the power losses. When the current wind speed is lower than the rated wind speed and higher than the cut-in wind speed, the temperature of all the devices will fluctuate following the change of wind speed. When the current wind speed is higher than the rated wind speed, the temperature will be constant because the wind power generator works at the rated speed under this situation.

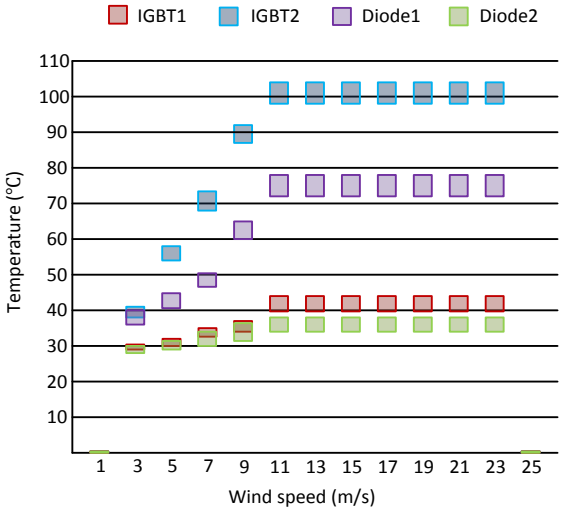

Fig. 2.12. Thermal profile of semiconductors in a sub-module in MMC using the test condition in Table 2.1 under various wind speed.

Based on the above analysis and the 1 year mission profile shown in Fig. 2.1, TS_1, TS_2, TD_1 and TD_2, the one year junction temperatures of the devices S_1, S_2, D_1 and D_2 in the sub-module, are shown in Fig. 2.13, which are closely related to the major failure mechanisms as well as the lifetime of the MMC.

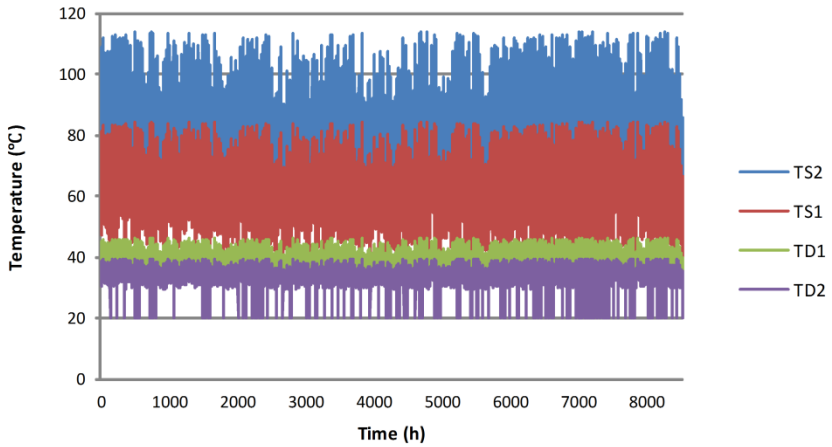

Fig. 2.13. Thermal profile of devices during one year using the test condition in Table 2.1 and the mission profile in Fig. 2.2.

2.3 Lifetime estimation of the devices in MMC

After the thermal profiles of the device under a wind speed variations has been established, it is possible to calculate the lifetime of device consumed by this complicated thermal cycles. Therefore, in this section the lifetime of the devices will be calculated based on the thermal profiles.

However, the thermal profile in Fig. 2.13 is too disordered to be used to calculate the lifetime. Thus a rain flow counting method developed by Endo and Matsuishi [78] is employed to convert the random thermal loading into the organized thermal cycles which are more suitable to be utilized by the lifetime models, as shown in Fig. 2.14. In Fig. 2.14, the x-axis is the maximum junction temperature, the y-axis means the fluctuation of the counted cycles, while the z-axis is the counted cycles. Each column denotes the cycles counted under the same maximum temperature and the same temperature fluctuation. There are total 1843 cycles counted in the thermal profiles and it can be seen that most cycles are located at the two ends where the lowest temperature and highest temperature are distributed. That is due to the possibility for the wind speed lower than the cut-in wind speed or higher than the rated wind speed is relatively higher than other situations. The lifetime of the MMC is related to the

magnitude and frequency of these temperature cycles. Each cycle applies different stress to the power module and it further leads to certain lifetime consumed. The consumed lifetime by the thermal cycles can be calculated by employing mathematical models.

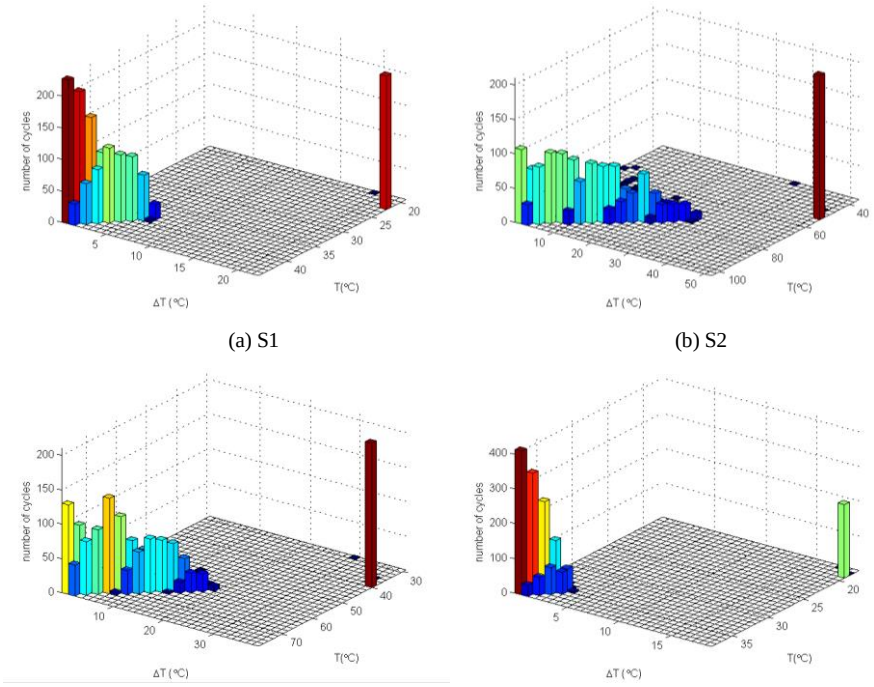

(a) S1 (b) S2

(c) D1 (d) D2

Fig. 2.14. Rainflow counting results of one year operation of the wind turbine (a) S_1; (b) S_2; (c) D_1; (d) D_2.

Among the analytical modelling methods of lifetime, the Coffin-Manson model [79] is the most widely used approach. However, it is relatively simple and inaccurate as it does not take frequency of cycles and heating and cooling times into account. The Norris-Landzberg model [80] takes also cycle frequency into account and the Bayerer's model [81] considers more factors which leads to much more complications in the calculation. Therefore, the Norris-Landzberg lifetime estimation model as shown in (2.11) has been used here to evaluate the percentage of the consumed lifetime of the semiconductors in the sub-module by each counted thermal cycle taken in the total lifetime.

$$N_f = A \cdot cf^{-\alpha} \cdot \Delta T_J^{-\beta} \cdot e^{(E_a/(K_B \cdot T_{Jmax}))} \tag{2.11}$$

where ΔT_j is the difference between maximum and minimum junction temperatures, T_{Jmax} is the maximum junction temperatures in Kelvin, cf is the cycle frequency, $K_B = 1.38 \times 10^{-23}$ is the Boltzmann constant, and $E_a = 0.42$ is the activation energy, $A = 310$ and $\alpha = 0.4$, $\beta = 2.0$ are the curve fitting parameters [80].

Then the total consumed lifetime CL_{1year} by the counted 1843 thermal cycles in one year can be accumulated in (2.12) according to the Miner's rule [82] and the lifetime of the devices LF can simply be calculated in (2.13).

$$CL_{1year} = \sum_{n=1}^{number\ of\ counted\ cycles} N_f \tag{2.12}$$

$$LF = \frac{1}{CL_{1year}} \tag{2.13}$$

The counted results as well as the total consumed lifetime by the counted cycles as well as the estimated lifetime are given in Table 2.4. Although S_1, S_2, D_1 and D_2 share the same counted cycle number, they consumed very different lifetime which means the lifetimes of devices under the mission profile are different. It can be seen that the S_2 which has the highest temperature, consumes the most lifetime, 2.53% of its whole lifetime, demonstrating that S_2 has the shortest lifetime, while D_2 with the lowest temperature and consumes the least lifetime 0.16% (D_2 has the longest lifetime). Although the counted temperature cycles for the four devices is same under the given mission profile, they have different lifetime which illustrates that not only the number of counted temperature cycles affects the consumed lifetime of the power semiconductors, but also suffering the maximum temperature and the fluctuation of temperature of each cycle is of significant importance for the lifetime consumption.

TABLE 2.4 LIFETIME CONSUMPTION OF DEVICES IN ONE SUB-MODULE OF MMC FOR ONE YEAR OF OPERATION

Device	*Counted Cycles*	*Consumed Lifetime (%)*	*Lifetime (year)*
IGBT1	1843	0.21%	476
IGBT2	1843	2.53%	39
Diode1	1843	1.96%	51
Diode2	1843	0.16%	625

It should be noted that the estimated lifetime of the devices are large. That's because the wind speed is sampled per hour and the wind speed is assumed to be constant during the hour, thus, the temperature of the devices are kept stable and the consumed lifetime is less. Actually, the wind speed changes from second to second and the

temperature of the devices also change very fast (depending on the thermal capacitance) and the consumed lifetime will be much more than in the above case.

However, although the calculated lifetime is not so accuracy for each device, the comparison among the lifetimes of the four devices is illustrated in this case. To make longer lifetime and higher reliability of MMC, some actions can be taken based on the analysis results, such as using high quality IGBT and Diode for S_2 and D_1, improving the cooling system to make S_2 and D_1 cool faster or designing suitable control strategy.

2.4 Summary

Lifetime estimation of MMC is important for its performance and reliability during operation. Hence, this chapter presents the lifetime prediction of the MMC based on the fatigue load according to the operational principle of the MMC and the different working conditions. It is concluded that different devices bear different stress and have different lifetime, and it is also illustrated that not only the number of counted temperature cycles affects the consumed lifetime of power semiconductors, but also the maximum temperature and the fluctuation of temperature of each cycle is of significant importance for the lifetime consumption. According to the conclusion, the proper cooling system and control strategy can be considered to improve the reliability of MMC.

3 Power Loss and Thermal Distribution of MMC Under Grid Faults

Due to the high cost for maintenance at distant offshore wind farm and strict requirements to the stability of the grid, the ability to withstand grid disturbances is greatly important for the MMC-HVDC system. Consequently, this chapter focuses on the analysis of the loading states of the semiconductors in the MMC under various grid faults, as the semiconductor is the most vulnerable. First, the impact of various grid faults to the ac bus voltages and the converter operations are simulated and also analytically solved. Afterwards, the corresponding loss and thermal behavior of the power semiconductor devices in the MMC is presented.

3.1 LVRT operation of the MMC under various grid faults

The Low-Voltage Ride-Through (LVRT) codes for the Wind Turbine Systems (WTSs) have been issued in several countries and it is shown in Fig. 3.1 [83], in which the dipping depth of grid voltage against the disturbing time is defined and is different for different countries. Furthermore, it is required by some codes that the WTS can provide some reactive power (up to 100% current capacity) to help the grid voltage recovery during its dips. Fig. 3.2 shows two examples from the German and China grid codes in which the required reactive currents vs the amplitudes of the grid voltage are specified [84].

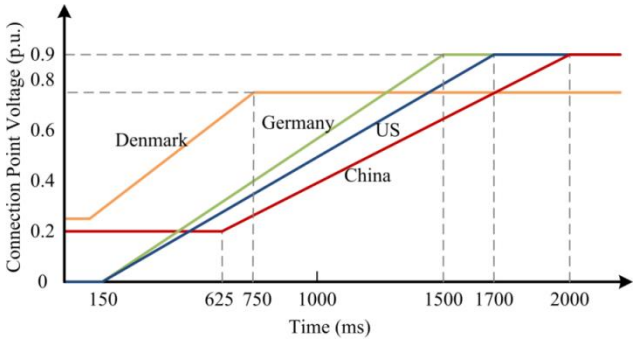

Fig. 3.1. Grid codes of wind turbines under LVRT by different countries [83].

There are several types of grid faults in such system and two typical grid faults are defined and explained in [77]. In this chapter single-phase ground fault and three-phase ground fault, are in focus [85, 86]. However, no matter which type it is, when a short-circuit fault happens in the power grid, normally the voltage dips will be detected by the grid-connected converter through the ac bus it is connected to, and

then the corresponding LVRT control algorithm, as explained in [87- 89] is activated, making the converter shifting from normal operation mode to the LVRT mode.

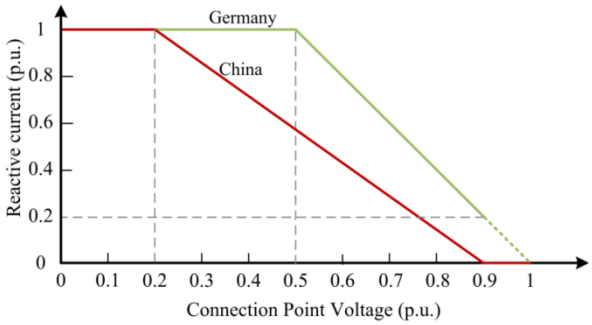

Fig. 3.2. Reactive current requirements versus grid voltage V_g during LVRT [84].

The control scheme, as shown in Fig. 3.3, is adopted to deal with different grid faults; both the output voltages and currents are detected and decomposed into positive and negative sequence voltages/currents by using low pass filters and band-pass filters respectively.

It should be noted that there is no zero sequence current flowing through the MMC since no zero sequence current loop is formed. Therefore, there is no zero sequence current controller in Fig. 3.3. Moreover, when any of the two faults occurs in the AC grid, the grid-side MMC transmits less power while there is no change in the wind power, which leads to imbalance of power in HVDC system and rise of DC voltage. However, a DC voltage ripple suppression controller [89] is assumed to be used here to maintain the DC voltage at a normal value.

The reference for the positive sequence I_{q+} current is set according to the German grid code reported in Fig. 3.2 and the I_{d+} current is referred to the generated active power by the wind turbines [77], while the references for the negative sequence I_{q-} and I_{d-} currents are set to zero. Then I_{d+} and I_{q+} reference can be solved analytically as:

$$I_{d+} = \begin{cases} 0\ p.u., & 0 < \dfrac{v_f}{v_n} \leq 0.5\ p.u. \\ \dfrac{2P}{3V_{d+}}, & 0.5\ p.u. < \dfrac{v_f}{v_n} \leq 1 \end{cases} \tag{3.1}$$

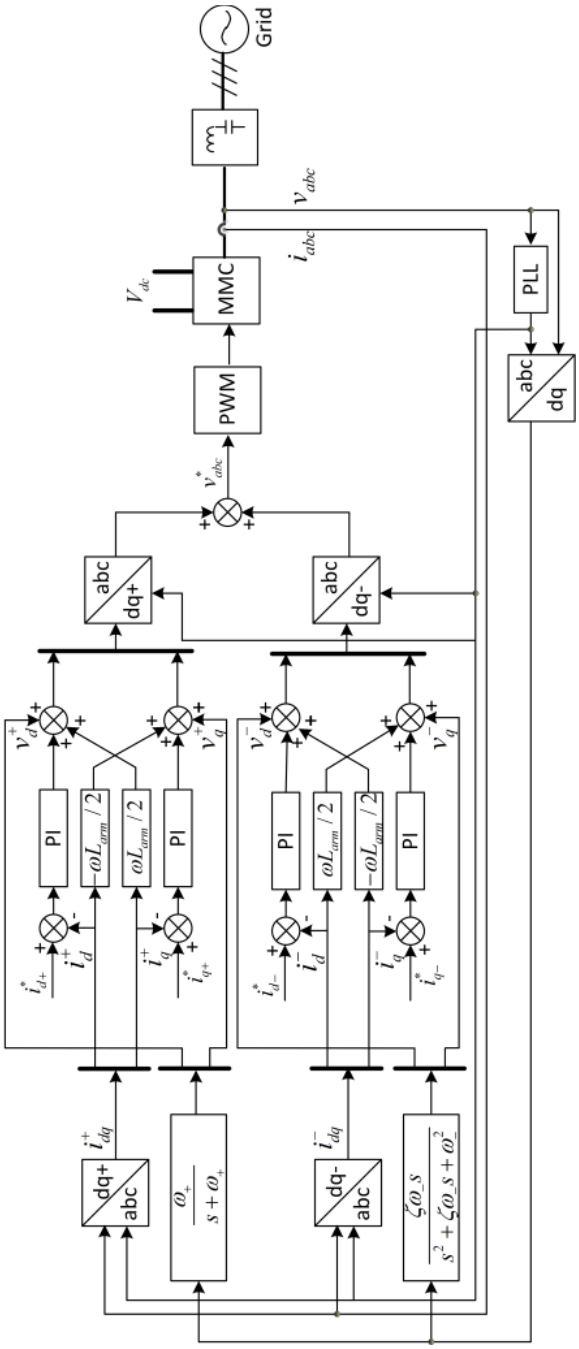

Fig. 3.3. Structure of current control scheme of the grid-side MMC.

$$I_{q+} = \begin{cases} 1\ p.u., & 0 < \dfrac{v_f}{v_n} \le 0.5\ p.u. \\ 2\left(1 - \dfrac{v_f}{v_n}\right), & 0.5\ p.u. < \dfrac{v_f}{v_n} \le 1 \end{cases} \tag{3.2}$$

where v_f is the grid voltage of the faulty phase under fault condition and v_n is the grid voltage under normal condition, P is the generated active power by the wind turbines, which is related to the available wind energy. The functions can be found in [90].

3.2 Simulation results

Fig. 3.4 gives the operation profile for the MMC under two types of grid faults with the same grid voltage dip severity, which is denoted as $Dip = 0.5\ p.u.$. The output voltages, load currents, and the instantaneous active/reactive power values are shown, respectively. As it is shown in Fig. 3.4, the output voltages under each given grid fault condition are consistent with the fault definition, and the currents are symmetrical among the three phases, which means that only the positive sequence currents are injected. Due to the existence of negative sequence voltage, there is a second order oscillation of the fundamental frequency in the delivered active and reactive power under the unbalanced grid faults.

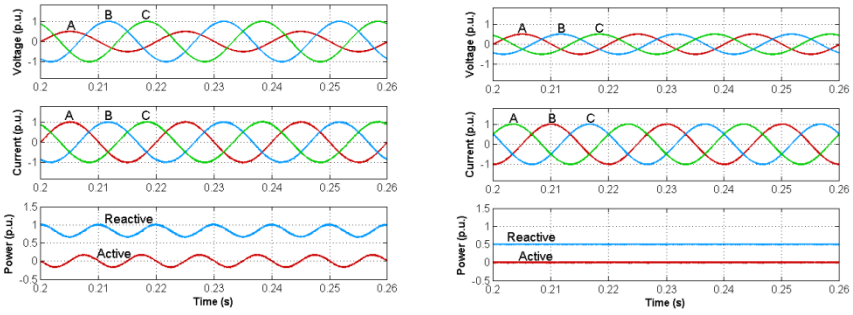

(a) (b)

Fig. 3.4. Outputs of the grid-side MMC under various grid faults ($Dip = 0.5\ p.u.$, $v_w = 11\ m/s$, German grid codes). (a) Single-phase ground fault. (b) Three-phase ground fault.

The averaged active power and reactive power delivered by the MMC versus voltage dips under the two grid faults are shown in Fig. 3.5 (a) and Fig. 3.5 (b), respectively. It can be seen that the reactive power is significantly different, especially when $Dip < 0.5\ p.u.$ because of the compensation requirement of reactive power according to the grid codes.

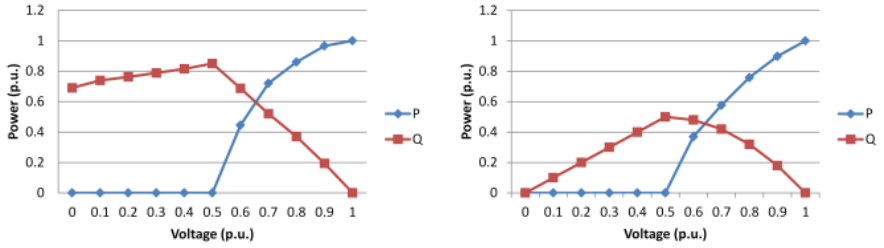

(a) (b)

Fig. 3.5. Active and reactive power values versus dip severity on the PCC. (a) Single-phase ground fault. (b) Three-phase ground fault.

The loss distributions of the four power switching devices in one MMC module at different grid voltage dips under the two fault conditions are shown in Fig. 3.6 (a)-(b), respectively, in which the AT1, BT1, CT1 mean IGBT S_1 in phase a, b, c, AD1, BD1, CD1 are diode D_1 in phase a, b, c, AT2, BT2, CT2 are S_2 in phase a, b, c and AD2, BD2, CD2 are D_2 in phase a, b, c. All of them are obtained under the rated wind speed $v_w = 11\ m/s$. It can be seen that the loss distribution among the three phases of the converter are asymmetrical under the single-phase unbalanced grid faults.

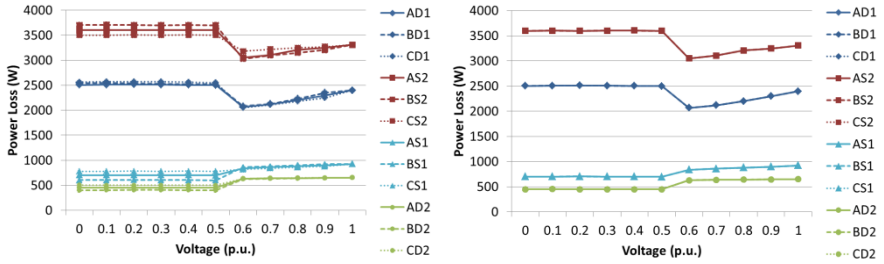

(a) (b)

Fig. 3.6. Power loss versus grid voltage dip severity ($v_w = 11\ m/s$). (a) Single-phase ground fault. (b) Three-phase ground fault.

Fig. 3.7 (a)-(c) displays the thermal distribution under normal condition in Phase a, b and c, in which it can be seen that the operation is balanced among the three phases under normal condition.

The junction temperatures for the devices in the same module in the three phases of the MMC undergoing single-phase grid fault (voltage dip in phase a) are shown in Fig. 3.8 (a)-(c), respectively. It is shown that the thermal loading behaviors in the three phases of the converter are different from each other under this fault condition. The temperature of S_2 and D_1 in Phase a is lower than that in phase b and higher

than that in phase c, while the temperature of S_1 and D_2 in Phase a is higher than that in phase B and lower than that in Phase c.

The junction temperatures for the three phases of the MMC suffering the three-phase ground grid fault are shown in Fig. 3.9 (a)-(c). It is shown that the thermal loading behaviors in the three phases of MMC are exactly the same under this grid fault.

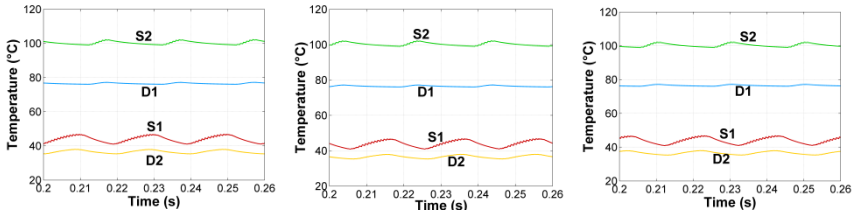

(a) (b) (c)

Fig. 3.7. Thermal distribution of the grid-side MMC under normal condition ($v_w = 11\ m/s$). (a) Phase a. (b) Phase b. (c) Phase c.

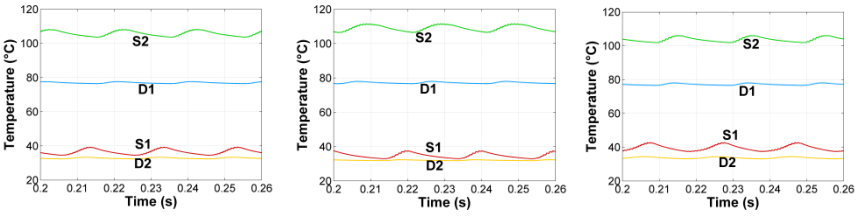

(a) (b) (c)

Fig. 3.8. Thermal distribution of the grid-side MMC under single-phase ground fault ($Dip = 0.5\ p.u.$, $v_w = 11\ m/s$). (a) Phase a. (b) Phase b. (c) Phase c.

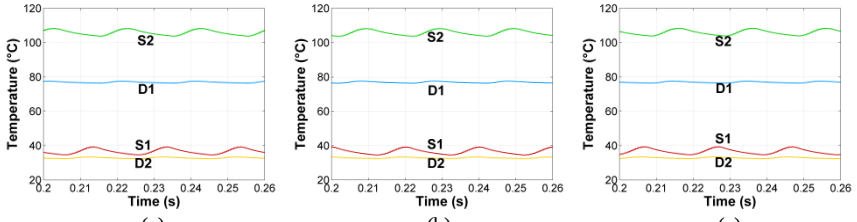

(a) (b) (c)

Fig. 3.9. Thermal distribution of the grid-side MMC under three-phase ground fault ($Dip = 0.5\ p.u.$, $v_w = 11\ m/s$). (a) Phase a. (b) Phase b. (c) Phase c.

The dynamic responses of the device temperatures with a voltage dip time of 500 ms under single-phase ground fault and three-phase ground fault are presented in Fig. 3. 10 and Fig. 3.11, respectively, the grid voltage dips to $0.5\ p.u.$ at $1\ s$ and recoveries to normal at $1.5\ s$. Under both of the two fault conditions, the

temperature of S_1 and D_2 are lower than that under the normal condition, while the temperature of S_2 and D_1 are higher than that under the normal condition.

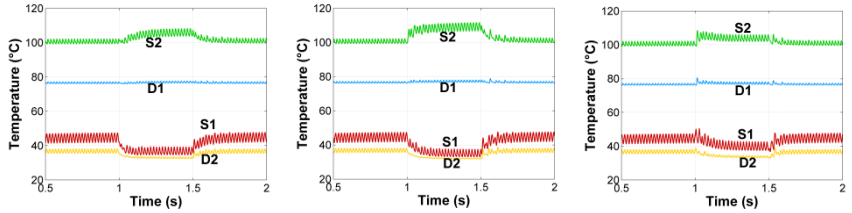

(a) (b) (c)

Fig. 3.10 Junction temperature dynamic response with a voltage dip time of 500 ms under single-phase ground fault ($Dip = 0.5\ p.u.$, $v_w = 11\ m/s$) (a) Phase a. (b) Phase b. (c) Phase c.

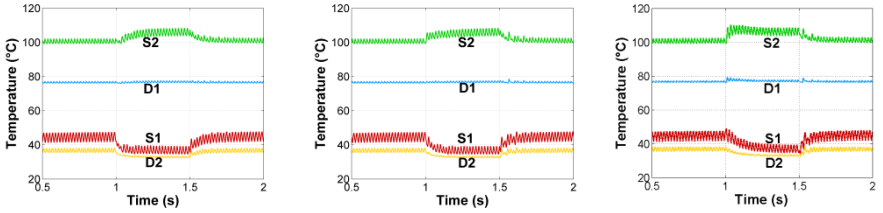

(a) (b) (c)

Fig. 3.11 Junction temperature dynamic response with a voltage dip time of 500 ms under three-phase ground fault ($Dip = 0.5\ p.u.$, $v_w = 11\ m/s$) (a) Phase a. (b) Phase b. (c) Phase c.

The junction temperatures of the switches and the diodes under different dip severity values of the single-phase grid fault and the three-phase grid fault are shown in Fig. 3.12 and Fig. 3.13, respectively. It is noted that, under both of the two fault conditions, when $Dip > 0.5\ p.u.$, the temperatures of the four devices are lower than that under the normal condition. When $Dip < 0.5\ p.u.$, the temperature of S_2 and D_1 are higher than that under the normal condition, while the temperatures of S_1 and D_2 are lower than that under the normal condition.

It should be noticed that the changes of the junction temperature with relation to the dip severity are different when Dip is below 0.5 p.u. and above 0.5 p.u. This is because there is 100% reactive current required by grid codes when $Dip < 0.5\ p.u.$; this will lead to a constant power factor within this range, whereas when $Dip > 0.5\ p.u.$, there are both active power and reactive power, which will result in a dramatically changed power factor. Additionally, special attention should be given to the power devices S_2 and D_1 under the LVRT operation of MMC. Those devices may have even higher junction temperature in some cases related to voltage level, power level, switching frequency and so on. These overloading conditions should

be taken into account when selecting the power devices and designing the heat sink system for the MMC.

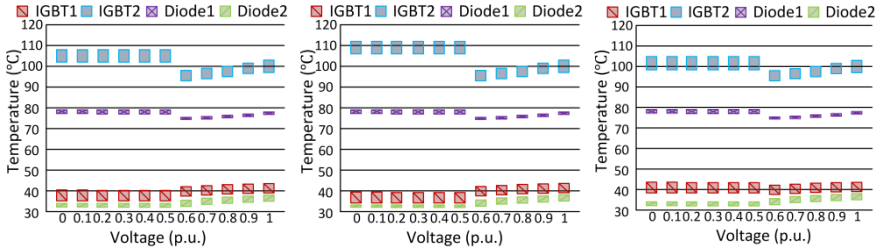

Fig. 3.12. Thermal distribution of the devices in grid-side MMC *vs*. grid voltage dip severity under single-phase ground fault ($v_w = 11$ m/s). (a) Phase a. (b) Phase b. (c) Phase c.

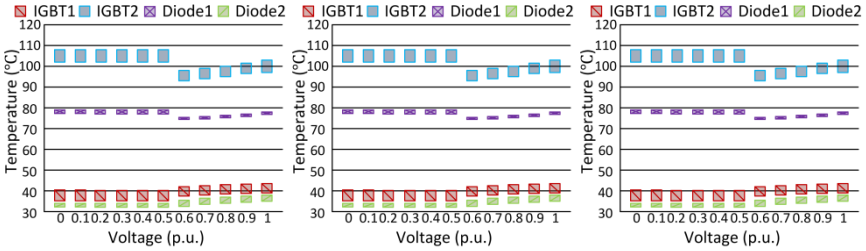

Fig. 3.13. Thermal distribution of the devices in grid-side MMC *vs*. grid voltage dip severity under three-phase ground fault ($v_w = 11\ m/s$). (a) Phase a. (b) Phase b. (c) Phase c.

3.3 Summary

As the loading conditions of the power devices in the MMC under grid faults are still not yet clarified, this chapter has focused on the investigation of the influence on different fault types and various grid voltage dips on the operating and loading behaviors of the MMC. The analyzing methods and results are of importance for understanding and improving the thermal performance of the MMC under grid fault condition.

Depending on the types and severity values of the grid faults, as well as LVRT control strategies, the operation status of the grid-connected MMC such as the output current, and the delivered power are significantly different. It is noticed that the operation conditions of the MMC are non-symmetrical among the three phases when unbalanced grid faults are present in the system.

The different grid fault types and severity values of voltage dips will aggravate the unbalanced loading of the devices. Some power devices under the LVRT operation may have even higher junction temperature than the normal full load operation condition. This overloading should be taken into account when choosing the power devices and designing the heat sink system for the wind power converter.

4 MMC State Observer Design

PS: In this project, the designed state observer of MMC in this chapter is used as a tool to localize the faulty module in next chapter. To make it clear to read and understand, the observer design is separated from the illustration of the fault diagnosis strategy. However, it should be noted that the designed state observer not only can be used to do the faulty diagnosis, but also is available for other functions like sensorless control.

In this chapter, a non-linear state observer based on the measurement of output currents and output voltages is proposed and studied in details which can be used to localize the faulty sub-module as explained in next chapter. The necessary and sufficient conditions are presented for MMC observability verification as well as the gain matrix calculation. No extra sensors are needed by this technique which decreases not only the investment but also avoids unpredictable failures of sensors and uncertainties caused by various noises. The effectiveness and the robustness of the proposed state observer are verified under different operation profiles such as fluctuation of transmission power, DC disturbances as well as AC disturbances.

4.1 Principle of MMC

4.1.1 Principle of MMC

The used MMC as well as the defined parameters are shown in Fig. 4.1. *R* denotes the resistor and *L* is the arm inductor.

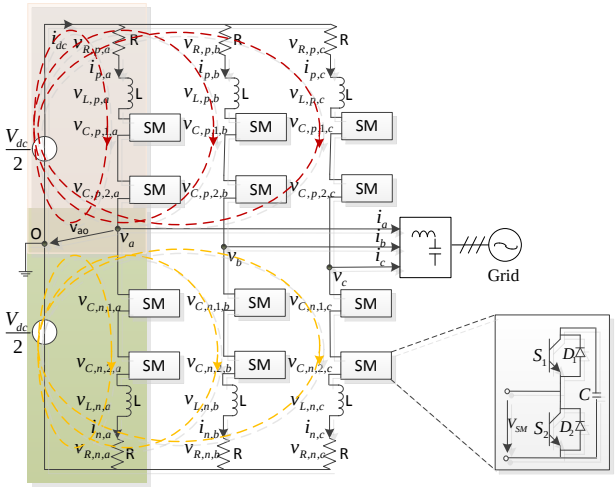

Fig. 4.1. The structure of Module Multilevel Converter (MMC).

As analyzed in the previous chapter, the MMC has four working regions which lead to different performance of capacitors as shown in Table 4.1 (Taking the first sub-module in phase A as an example). When the arm current $i_{p(n),k}$ is positive and S_1 is turned on and S_2 is turned off, the current flows through S_1 and the capacitor discharges, while when S_1 is turned off and S_2 is turned on, the current flows through D_2 and the capacitor maintains stable. When the arm current is negative and S_1 is turned on and S_2 is turned off, the current flows through D_1 and the capacitor charges, while when S_1 is turned off and S_2 is turned on, the current flows through S_2 and the capacitor voltage is maintained stable.

TABLE 4.1 FOUR WORKING REGIONS OF SUB-MODULE IN MMC

State no.	***Current***	***Status***	***Gating Signal***	***Arm Current Goes Through***	***Capacitor***	***Capacitor Voltage***
1*st*	$i_{p(n),k} > 0$	S_1on, S_2off	$g_{p(n),i,k} = 0$	D_1 and C	Charged	Increased
2*nd*	$i_{p(n),k} > 0$	S_1off, S_2on	$g_{p(n),i,k} = 1$	S_2	Bypassed	Stable
3*rd*	$i_{p(n),k} < 0$	S_1on, S_2off	$g_{p(n),i,k} = 0$	S_1 and C	Discharged	Decreased
4*th*	$i_{p(n),k} < 0$	S_1off, S_2on	$g_{p(n),i,k} = 1$	D_2	Bypassed	Stable

The dynamic equations which characterize the MMC as shown in Fig. 4.1 are expressed below. According to the Kirchhoff's voltage law, (4.1) and (4.2) can be obtained from the upper loops (in red) and the lower loops (in orange) which denote the relationship among the DC link voltages $\frac{V_{dc}}{2}$ and the voltage on the ith cells $v_{c,p(n),i,k}$, inductors $v_{L,p(n),k}$ and resistors $v_{R,p(n),k}$ in the upper arm and lower arm in phase k, respectively, $g_{p(n),i,k}$ are the driving signals for the cells, subscripts p and n are the upper arm and lower arm in each phase and $k = a, b, c$ represent the three phases. Equations (4.3)-(4.5) illustrate the relationship between the arm currents and the capacitor voltages, the arm inductor voltages and the arm resistor voltages. The relationship between the arm currents $i_{p(n),k}$ and the output currents i_k are obtained from Kirchhoff's current law and illustrated in equations (4.6) and (4.7).

$$\frac{V_{dc}}{2} = \sum_{i=1}^{N} g_{p,i,k} \cdot v_{c,p,i,k} + v_{L,p,k} + v_{R,p,k} + v_k \tag{4.1}$$

$$\frac{V_{dc}}{2} = \sum_{i=1}^{N} g_{n,i,k} \cdot v_{c,n,i,k} + v_{L,n,k} + v_{R,p,k} - v_k \tag{4.2}$$

$$g_{p(n),i,k} \cdot i_{p(n),k} = C \cdot \frac{dv_{c,p(n),i,k}}{dt} \tag{4.3}$$

$$g_{p(n),i,k} \cdot v_{L,p(n),k} = L \cdot \frac{di_{p(n),k}}{dt} \tag{4.4}$$

$$v_{R,p(n),k} = R \cdot i_{p(n),k} \tag{4.5}$$

$$i_{p,k} = \frac{i_{dc}}{3} + \frac{i_k}{2} + i_{cir,k} \tag{4.6}$$

$$i_{n,k} = \frac{i_{dc}}{3} - \frac{i_k}{2} + i_{cir,k} \tag{4.7}$$

By selecting the capacitor voltages and the output currents as the state variables, the above dynamical mathematical equations can be transferred into a state space model as follows:

$$\dot{v}_{c,p,i,k} = \frac{1}{C} g_{p,i,k} \cdot (\frac{i_{dc}}{3} + \frac{i_k}{2} + i_{cir,k}) \tag{4.8}$$

$$\dot{v}_{c,n,i,k} = \frac{1}{C} g_{n,i,k} \cdot (\frac{i_{dc}}{3} - \frac{i_k}{2} + i_{cir,k}) \tag{4.9}$$

$$\dot{i}_k = \frac{1}{L} (\sum_{i=1}^{N} g_{n,i,k} \cdot v_{c,n,i,k} - \sum_{i=1}^{N} g_{p,i,k} \cdot v_{c,p,i,k} - R \cdot i_k - 2v_k) \tag{4.10}$$

4.1.2 Observability analysis of MMC

Before explaining the observer design process, it is essential to analyze the observability property of the MMC.

Denote the system state matrix and the system input matrix as F and H.

$$F = \begin{bmatrix} \frac{1}{C} g_{p,i,k} \cdot \left(\frac{i_k}{2} + i_{cir,k}\right) \\ \frac{1}{C} g_{n,i,k} \cdot \left(-\frac{i_k}{2} + i_{cir,k}\right) \\ \frac{1}{L} (\sum_{i=1}^{N} g_{n,i,k} \cdot v_{c,n,i,k} - \sum_{i=1}^{N} g_{p,i,k} \cdot v_{c,p,i,k} - R \cdot i_k - 2v_k) \end{bmatrix} \tag{4.11}$$

$$H = \begin{bmatrix} \frac{1}{C} g_{p,i,k} \\ \frac{1}{C} g_{n,i,k} \\ 0 \end{bmatrix} \tag{4.12}$$

According to the observability criterion of the nonlinear and time-varying system [91], the observability analysis is performed by computing the rank of the following Jacobian matrix J with respect to the state variables.

$$J = [H, [F, H]] \tag{4.13}$$

in which $[F, H]$ is the Lie bracket operation and can be calculated as given below

$$[F, H] = \frac{\partial F}{\partial x} H - \frac{\partial H}{\partial x} F \tag{4.14}$$

where

$$\frac{\partial H}{\partial x} = 0 \tag{4.15}$$

And

$$\frac{\partial F}{\partial x} = \begin{bmatrix} \frac{\partial F_1}{\partial x_1} & \frac{\partial F_1}{\partial x_2} & \frac{\partial F_1}{\partial x_3} \\ \frac{\partial F_2}{\partial x_1} & \frac{\partial F_2}{\partial x_2} & \frac{\partial F_2}{\partial x_3} \\ \frac{\partial F_3}{\partial x_1} & \frac{\partial F_2}{\partial x_2} & \frac{\partial F_3}{\partial x_3} \end{bmatrix} \tag{4.16}$$

Thus, the Jacobian matrix is calculated as

$$J = \begin{bmatrix} \frac{1}{C} g_{p,i,k} & \frac{1}{2C^2} g_{p,i,k}^2 \\ \frac{1}{C} g_{n,i,k} & -\frac{1}{2C^2} g_{n,i,k}^2 \\ 0 & -\frac{R}{CL} g_{p,i,k} + \frac{1}{CL} g_{n,i,k} \cdot \sum_{i=1}^{N} g_{p,i,k} \end{bmatrix} \tag{4.17}$$

As the rank of the Jacobian matrix is equal to 3 which is the number of state variables, the system is observable.

4.2 State observer design of MMC

In the engineering practice, an observer is designed to provide an estimation of the actual state value at current time. An asymptotic observer is designed for the MMC system as given in equations (4.1)-(4.7). By an asymptotic observer, the estimated capacitor voltages $\hat{v}_{c,p,i,k}$ and $\hat{v}_{c,n,i,k}$ converge to the plant state $v_{c,p,i,k}$ and $v_{c,n,i,k}$ as $t \to \infty$.

4.2.1 Observer model of MMC

Fig. 4.2 illustrates the MMC observer execution process in practice. It can be seen that the observer consists of an MMC state space model as shown in the purple part in Fig. 4.2 and an estimation error correction by using a gain matrix G as highlighted in the red part. In order to obtain the estimation of the MMC state from the observer model and construct the gain matrix G, the signals available from the actual MMC plant (blue part) are gathered such as the DC-link voltage V_{dc} , the output currents $i_{a,b,c}$ and the output voltages $v_{a,b,c}$.

The observer model can be written as

$$\dot{\hat{v}}_{c,p,i,k} = \frac{1}{C} g_{p,i,k} \cdot \left(\frac{i_{dc}}{3} + \frac{\hat{i}_k}{2} + \hat{\imath}_{cir,k}\right) + g g_{p,i} \cdot f(i_k - \hat{i}_k) \tag{4.18}$$

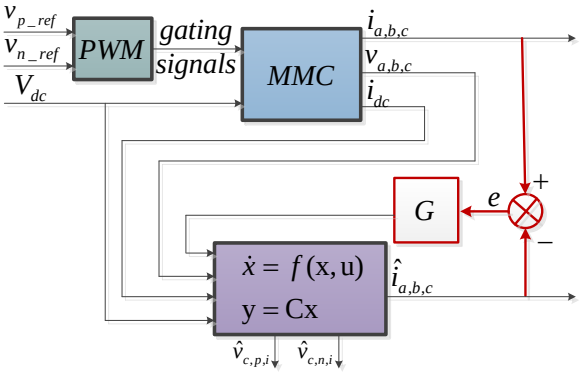

Fig. 4.2. Flow diagram of the proposed observer.

$$\dot{\hat{v}}_{c,n,i,k} = \frac{1}{C} g_{n,i,k} \cdot \left(\frac{i_{dc}}{3} - \frac{\hat{i}_k}{2} + \hat{i}_{cir,k}\right) + gg_{n,i} \cdot f(i_k - \hat{i}_k) \tag{4.19}$$

$$\dot{\hat{i}}_k = \frac{1}{L}\left(\sum_{i=1}^{N} g_{n,i,k} \cdot \hat{v}_{c,n,i,k} - \sum_{i=1}^{N} g_{p,i,k} \cdot \hat{v}_{c,p,i,k} - R \cdot \hat{i}_k - 2v_k\right) + gg_k \cdot f(i_k - \hat{i}_k) \tag{4.20}$$

where, $\hat{v}$ and $\hat{\imath}$ are the estimation values, $gg_{p,i}, gg_{n,i}, gg_k$ are the elements of the gain matrix G which should be set to satisfy the fast dynamic response and acceptable convergence characteristics of the estimated capacitor voltage curves. Assuming zero estimation errors for the output current, the error equation $f(i_k - \hat{i}_k)$ is stated as:

$$f(x) = \begin{cases} -1, & x < -1 \\ 0, & -1 < x < 1 \\ 1, & x > 1 \end{cases} \tag{4.21}$$

4.2.2 Gain matrix calculation

The performance of the designed observer is evaluated by the observation error. Subtracting the state space model from the observer model, the observation error dynamics for the developed observer can easily be obtained and they are given as:

$$\dot{\tilde{v}}_{c,p,i,k} = \dot{v}_{c,p,i,k} - \dot{\hat{v}}_{c,p,i,k} = \frac{1}{C} g_{p,i,k} \cdot \left(\frac{i_k}{2} - \frac{\hat{i}_k}{2} + i_{cir,k} - \hat{i}_{cir,k}\right) - gg_{p,i} \cdot f(i_k - \hat{i}_k) \tag{4.22}$$

$$\dot{\tilde{v}}_{c,n,i,k} = \dot{v}_{c,n,i,k} - \dot{\hat{v}}_{c,n,i,k} = \frac{1}{C} g_{n,i,k} \cdot \left(\frac{\hat{i}_k}{2} - \frac{i_k}{2} + i_{cir,k} - \hat{i}_{cir,k}\right) - gg_{n,i} \cdot f(i_k - \hat{i}_k) \tag{4.23}$$

$$\dot{\hat{i}}_k = \frac{1}{L}\left(\sum_{i=1}^{N} g_{n,i,k}\cdot\left(v_{c,n,i,k}-\hat{v}_{c,n,i,k}\right)-\sum_{i=1}^{N} g_{p,i,k}\cdot\left(v_{c,p,i,k}-\hat{v}_{c,p,i,k}\right)-R\cdot\left(\hat{i}_k-i_k\right)\right)-gg_k\cdot f(i_k-\hat{i}_k) \tag{4.24}$$

where

$$\tilde{v}_{c,p,i,k} = v_{c,p,i,k}-\hat{v}_{c,p,i,k} \tag{4.25}$$

$$\tilde{v}_{c,n,i,k} = v_{c,n,i,k}-\hat{v}_{c,n,i,k} \tag{4.26}$$

$$\tilde{i}_k = i_k-\hat{i}_k \tag{4.27}$$

$$\tilde{i}_{cir,k} = i_{cir,k}-\hat{i}_{cir,k} \tag{4.28}$$

With zero observation errors, the observer will give the best results. Otherwise, the observation errors should at least be in steady state. To meet the requirement, the objective function

$$V_e = \frac{1}{2}(\tilde{i}_k^2+\sum_{i=1}^{N} g_{p,i,k}\cdot\tilde{v}_{c,p,i,k}^2+\sum_{i=1}^{N} g_{n,i,k}\cdot\tilde{v}_{c,n,i,k}^2) \tag{4.29}$$

is constructed, whose time d

$$\dot{V}_e = \tilde{i}_k\cdot\dot{\tilde{i}}_k+\sum_{i=1}^{N} g_{p,i,k}\cdot\tilde{v}_{c,p,i,k}\cdot\dot{\tilde{v}}_{c,p,i,k}+\sum_{i=1}^{N} g_{n,i,k}\cdot\tilde{v}_{c,n,i,k}\cdot\dot{\tilde{v}}_{c,n,i,k} \tag{4.30}$$

Substitute (4.22)-(4.28) to (4.30) yields

$$\begin{aligned}\dot{V}_e = \tilde{i}_k\cdot(&\frac{1}{L}\left(\sum_{i=1}^{N} g_{n,i,k}\cdot\tilde{v}_{c,n,i,k}-\sum_{i=1}^{N} g_{p,i,k}\cdot\tilde{v}_{c,p,i,k}-R\cdot\tilde{i}_k\right)-gg_k\cdot f(\tilde{i}_k))\\&+\sum_{i=1}^{N} g_{p,i,k}\cdot\tilde{v}_{c,p,i,k}\cdot(\frac{1}{C}g_{p,i,k}\cdot\left(\frac{\tilde{i}_k}{2}+\tilde{i}_{cir,k}\right)-gg_{p,i}\cdot f(\tilde{i}_k))\\&+\sum_{i=1}^{N} g_{n,i,k}\cdot\tilde{v}_{c,n,i,k}\cdot(\frac{1}{C}g_{n,i,k}\cdot\left(\frac{\tilde{i}_k}{2}+\tilde{i}_{cir,k}\right)-gg_{n,i}\cdot f(\tilde{i}_k))\end{aligned} \tag{4.31}$$

By grouping the three state variables together, respectively, it is possible to obtain

$$\dot{V}_e = -\frac{R}{L} i_k^2 + \tilde{i}_k \cdot \left[\left(\frac{1}{2C} + \frac{1}{L} \right) \cdot \sum_{i=1}^{N} g_{n,i,k} \cdot \tilde{v}_{c,n,i,k} + \left(\frac{1}{2C} - \frac{1}{L} \right) \cdot \sum_{i=1}^{N} g_{p,i,k} \cdot \tilde{v}_{c,p,i,k} - g_k \cdot f(\tilde{i}_k) \right] + \sum_{i=1}^{N} g_{p,i,k} \cdot \tilde{v}_{c,p,i,k} \cdot \left[\frac{1}{C} \cdot \tilde{i}_{cir,k} - gg_{p,i} \cdot f(\tilde{i}_k) \right] + \sum_{i=1}^{N} g_{n,i,k} \cdot \tilde{v}_{c,n,i,k} \cdot \left[\frac{1}{C} \cdot \tilde{i}_{cir,k} - gg_{n,i} \cdot f(\tilde{i}_k) \right] \tag{4.32}$$

To ensure $\dot{V}_e < 0$ under all situations, the following inequalities should be satisfied.

$$\left(\frac{1}{2C} + \frac{1}{L} \right) \cdot \sum_{i=1}^{N} g_{n,i,k} \cdot \tilde{v}_{c,n,i,k} + \left(\frac{1}{2C} - \frac{1}{L} \right) \cdot \sum_{i=1}^{N} g_{p,i,k} \cdot \tilde{v}_{c,p,i,k} < gg_k \tag{4.33}$$

$$\frac{1}{C} \cdot \tilde{i}_{cir,k} < gg_{p,i} \tag{4.34}$$

$$\frac{1}{C} \cdot \tilde{i}_{cir,k} < gg_{n,i} \tag{4.35}$$

Thus, the gain matrix G can be obtained.

4.3 Simulation results

To evaluate the performance of the proposed observer, a simulation study is conducted based on the specifications listed in Table 2.1, according to which, the gain matrix is obtained as $gg_{p,i} = 2500, gg_{n,i} = 2500, gg_k = 300000$. Moreover, to further illustrate the effectiveness of the designed observer, the estimation results under different loading profile, such as fluctuated transmission power, DC voltage disturbances and AC voltage disturbances are displayed.

A. Case I: Normal AC grid condition

Fig. 4.3 shows the outputs of the MMC and the signals in the designed state observer under normal condition. The output phase voltages v_a, v_b, v_c, the load current i_a and the arm currents $i_{p,a}$, $i_{n,a}$ in phase a of MMC are displayed in Fig. 4.3 (a) and (b), respectively. The distortion of the outputs voltage is caused by the charging and discharging of the capacitors. The measured upper arm capacitor voltages $v_{c,p,1,a}$~$v_{c,p,12,a}$ and lower arm capacitor voltages $v_{c,n,1,a}$~$v_{c,n,12,a}$ in Phase A are shown in the first figure of Fig. 4.3 (c). The balanced capacitor voltage is ensured at a reference voltage (31800 V/12 = 2650 V) with a fluctuation of around 5% by employing the capacitor voltage balance algorithm which shares the same idea as that given in [92]. The estimated upper arm capacitor voltages $\hat{v}_{c,p,1,a}$~$\hat{v}_{c,p,12,a}$ and lower arm capacitor voltages $\hat{v}_{c,n,1,a}$~$\hat{v}_{c,n,12,a}$ are given in Fig.

4.3 (d) (in the figures, $Ev_{c,p(n),i,k}$ means $\hat{v}_{c,p(n),i,k}$). All the errors between the measured capacitor voltages and the estimated capacitor voltages present a small value as identified in Fig. 4.3 (e). From the estimation results it can be seen that the estimation errors are very small (maximum estimation error 0.75 %) and the output from the observer can be used for both the control and fault detection purposes.

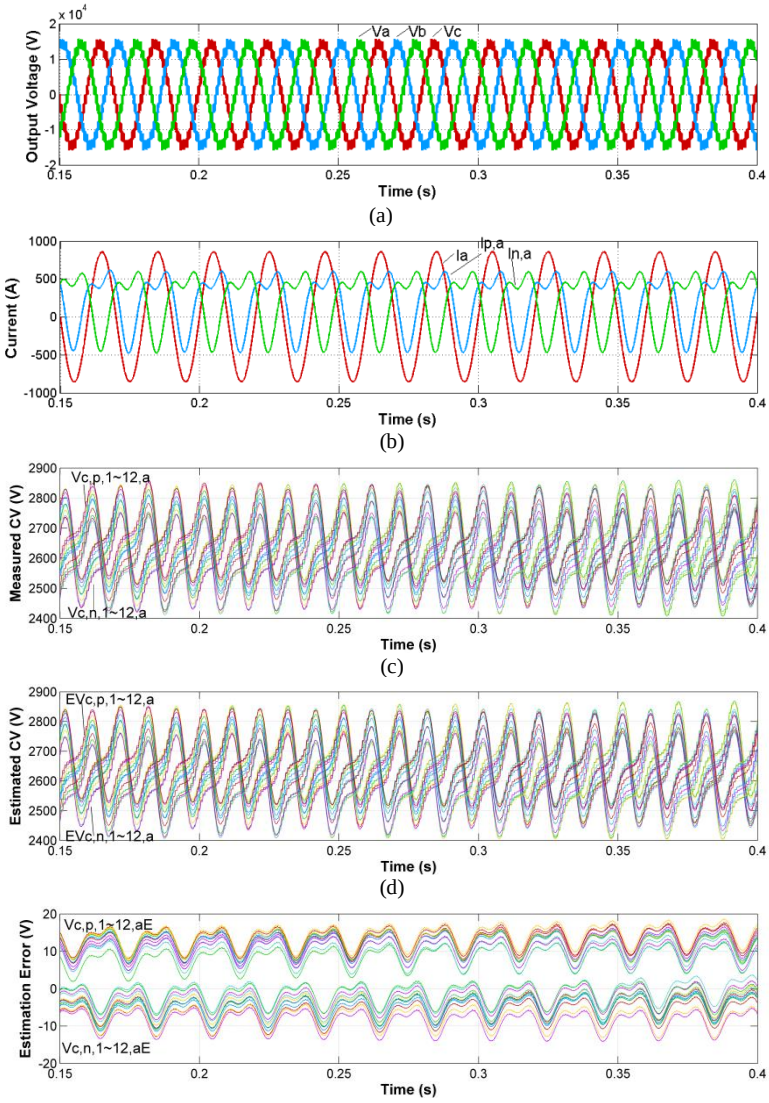

Fig. 4.3. Performance of grid-side MMC and observer under normal operation condition (a) Output phase voltage of MMC; (b) Load current and arm currents in phase A; (c) Measured capacitor voltage; (d) Estimated capacitor voltage; (e) Estimation error. (CV: Capacitor Voltage).

B. Case II: Change of delivered power

The transmission power reduces to half the rated value at $t = 0.2\ s$ and recoveries to rate value at $t = 0.26\ s$. The corresponding outputs are shown in Fig. 4.4. The estimation error is still within 0.75 %, which can be seen from Fig. 4.4 (e).

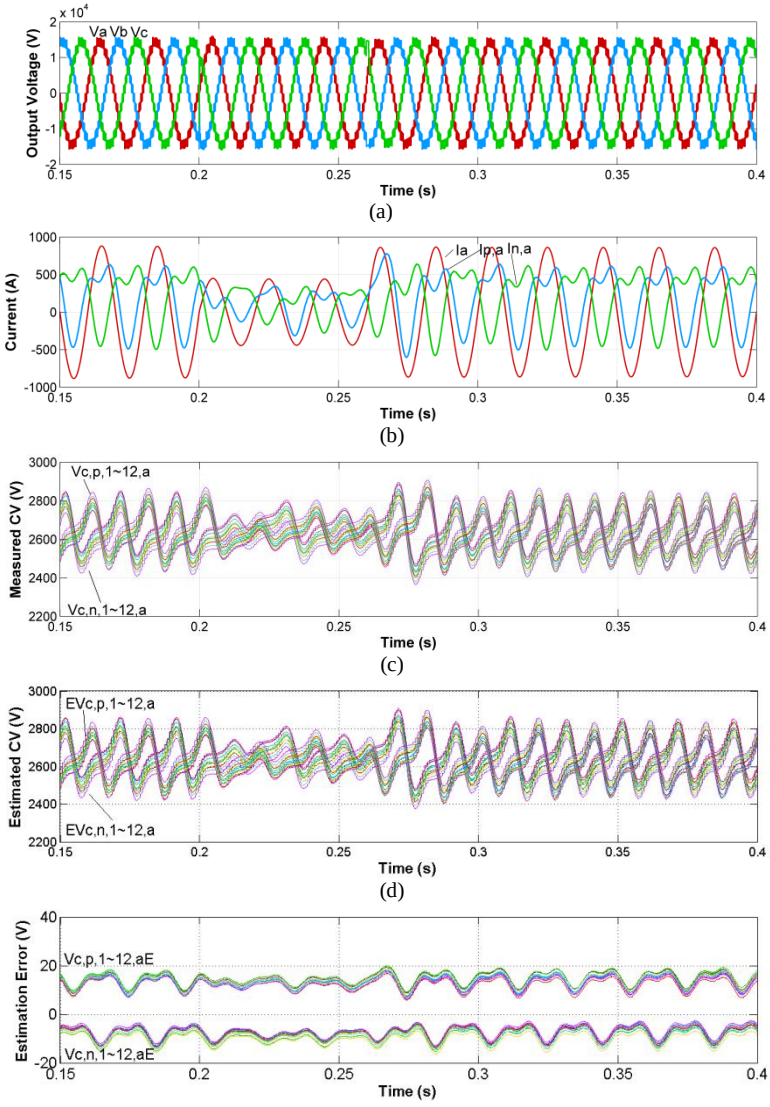

Fig. 4.4. Performance of MMC and observer under different transmission power (a) Output phase voltage of MMC; (b) Load current and arm currents in phase A; (c) Measured capacitor voltage; (d) Estimated capacitor voltage; (e) Estimation error. (CV: Capacitor Voltage).

C. Case III: Change of DC voltage

The dynamic performance of MMC under 50% DC voltage drop appearing at $t = 0.2\ s$ and disappearing at $t = 0.26\ s$ is shown in Fig. 4.5. The estimation error, as shown in Fig. 4.5 (e), is in the range of 0.75 %.

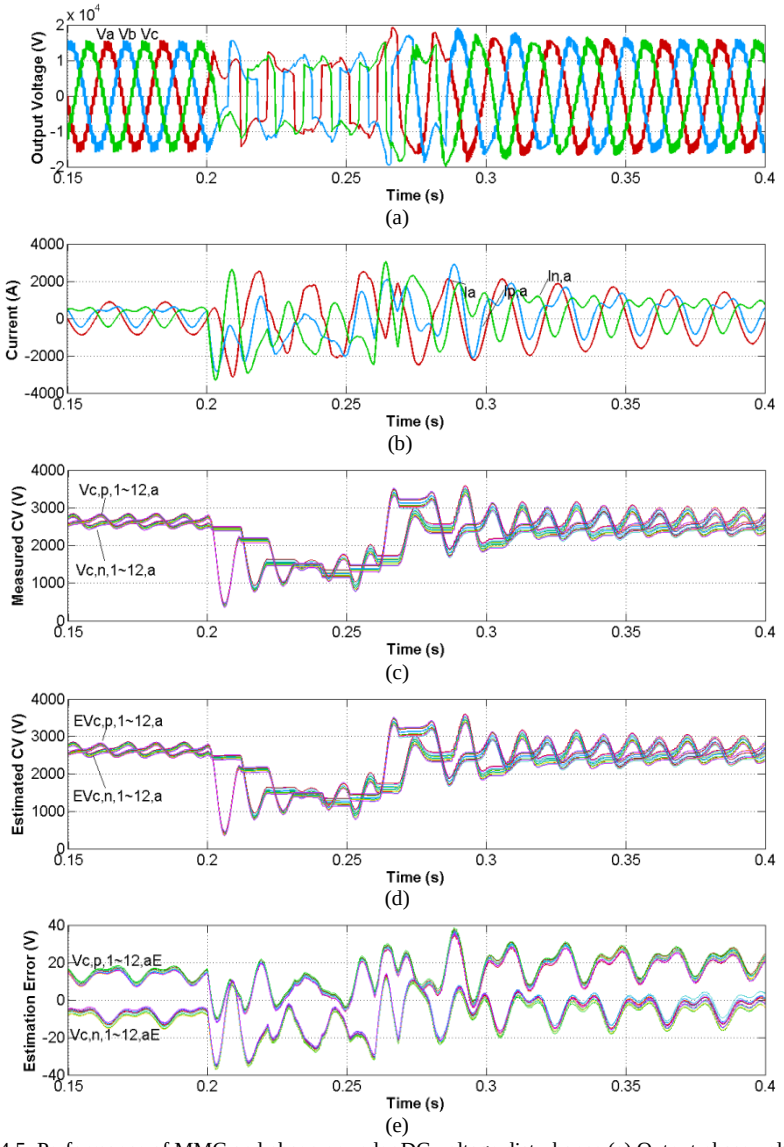

Fig. 4.5. Performance of MMC and observer under DC voltage disturbance (a) Output phase voltage of MMC; (b) Load current and arm currents in phase A; (c) Measured capacitor voltage; (d) Estimated capacitor voltage; (e) Estimation error. (CV: Capacitor Voltage).

D. Case IV: Grid voltage disturbance

Fig. 4.6 shows the MMC and observer performance when the grid voltage dips to at $t = 0.2\ s$ and recoveries to normal value at $t = 0.26\ s$. It can be seen that the observer works quite well under this situation.

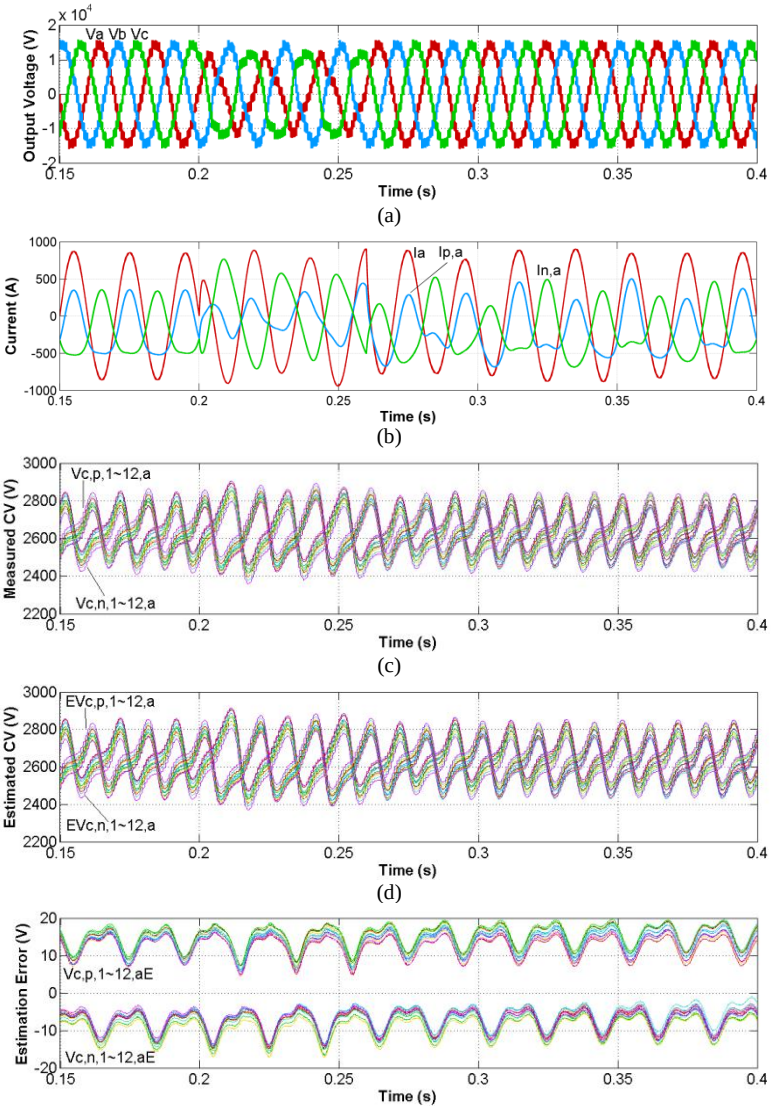

Fig. 4.6. Performance of MMC and observer under grid voltage disturbance (a) Output phase voltage of MMC; (b) Load current and arm currents in phase A; (c) Measured capacitor voltage; (d) Estimated capacitor voltage; (e) Estimation error. (CV: Capacitor Voltage).

E. Case V: Three-phase to ground fault

Fig. 4.7 shows the MMC and observer performance when a three-phase to ground fault ($dip = 0.5$) happens at $t = 0.2\ s$ and back to normal at $t = 0.26\ s$. It can be seen that the results of the observer can follow the measured capacitor voltages.

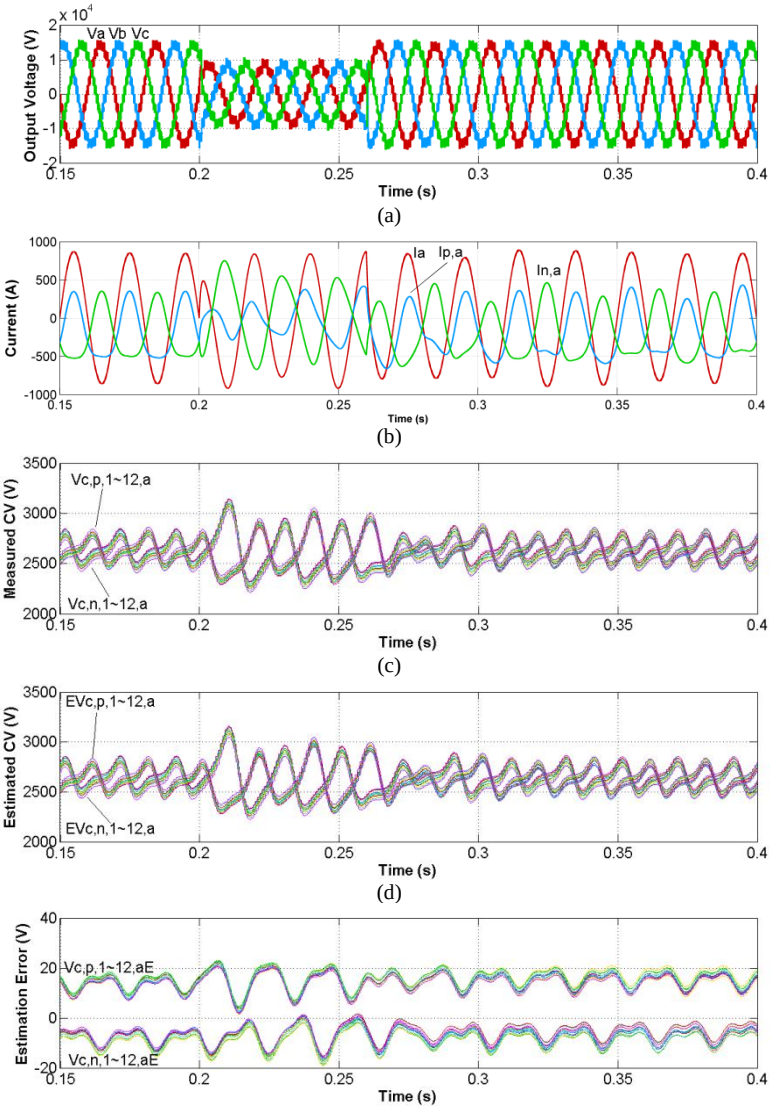

Fig. 4.7. Performance of MMC and observer under three-phase to ground fault (a) Output phase voltage of MMC; (b) Load current and arm currents in phase A; (c) Measured capacitor voltage; (d) Estimated capacitor voltage; (e) Estimation error. (CV: Capacitor Voltage).

4.4 Summary

In this chapter, a state observer of MMC is established to estimate the capacitor voltage in each module under not only normal operation condition, but also various condition disturbances, which verifies both the effectiveness and the robustness of the proposed state observer. No additional sensors are required by this technique which not only decreases the investment but also avoid unpredictable failures of sensors and uncertainties caused by various noise sources.

Other contributions of this chapter are the verification of the observability of the MMC and the calculation of the gain matrix, which is introduced in detail and could be a reference for those non-linear switching systems.

5 Fault Diagnosis of MMC

Once the observer is ready to use, it is possible to estimate the states in MMC system such as arm currents, capacitor voltages and so on. However, the failure of the semiconductor device is common due to the large number of switching devices in the MMC. It should be noted that the observer is designed based on the schematics of the MMC and the observer is not valid under the switching device faults condition as the structure of MMC is changed due to the faults. Therefore, the switching device fault mechanism as well as the corresponding observer modification strategies is discussed in this chapter in order to be able to identify the device faults in the MMC.

Once the power devices come to the end of life or experience any kind of fault, they are expected to be detected, diagnosed and localized as early and fast as possible in order to reduce the maintenance time and avoid damage to other parts in the MMC system. In this chapter, a fault diagnosis method of MMC is proposed to detect the fault, localize the faulty module as well as identify the faulty switch. The effectiveness of this method is verified under external disturbances, various faults, even under multiple module fault and multiple device fault situations.

It is also expected that the fault diagnosis method can effectively and precisely locate the faulty modules and faulty power devices, even without increasing the implementation complexity. It is important that the diagnosis method should be valid under all kinds of driving signal generating methods and system control strategies, even under some external disturbances and fault situations in order to avoid false diagnosis**.**

5.1 Basic idea of the fault diagnosis method in MMC

It is desirable that fault diagnostic method utilizes variables which are already used by the control system in order to avoid extra sensors and involving extra complexity and costs of the system. The proposed diagnostic algorithm uses the output currents $i_k$and capacitor voltages $v_{c,p(n),i,k}$, which can be easily obtained from the control system.

The diagram of the proposed fault diagnosis method is shown in Fig. 5.1, which is divided into three parts, fault detection, faulty module localization and faulty device identification. In the fault detection stage, the output current i_k is evaluated continuously to detect if there is fault happened to MMC. Once there is fault in the system, the faulty module localization stage is activated and the faulty module can

be localized. If faulty device is expected, the third stage—faulty device identification stage is triggered and the faulty device can be identified.

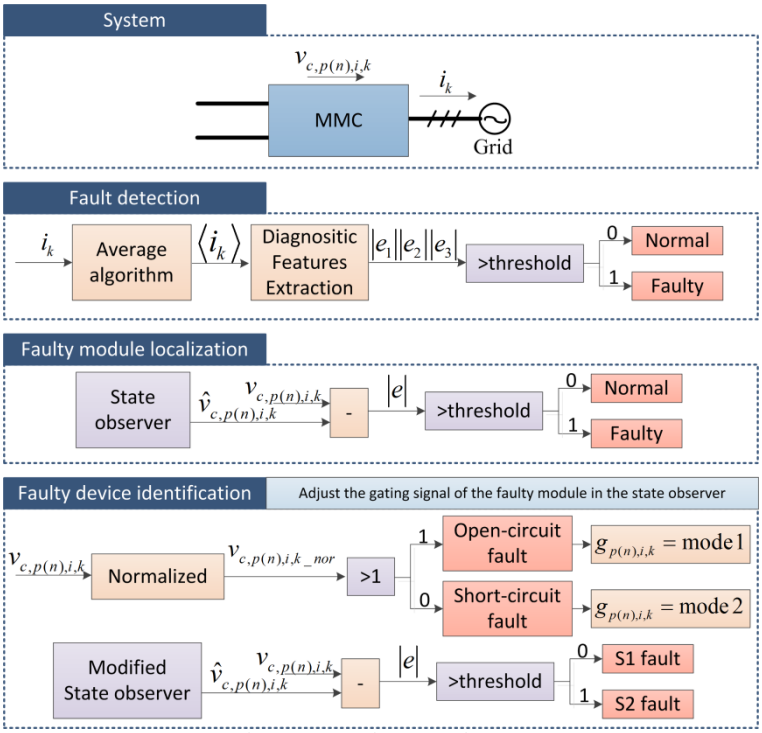

Fig. 5.1. Framework of the proposed fault identification method in the MMC.

5.2 Fault detection

The averaged values of the output currents i_k are calculated first as expressed in equation (5.1)

$$\langle i_k \rangle = \frac{1}{T}\int_{\alpha}^{\alpha+T} i_k dt \tag{5.1}$$

$\langle i_k \rangle$ is the averaged output current and three diagnosis features are defined as below to detect the occurrence of failures in any of its phases

$$\begin{cases} e_1 = \langle i_a \rangle - \langle i_b \rangle \\ e_2 = \langle i_a \rangle - \langle i_c \rangle \\ e_3 = \langle i_b \rangle - \langle i_c \rangle \end{cases} \tag{5.2}$$

Under normal condition, the output currents are balanced and the three diagnosis features are near to zero. If any fault occurs, all the output currents will be affected and the diagnosis variables e_1, e_2, e_3 will be different from those under normal

condition. Therefore, the fault can be detected when the absolute values of the diagnosis variables e_1, e_2, e_3 are larger than the threshold $k_{detection}$ and it lasts for 100 sampling time.

5.3 Faulty module localization

Once the fault is detected, the faulty module localization stage is activated. The state observer proposed in Chapter 4 is triggered to obtain the estimated capacitor voltage $\hat{v}_{c,p(n),i,k}$. By comparing the measured capacitor voltage $v_{c,p(n),i,k}$ and the corresponding estimated capacitor voltage $\hat{v}_{c,p(n),i,k}$, the estimation errors can be obtained. Those sub-modules with estimation errors larger than the given threshold $k_{localization}$ and it lasts for 100 sampling time are considered as the faulty modules.

The state observer is designed based on the schematics of the MMC, but the observer is not valid under the fault condition as the structure of MMC is changed due to the faults. When the structure of the MMC is changed while the state observer is kept stable, the output of the real MMC and the output of the state observer will be different. Based on this mechanism, the faulty module can be localized.

5.4 Faulty device identification

When there is fault occurs, the structure of the MMC is changed. Different with faulty module localization stage, in the faulty device identification stage, the state observer is modified into the fault mode to estimate the capacitor voltages in the faulty module.

Since the capacitor voltage in the faulty module increases if the open-circuit fault occurs in S_1 or S_2 and the capacitor voltage in the faulty module decreases to zero if the short-circuit fault occurs in S_1 or S_2 (this will be explained in the following), the fault type (open-circuit fault or short-circuit fault) can be identified. To identify the S_1 open-circuit fault and S_2 open-circuit fault, the modification strategy of the observer for the S_1 open-circuit fault is analyzed and to identify the S_1 short-circuit fault and S_2 short-circuit fault, the modification strategy of the observer for the S_2 short-circuit fault is analyzed. Therefore, four kinds of faults in MMC, S_1 open-circuit fault, S_2 open-circuit fault, S_1 short-circuit fault and S_2 short-circuit fault, are considered here and two modification modes of the state observer are defined to estimate the corresponding capacitor voltages under those fault conditions.

After the faulty module is localized, the faulty device identification stage is activated. First, the fault type is judged according to the normalized value of the measured capacitor voltage in the faulty module. If the normalized value is larger

than 1, it is the open-circuit fault in S_1 or S_2. The state observer proposed in Chapter 4 is adjusted into open mode (actually, it is the driving signal of the faulty module is adjusted into open mode and it will be illustrated in the following), if the difference between the estimated capacitor voltage in the faulty module $\hat{v}_{c,p(n),i,k}$ and the measured capacitor voltage in the faulty module $v_{c,p(n),i,k}$ is smaller than $k_{identification_open}$and it can last for 100 sampling time, the faulty device is S_1, if the difference is larger than $k_{identification_open}$and it can last for 100 sampling time, the faulty device is S_2. If the normalized value is smaller than 1, it is the short-circuit fault in S_1 or S_2. The state observer is adjusted into short mode , if the difference between the estimated capacitor voltage in the faulty module $\hat{v}_{c,p(n),i,k}$ and the measured capacitor voltage in the faulty module $v_{c,p(n),i,k}$ is smaller than $k_{identification_short}$and it can last for 100 sampling time, the faulty device is S_2, if the difference is larger than $k_{identification_short}$and it can last for 100 sampling time, the faulty device is S_1.

TABLE 5.1 FAULTY DEVICE IDENTIFICATION

Normalized capacitor voltage in the faulty module	***Estimation error in the faulty module***	***Faulty device***
$v_{c,p(n),i,k\_nor} > 1$	$e < k_{identification\_open}$	S1 Open
	$e > k_{identification\_open}$	S2 Open
$v_{c,p(n),i,k\_nor} < 1$	$e > k_{identification\_short}$	S1 Short
	$e < k_{identification\_short}$	S2 Short

5.4.1 Operation analysis of sub-module under fault conditions

There are mainly two types of failures in the switching devices dependent on different IGBT package types: open-circuit fault which appears in bond-wired packaging device due to the lifting of the bonding wires in a switch module caused by over-temperature; short-circuit fault in both the bond-wired packaging and press packaging devices which may be caused by wrong gating signals, overvoltage, or high temperature. It should be noted that in order to illustrate the performance of the MMC under different device faults, extra hardware protection action is not taken into account in the analysis. The open-circuit and short-circuit faults in a sub-module concerning the failures of the switching devices S_1 and S_2 are shown in Fig. 5.2. The analysis of the operation performance of the sub-modules which suffer open-circuit and short-circuit faults concerning the failures of the switching devices S_1 and S_2 is given below.

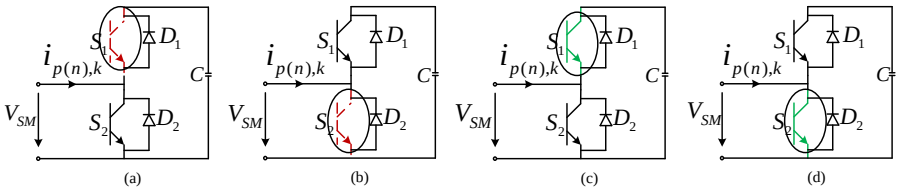

Fig. 5.2. Failure modes of the modules (a) Open-circuit fault in S1; (b) Open-circuit fault in S2; (c) Short-circuit fault in S1; (d) Short-circuit fault in S2.

1) Open-circuit fault in S_1 (Fig. 5.1 (a)): as shown in Table 5.2, the sub-module operates normally when the arm current $i_{p(n),k} > 0$, the arm current still goes through D_1 to charge the capacitor when the gating signal $g_{p(n),i,k} = 0$, the arm current flows through S_2 to bypass the capacitor when the gating signal $g_{p(n),i,k} = 1$; When $i_{p(n),k} < 0$, the module is in normal operation when $g_{p(n),i,k} = 1$, the arm current flows through D_2, the capacitor is bypassed and the capacitor voltage is stable; However, when the gating signal $g_{p(n),i,k} = 0$, the arm current will be forced to go through D_2 instead of S_1 and the capacitor voltage is maintained stable, as shown in orange in the table;

TABLE 5.2 FAILURE MECHANISM OF OPEN-CIRCUIT FAULT IN S1

State no.	*Current*	*Status*	*Gating Signal*	*Arm Current Goes Through*	*Capacitor*	*Capacitor Voltage*
1*st*	$i_{p(n),k} > 0$	S_1on, S_2off	$g_{p(n),i,k} = 0$	D_1 and C	Charged	Increased
2*nd*	$i_{p(n),k} > 0$	S_1off, S_2on	$g_{p(n),i,k} = 1$	S_2	Bypassed	Stable
3*rd*	$i_{p(n),k} < 0$	S_1on, S_2off	$g_{p(n),i,k} = 0$	D_2	Bypassed	Stable
4*th*	$i_{p(n),k} < 0$	S_1off, S_2on	$g_{p(n),i,k} = 1$	D_2	Bypassed	Stable

2) Open-circuit fault in S_2 (Fig. 5.1 (b)): as shown in Table 5.3, the sub-module operates as normal when the arm current is positive and $g_{p(n),i,k} = 0$; if S_1 is turned off, S_2 is turned on, the arm current is forced to go through D_1 to charge the capacitor instead of S_2 to bypass the capacitor; when the arm current $i_{p(n),k} < 0$, the module is in normal operation;

TABLE 5.3 FAILURE MECHANISM OF OPEN-CIRCUIT FAULT IN S2

State no.	*Current*	*Status*	*Gating Signal*	*Arm Current Goes Through*	*Capacitor*	*Capacitor Voltage*
1*st*	$i_{p(n),k} > 0$	S_1on, S_2off	$g_{p(n),i,k} = 0$	D_1 and C	Charged	Increased
2*nd*	$i_{p(n),k} > 0$	S_1off, S_2on	$g_{p(n),i,k} = 1$	D_1 and C	Charged	Increased
3*rd*	$i_{p(n),k} < 0$	S_1on, S_2off	$g_{p(n),i,k} = 0$	S_1 and C	Discharged	Decreased
4*th*	$i_{p(n),k} < 0$	S_1off, S_2on	$g_{p(n),i,k} = 1$	D_2	Bypassed	Stable

3) Short-circuit fault in S_1 (Fig. 5.1 (c)): as shown in Table 5.4, when the short-circuit fault happens in S_1, the sub-module operates as normal if S_1 is turned on and the complementary S_2 is turned off; at once S_2 is turned on, the capacitor is discharged through the capacitor discharging loop which is formed by the short-circuited S_1, the complementary S_2 and the capacitor if no protective action is taken. Due to the small time constant of the capacitor discharging loop, the capacitor is discharged quickly which leads to rapid declines of the capacitor voltage and a large short-circuit current in the faulty module. The large short-circuit current makes S_2 open-circuited. As a result, the arm current goes through short-circuited S_1 and the capacitor.

TABLE 5.4 FAILURE MECHANISM OF SHORT-CIRCUIT FAULT IN S1

State no.	*Current*	*Status*	*Gating Signal*	*Arm Current Goes Through*	*Capacitor*	*Capacitor Voltage*
1*st*	$i_{p(n),k} > 0$	S_1on, S_2off	$g_{p(n),i,k} = 0$	Short-circuited $S_1$and C	Charged	Increased
2*nd*	$i_{p(n),k} > 0$	S_1off, S_2on	$g_{p(n),i,k} = 1$	Short-circuited $S_1$and C	Charged	Increased
3*rd*	$i_{p(n),k} < 0$	S_1on, S_2off	$g_{p(n),i,k} = 0$	Short-circuited $S_1$and C	Discharged	Decreased
4*th*	$i_{p(n),k} < 0$	S_1off, S_2on	$g_{p(n),i,k} = 1$	Short-circuited $S_1$and C	Discharged	Decreased

4) Short-circuit fault in S_2 (Fig. 5.1 (d)): similar with the short-circuit fault in S_1, when the short-circuit fault happens in S_2, the sub-module operates as normal if S_2 is turned on and the complementary S_1 is turned off; When S_1 is turned on, the capacitor is discharged through the capacitor discharging loop which is composed by the short-circuited S_2, the complementary S_1 and the capacitor if no protective action is taken. S_1 will be destroyed and the current will go through the short-circuited S_2 independent on the direction of the arm current, as shown in Table 5.5.

TABLE 5.5 FAILURE MECHANISM OF SHORT-CIRCUIT FAULT IN S2

State no.	*Current*	*Status*	*Gating Signal*	*Arm Current Goes Through*	*Capacitor*	*Capacitor Voltage*
1*st*	$i_{p(n),k} > 0$	S_1on, S_2off	$g_{p(n),i,k} = 0$	Short-circuited S_2	Bypassed	Zero
2*nd*	$i_{p(n),k} > 0$	S_1off, S_2on	$g_{p(n),i,k} = 1$	Short-circuited S_2	Bypassed	Zero
3*rd*	$i_{p(n),k} < 0$	S_1on, S_2off	$g_{p(n),i,k} = 0$	Short-circuited S_2	Bypassed	Zero
4*th*	$i_{p(n),k} < 0$	S_1off, S_2on	$g_{p(n),i,k} = 1$	Short-circuited S_2	Bypassed	Zero

5.4.2 Modification of the state observer under device faults

Based on the above analysis, it can be seen that the operation and fault mechanism under the four fault conditions is different from each other. When the open-circuit fault occurs in S_1 or S_2, the capacitor voltage in the faulty module increases and when the short-circuit fault occurs in S_1 or S_2, the capacitor voltage in the faulty module decreases to zero. According to this, the fault type (open-circuit fault or short-circuit fault) can be identified. To further identify the S_1 open-circuit fault and S_2 open-circuit fault, the modification strategy of the observer for the S_1 open-circuit fault is analyzed and to identify the S_1 short-circuit fault and S_2 short-circuit fault, the modification strategy of the observer for the S_2 short-circuit fault is analyzed.

1) Open Mode: Open-circuit fault in S_1

When the open-circuit fault happens in S_1, the capacitor is charged only under the condition of $i_{p(n),k} > 0$ and $g_{p(n),i,k} = 0$ appear at the same time instead of only $g_{p(n),i,k} = 0$. Therefore, the modified driving signal $g'_{p(n),i,k} = (i_{p(n),k} > 0 \&\& \ g_{p(n),i,k} = 0)$ is used in the observer model rather than the original driving signal.

2) Short Mode: Short-circuit fault in S_2

When the short-circuit fault happens in S_1, the module is bypassed and the capacitor voltage is stable to zero. Hence, $g''_{p(n),i,k} = 0$ is used in the observer model.

5.5 Simulation results

5.5.1 Fault detection method verification

For the detection algorithm, the threshold $k_{detection}$ is 0.003. The value was empirically established by analyzing several test conditions and taking into account a tradeoff between a fast detection and also robustness against false alarms.

Simulation results showing the algorithm behavior for normal operation, S_1 open-circuit fault, S_2 open-circuit fault, S_1 short-circuit fault, S_2 short-circuit fault, were obtained for two different power levels, which are 18 MW and 9 MW, respectively, in order to evaluate the technique under different operation condition.

A. Open-circuit fault in S_1

At $t = 0.3\ s$, an S_1 open-circuit fault in first module in the upper arm in phase a is introduced and the results are displayed in Fig. 5.3. The output current i_k in the three phases as well as their average values are shown in Fig. 5.3 (a) and Fig. 5.3 (b). The

output currents are balanced and their average values are equal to zero before 0.3 s. It can be seen that the waveforms of the output currents are also normal from 0.3 s to 0.312 s. That is due to the arm current in the upper arm in phase a is positive during 0.3 s and 0.312 s and according to Table 5.1 the faulty S_1 has no influence to the system during this period. After 0.312 s, when the arm current $i_{p(n),k} < 0$ and S_1 is on and S_2 is off, the faulty S_1 began to affect the performance of the system. However, from the output current in Fig. 5.3 (a), it is difficult to say the difference between the normal and the fault. But the difference of the normal diagnosis features and the faulty diagnosis features is obvious as shown in Fig. 5.3 (c). Thus, a fault is detected in MMC after the fault signature lasts for 100 sampling period.

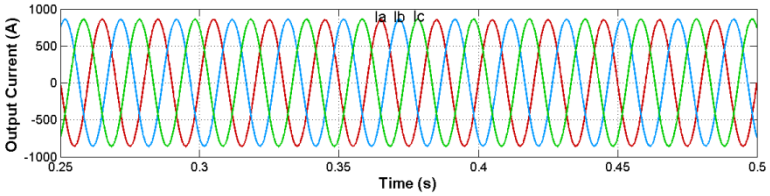

(a)

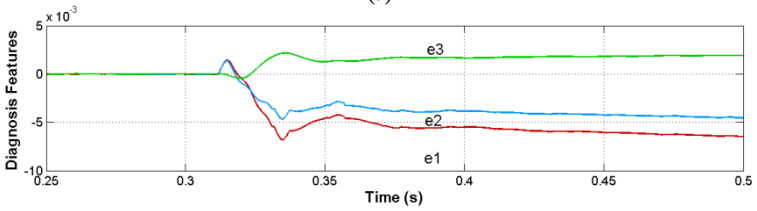

(b)

Fig. 5.3. S1 open-circuit fault detection under 18 MW (a) Output currents (b) diagnosis features.

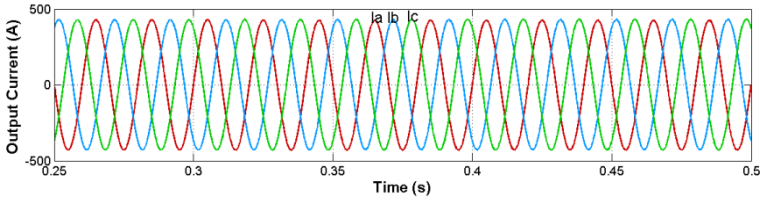

(a)

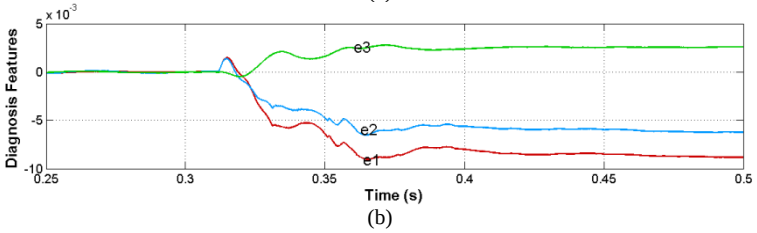

(b)

Fig. 5.4. S1 open-circuit fault detection under 9 MW (a) Output currents (b) diagnosis features.

In order to evaluate the algorithm performance for different operating conditions, the equivalent time-domain waveforms of the output currents and the three diagnostic variables for 9 MW power level are shown in Fig. 5.4. It can be seen that the chosen diagnosis features are unique fault signatures to detect fault in MMC.

It should be noticed that the chosen study case is almost the worst case which has the longest detection time because from 0.3 s to 0.312 s the arm current is positive in the upper arm in phase a and the faulty S_1 does not affect the system operation during this period. If the corresponding arm current is negative when the fault happens, the detection time will be much shorter than shown case.

B. Open-circuit fault in S_2

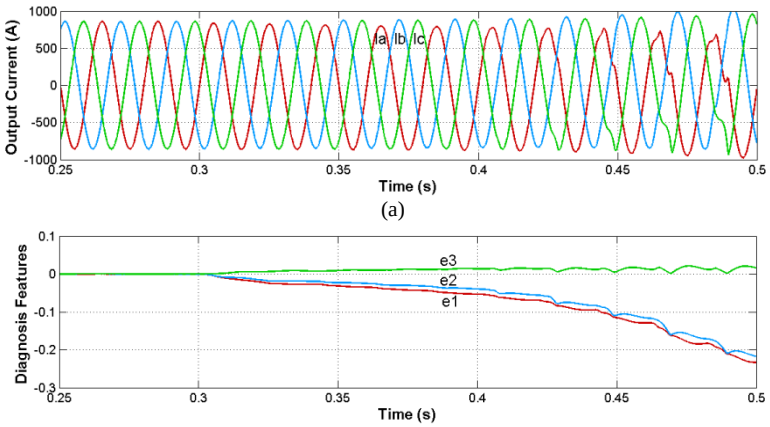

Fig. 5.5. S2 open-circuit fault detection under 18 MW (a) Output currents (b) diagnosis features.

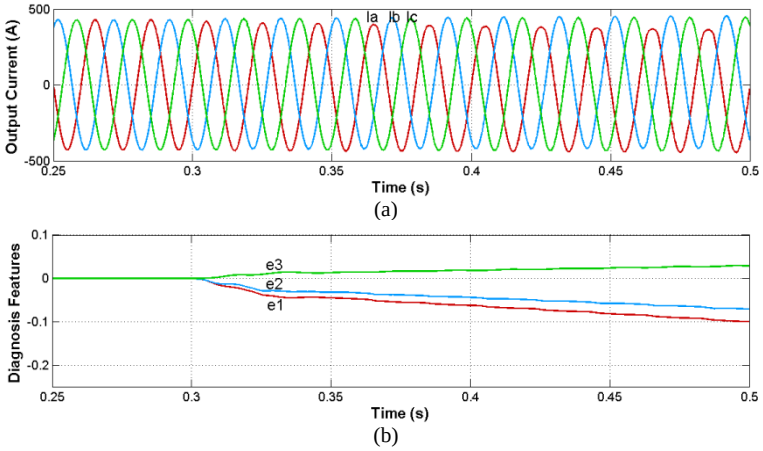

Fig. 5.6. S2 open-circuit fault detection under 9 MW (a) Output currents (b) diagnosis features.

Similarly, at $t = 0.3\ s$, an S_2 open-circuit fault in first module in the upper arm in phase a is introduced and the results are displayed in Fig. 5.5. It can be seen that the waveform of the output current in phase a changes after $0.3\ s$ and the errors among the three averaged output currents trend to be non-zero from which the fault can be detected.

When the open-circuit fault in S_2 happens at $0.3\ s$ under 9 MW transmission power, as shown in Fig. 5.6, the diagnosis variables are non-zero, as illustrated in the previous case. The fault can be detected.

C. Short-circuit fault in S_1

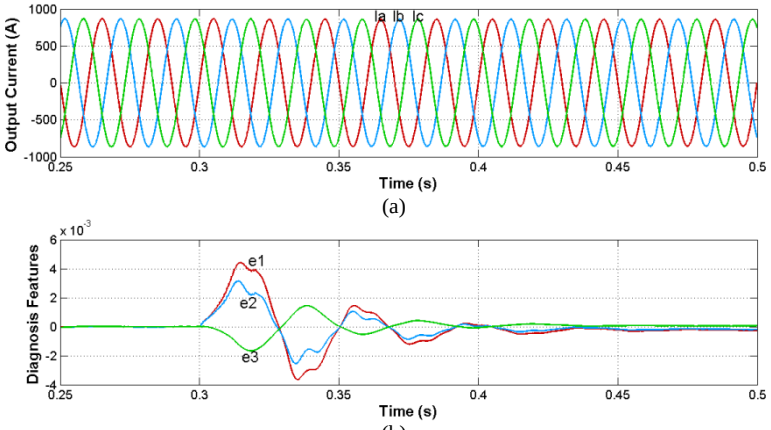

Fig. 5.7. S1 short-circuit fault detection under 18 MW (a) Output currents (b) diagnosis features.

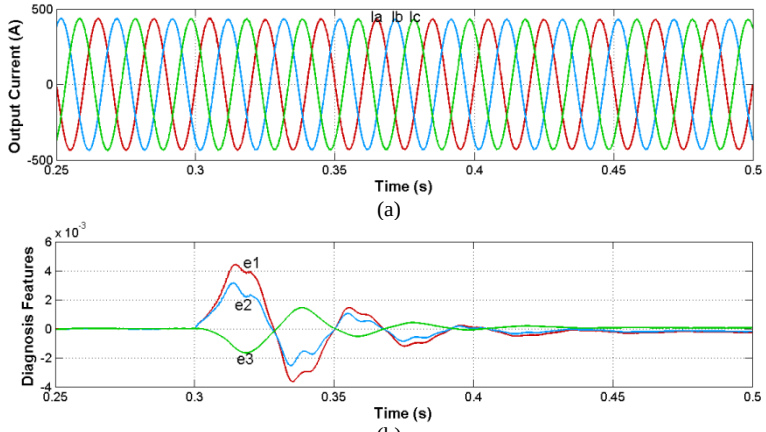

Fig. 5.8. S1 short-circuit fault detection under 9 MW (a) Output currents (b) diagnosis features.

The S_1 short-circuit fault under 18 MW and 9 MW are studied and the results are shown in Fig. 5.7 and Fig. 5.8, respectively. It can also be seen that the diagnosis variables $e1$, $e2$, and $e3$ are no longer zero after $t = 0.3\ s$. A fault in MMC can be detected.

D. Short-circuit fault in S_2

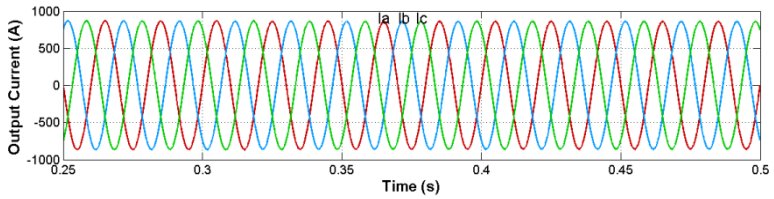

(a)

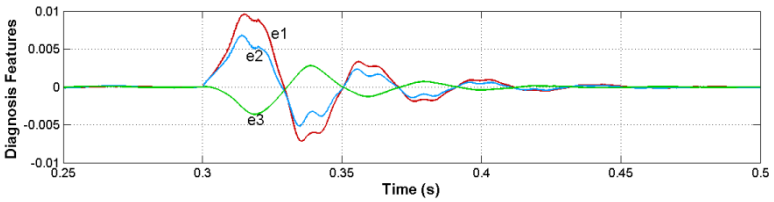

(b)

Fig. 5.9. S2 short-circuit fault detection under 18 MW (a) Output currents (b) diagnosis features.

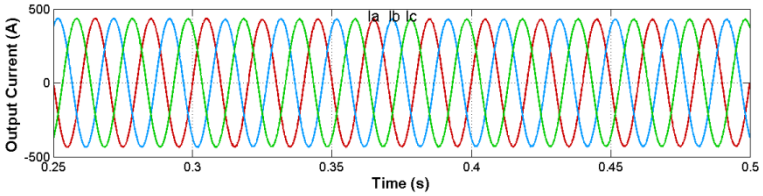

(a)

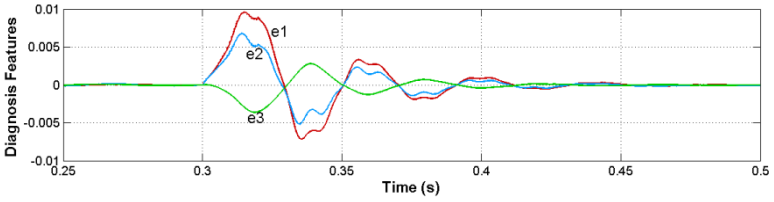

(b)

Fig. 5.10. S2 short-circuit fault detection under 9 MW (a) Output currents (b) diagnosis features.

The next analysis of the algorithm is the occurrence of S_1 short-circuit fault under 18 MW and 9 MW. Fig. 5.9 and Fig. 5.10 present the time-domain waveforms of the three phase currents and the three diagnosis variables.

Under normal operating conditions, all the three diagnosis variables are zero. Then, at $t = 0.3\,s$, a short-circuit fault in S_1 is introduced. Immediately after the fault occurrence, the diagnostic variables $e1$, $e2$, and $e3$ are no longer zero and it is able to detect a fault in phase a.

5.5.2 Faulty module localization method verification

For the faulty module localization algorithm, the threshold $k_{localization}$ is 50.

Faulty module localization results show the algorithm dynamic behavior under S_1 open-circuit fault, S_2 open-circuit fault, S_1 short-circuit fault, S_2 short-circuit fault as well as the multiple switch faults, in order to evaluate the effectiveness of the technique.

A. Open-circuit fault in T_1

Fig. 5.11 displays the performance of the MMC and the state observer under the open-circuit fault in T_1 in the first module of the upper arm in phase a.

To present the dynamic characteristic of the open-circuit fault, the fault is introduced at $t = 0.2\,s$. The output phase voltages v_a, v_b, v_c, load current i_a and arm current $i_{p,a}$, $i_{n,a}$ in phase a of the MMC are shown in Fig. 5.11 (a) and Fig. 5.11 (b), respectively. It can be seen that it is difficult to identify the affection of the open-circuit fault in T_1 to the system performance, compared with the waves under normal condition.

However, there is distortion in the capacitor voltages $v_{c,p,1,a} \sim v_{c,p,12,a}$ and $v_{c,n,1,a} \sim v_{c,n,12,a}$ caused by the open-circuit fault in T_1 as shown in Fig. 5.11 (c). The comparison of the measured capacitor voltages and the estimated values $\hat{v}_{c,p,1,a} \sim \hat{v}_{c,p,12,a}$ and $\hat{v}_{c,n,1,a} \sim \hat{v}_{c,n,12,a}$ in Fig. 5.11 (d) indicates that the estimated capacitor voltages in phase a obtained by employing the modified observer closely fit the measured capacitor voltages with maximum estimation error 0.75% as displayed in Fig. 5.11 (e), except that in the faulty module.

To make it clear, the measured capacitor voltage as well as the estimated capacitor voltage in the faulty module is shown in Fig. 5.11 (f), from which it can be seen that the faulty module can be detected and localized if the measured capacitor voltage is unequal to the estimated capacitor voltage. (In the figures, $Ev_{c,p(n),i,a}$ are the estimated capacitor voltages)

B. Open-circuit fault in T_2

The output performance of MMC under open-circuit fault in T_2 is displayed in Fig. 5.12.

The outputs are shown in Fig. 5.12 (a) and Fig. 5.12 (b). As that in the above case, the open-circuit fault in T_2 effects the output of the system slightly, while influences the capacitor voltages seriously as shown in Fig. 5.12 (c).

The estimated capacitor voltages $\hat{v}_{c,p,1,a}$~$\hat{v}_{c,p,12,a}$ and $\hat{v}_{c,n,1,a}$~$\hat{v}_{c,n,12,a}$ are displayed in Fig. 5.12 (d), from which we can see that, for those normal modules, the waves of the estimated capacitor voltages follow those of the measured, while their errors are calculated and displayed in Fig. 5.12 (e). However, for the faulty module, the estimated capacitor voltage cannot follow the measured capacitor voltage as shown in Fig. 5.12 (f), from which the faulty module can be localized.

C. Short-circuit fault in T_1

The result of the short circuit fault in T_1 is shown in Fig. 5.13. It can be seen that the faulty capacitor voltage $v_{c,p,1,a}$ of the first module in the upper arm in phase a decreases rapidly to zero after fault and then changing and discharging gradually with the change of arm current direction. For the normal module, the estimation error is within a certain range, while for the faulty modules, the estimation errors are larger than that of the normal module.

D. Short-circuit fault in T_2

The operation performance of MMC and observer under the short circuit fault in T_2 is shown in Fig. 5.14. The capacitor voltage $v_{c,p,1,a}$ of the faulty module decreases rapidly to zero after fault happens at $t = 0.2\ s$ since the capacitor in the faulty module is short-circuited by the short-circuited T_2 and the estimated voltage $\hat{v}_{c,p,1,a}$ cannot follow the faulty $v_{c,p,1,a}$ any more after the fault. Therefore, the faulty sub-module can be localized.

E. Multiple switch faults

In this case, open-circuit fault in T_1 in the second sub-module in phase a and open-circuit fault in T_2 in the first sub-module in phase a is introduced at $t = 0.2\ s$ and $t = 0.3\ s$, respectively. From Fig. 5.15 (f) and Fig. 5.15 (g), it can be seen that the multiple faults can be diagnosed as well.

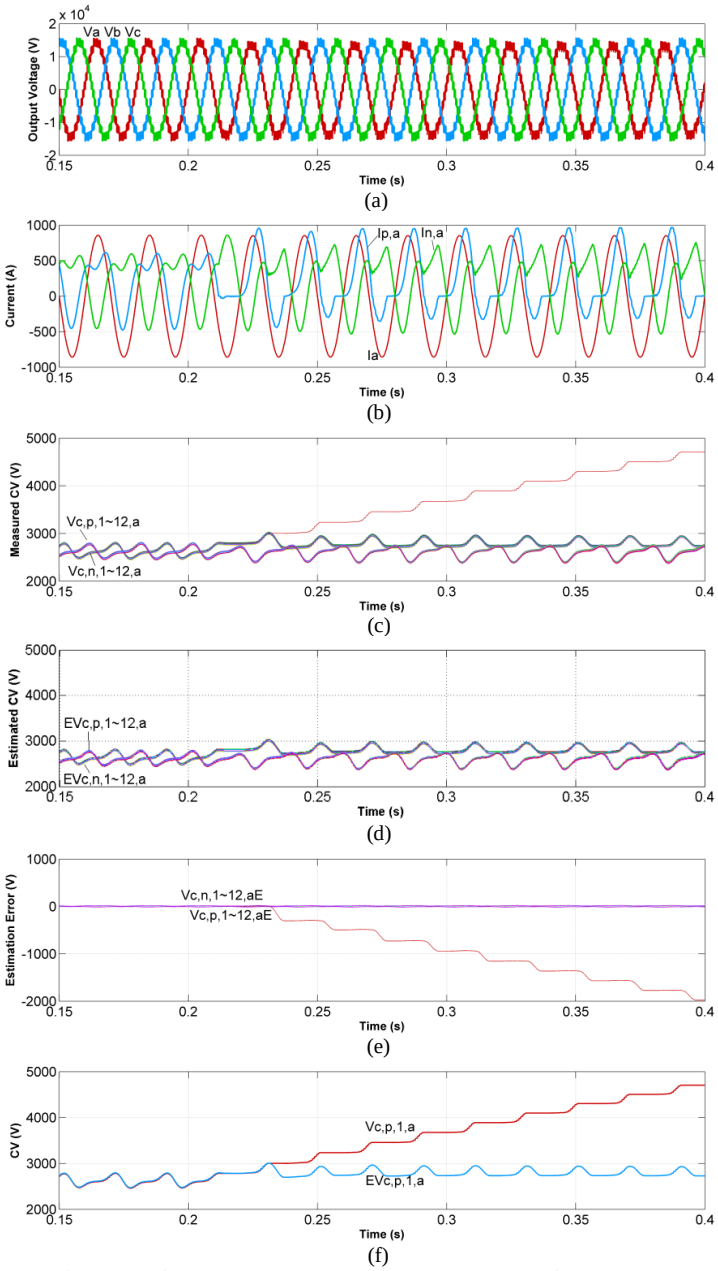

Fig. 5.11. Performance of MMC and state observer under open-circuit fault in T1 (a) Output phase voltage; (b) Load current and arm currents in phase A; (c) Measured capacitor voltage; (d) Estimated capacitor voltage; (e) Estimation error. (CV: Capacitor Voltage); (f) Measured and estimated capacitor voltages in the faulty module.

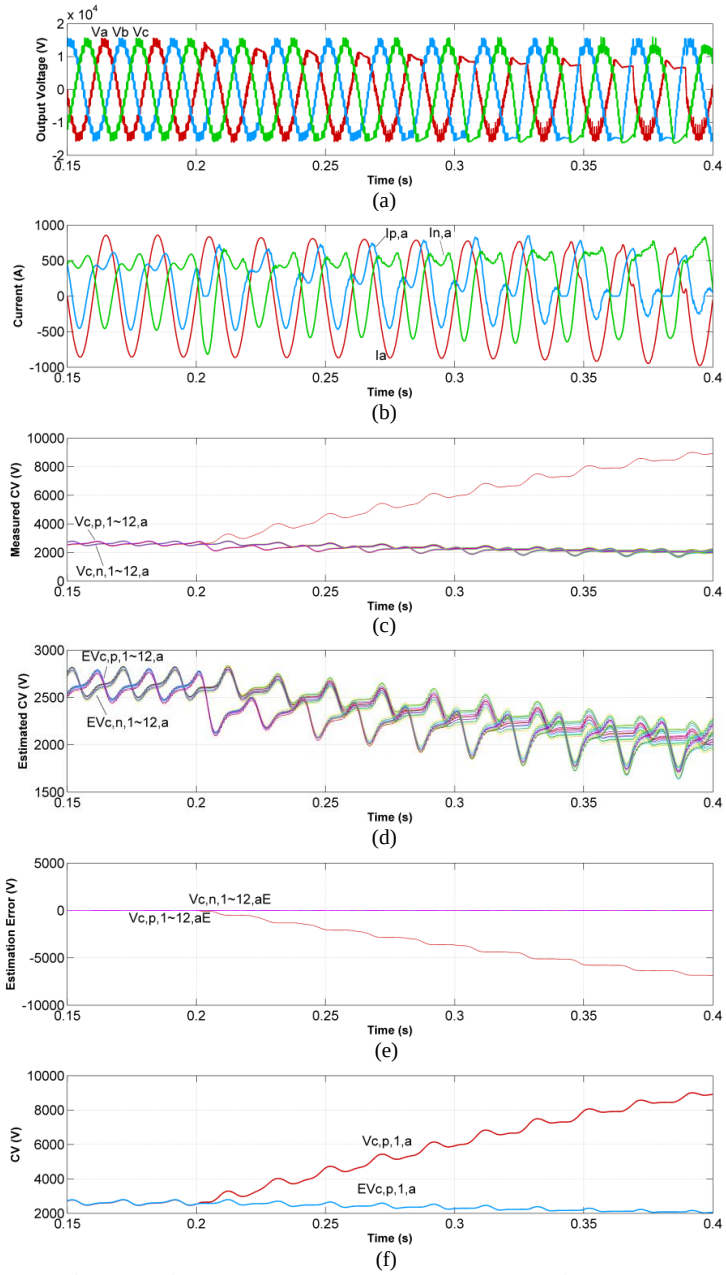

Fig. 5.12. Performance of MMC and state observer under open-circuit fault in T2 (a) Output phase voltage of MMC; (b) Load current and arm currents in phase A; (c) Measured capacitor voltage; (d) Estimated capacitor voltage; (e) Estimation error. (CV: Capacitor Voltage); (f) Measured and estimated capacitor voltages in the faulty module.

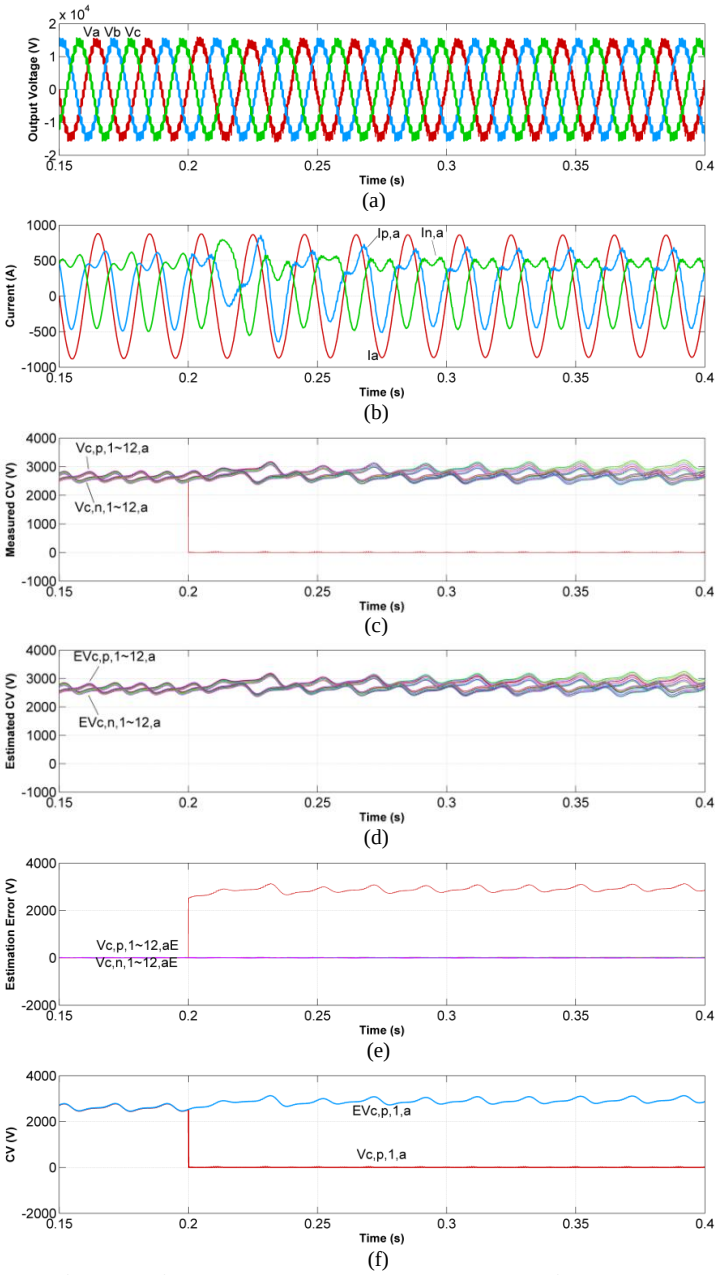

Fig. 5.13. Performance of MMC and state observer under short-circuit fault in T1 (a) Output phase voltage of MMC; (b) Load current and arm currents in phase A; (c) Measured capacitor voltage; (d) Estimated capacitor voltage; (e) Estimation error. (CV: Capacitor Voltage); (f) Measured and estimated capacitor voltages in the faulty module.

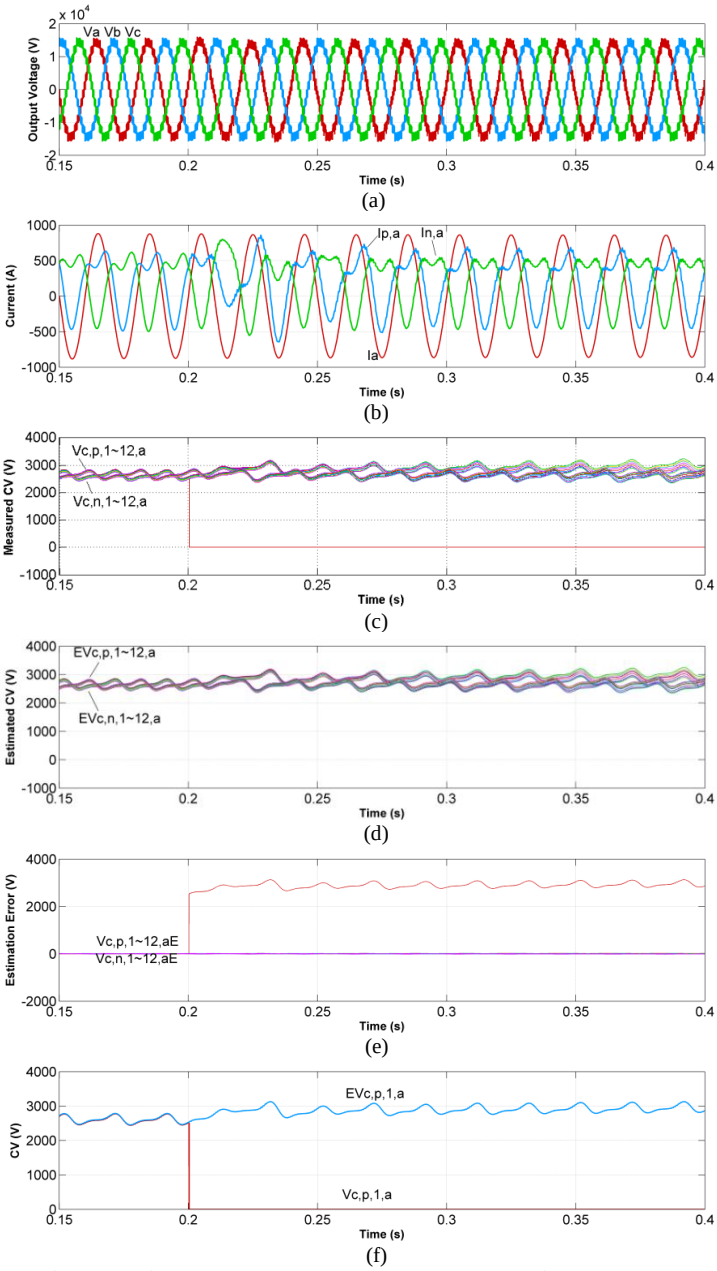

Fig. 5.14. Performance of MMC and state observer under short-circuit fault in T2 (a) Output phase voltage of MMC; (b) Load current and arm currents in phase A; (c) Measured capacitor voltage; (d) Estimated capacitor voltage; (e) Estimation error. (CV: Capacitor Voltage); (f) Measured and estimated capacitor voltages in the faulty module.

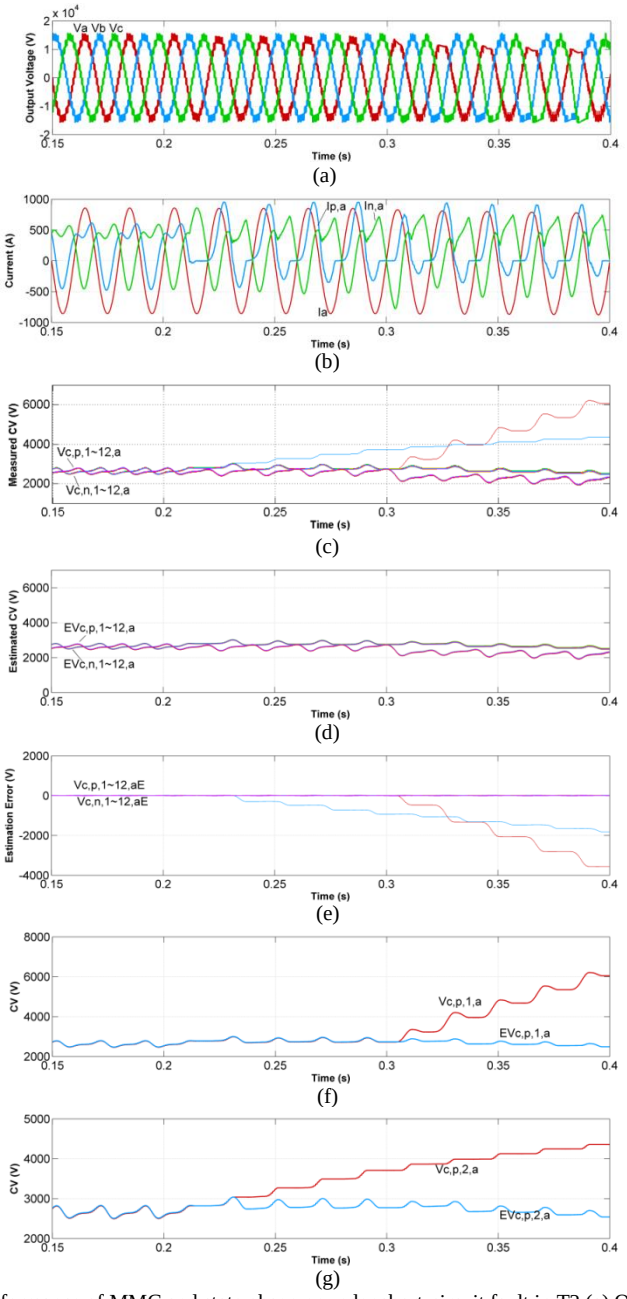

Fig. 5.15. Performance of MMC and state observer under short-circuit fault in T2 (a) Output phase voltage of MMC; (b) Load current and arm currents in phase A; (c) Measured capacitor voltage; (d) Estimated capacitor voltage; (e) Estimation error. (CV: Capacitor Voltage); (f) Measured and estimated capacitor voltages in the faulty module (g) Measured and estimated capacitor voltages in another faulty module.

5.5.3 Faulty device identification method verification

For the faulty device identification algorithm, the threshold $k_{identification\_open}$ is 50 and $k_{identification\_short}$ is 1. Faulty device identification results show the algorithm dynamic behavior under S_1 open-circuit fault, S_2 open-circuit fault, S_1 short-circuit fault, S_2 short-circuit fault, in order to evaluate the effectiveness of the technique.

A. Open-circuit fault in S_1 or S_2

At $t = 0.3\ s$, an S_1 open-circuit fault in the first module in the upper arm in phase a is introduced and the results are displayed in Fig. 5.16 (a). Once the faulty module is localized, the gating signal for the faulty module is immediately adjusted to Mode 1 in order to estimate the faulty capacitor voltage. By comparing the measured faulty capacitor voltage with the corresponding faulty estimated capacitor voltages, the faulty device can be identified if they are consistent.

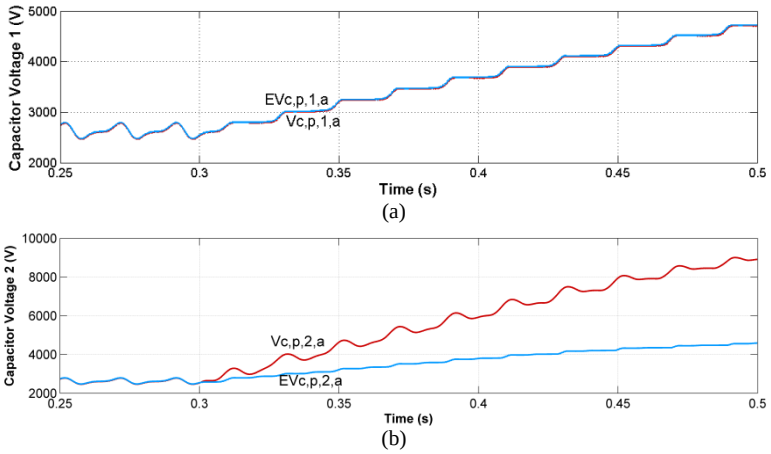

Fig. 5.16. Open-circuit fault in S1 or S2 (a) capacitor voltages in SM1 (b) capacitor voltages in SM2.

Moreover, at $t = 0.3\ s$, an S_2 open-circuit fault in the second module in the upper arm in phase a is introduced, but the gating signal for the faulty module is still adjusted to mode 1. As shown in Fig. 5.16 (b), the error between the measured capacitor voltage and the estimated capacitor voltage is larger than $k_{localization}$ for 100 sampling time. Therefore, by exclusion, the algorithm localizes S_2 in the faulty module to be the faulty device.

B. Short-circuit fault in S_1 or S_2

At $t = 0.3\ s$, a short-circuit fault in S_2 is introduced to the first module in the upper arm in phase a. Once the faulty module is localized, the gating signal for the faulty

module is immediately adjusted to Mode 2 in order to estimate the faulty capacitor voltage. By observing the difference between the measured faulty capacitor voltage and the corresponding estimated faulty capacitor voltages, the faulty device can be identified if the difference is smaller than $k_{localization}$ within 100 sampling time, as shown in Fig. 5.17 (a).

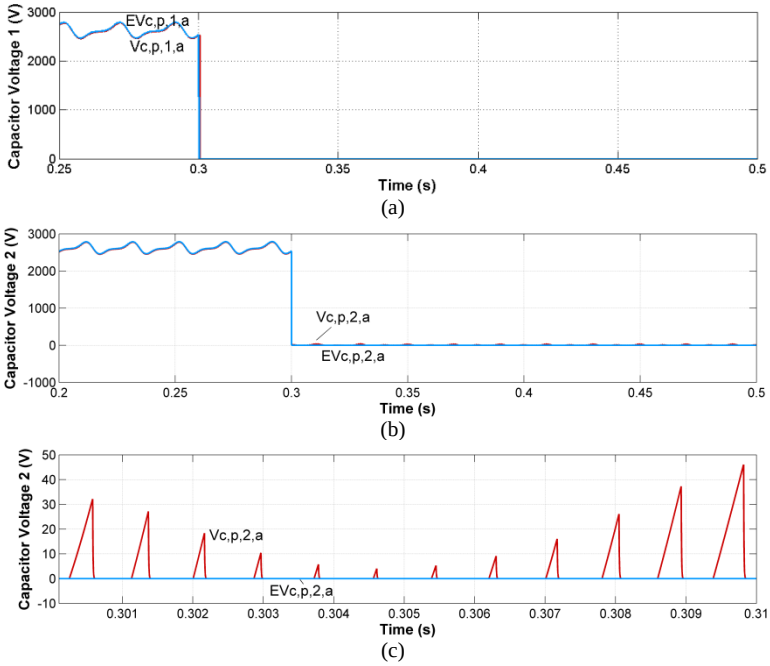

Fig. 5.17. Short-circuit fault in S1 or S2 (a) capacitor voltages in SM1 (b) capacitor voltages in SM2 (c) zoom in waveforms of (b).

At $t = 0.3\ s$, an S_1 short-circuit fault in the second module in the upper arm in phase a is introduced, but the gating signal for the faulty module is still adjusted to mode 2. As shown in Fig. 5.17 (b), the error between the measured capacitor voltage and the estimated capacitor voltage is larger than $k_{localization}$ for 100 sampling time. Therefore, by exclusion, the algorithm localizes S_1 in the faulty module to be the faulty device. The zoom in waveform is given in Fig. 5.17 (c).

5.6 Summary

An algorithm for real-time diagnosis of power switches open-circuit faults, short-circuit faults as well as the multiple faults in MMC has been proposed in this chapter. It consists of three stages, fault detect, faulty modules localization and faulty device identification. Pointing to different applications and different requirements, the three stages can be used separately.

The technique just uses variables that are already available from the control system. This means that it avoids the use of extra sensors or electric devices and avoids extra complexity and costs of the system.

The obtained results allow concluding that, in opposition to other existing methods, the algorithm behavior depends neither on the transmission power level, nor on its load level. Accordingly, universal thresholds can be defined independently of these issues and this idea will simplify the method implementation and application to other cases.

Finally, compared with the existing methods, the developed diagnostic algorithm is relatively simple since it just requires a few and basic mathematical operations. This makes it not computationally demanding, and therefore, it can easily be integrated into the main control system without great effort.

6 Conclusion and Future Work

The intent of this chapter is to summarize the work which has been done throughout this Ph.D. project, and to emphasize the main contributions of this project – *reliability improvement of MMC applied to offshore wind power generation system including lifetime evaluation of MMC and switching device fault diagnosis considering various mission profiles*. Then, this chapter ends with an outlook of this topic in order to enrich the future research outcome.

6.1 Conclusion

The main topics of this project are: *a)* how the reliability of MMC is affected by normal and abnormal operation and *b)* how to improve the reliability of the MMC. The first topic is described in *Chapter 2* and *Chapter 3* by studying the thermal distribution and lifetime estimation of the MMC considering different mission profiles. The second topic is conducted by diagnosing and localizing the faulty switching devices in the MMC in *Chapter 5* based on the observer proposed and designed in *Chapter 4*.

6.1.1 Lifetime estimation of MMC

A lifetime prediction method of the MMC based on the fatigue in the power module is presented based on the operating conditions of the MMC. It is concluded that the lower IGBT in the module bears the most serious stress and consequently the lowest lifetime and it is also illustrated that not only the maximum temperature is of significant importance for the lifetime consumption, but also the temperature cycles caused by the fluctuation of the wind speed will have strong impacts to the lifetime of power semiconductors.

6.1.2 Thermal distribution of MMC under grid faults

An investigation on the influence of various grid voltage dips to the operating and loading behaviors of the MMC is conducted. It is noticed that the operation conditions of the MMC are non-symmetrical among the three phases when unbalanced grid faults are present in the system.

The different grid fault types and severity values of voltage dips will aggravate the unbalanced loading of the devices. Some power devices under the LVRT operation may have even higher junction temperature than the normal full load operation condition. This overloading should be taken into account when choosing the power devices and designing the heat sink system for the wind power converter.

6.1.3 State observer design of MMC

To estimate the capacitor voltages in the MMC, a state observer of MMC is established and verified under not only normal operation condition, but also various condition disturbances, which illustrates the effectiveness and the robustness of the proposed state observer.

6.1.4 Fault diagnosis of MMC

A fault diagnosis method is proposed to detect the fault, localize the faulty modules and identify the faulty devices. After a series of verification it can be seen that the proposed fault diagnosis method is effective to not only open-circuit faults, short-circuit faults as well as the multiple device faults in MMC. The behavior of the fault diagnosis method depends neither on the transmission power level, nor on its load level. Moreover, it avoids the extra sensors or electric devices and not computationally demanding.

6.2 Main contributions

The significance and main contributions of this project from the author's point of view can be summarized as follows:

- *Lifetime estimation of devices in MMC*
- *Investigations of the thermal loading of MMC under grid faults*
- *Design of state observer of MMC*
- *Advanced fault diagnosis method for MMC*

6.3 Proposals for future research topics

Although some aspects have been documented in this thesis for reliability of the MMC system, there are still many possibilities for technology improvement. Some issues of high interest for future investigations are listed below:

1) The lifetime estimation model used in this project is a common used approach. However, it is more complete if the comparison can be done with other lifetime models supplied by other companies. Moreover, the power loss calculation is only focused on those generated by IGBTs and Diodes. As a whole system, the loss produced by inductors and capacitors might also be considered in such cases. Hence, this would be an important topic to investigate exactly the power loss, efficiency, thermal and lifetime of MMC. Additionally, the power loss and thermal analysis under other mission profiles, such as DC fault, have not been clarified yet and would be an interesting scope for the future.

2) The power loss distribution affects the thermal behavior and thus the lifetime of the MMC. The development of potential solutions, such as the advanced control strategies as well as the new modulation methods for the temperature balance among the devices, could also be an interesting point to study further.

3) It should be pointed out that most existing studies with the area of fault diagnosis and fault-tolerant control of MMC-HVDC are done in terms of switching device faults in MMC, DC faults as well as AC grid faults, while the fault detection, fault location and fault handling on the other parts such as diode faults, capacitor faults or aging, driving unit, control unit and so on are rather rare. They are also of importance and should be achieved due to largely applied in MMC-HVDC system.

4) The model estimation of MMC considering both system reliability and efficiency is also worth investigating more as well as doing experimental validation of all the issues proposed in the thesis.

Besides the above topics, the development and implementation of the technical standards of the MMC are far from finalization. Moreover, applying the advanced fault diagnosis method on other topologies than the used MMC might be another interesting study.

Reference

[1] M. Renvall, "Nine tidal and ocean stream power startup companies from Scandinavia," July 30 2010.
Online: *http://www.nordicgreen.net/startups/article/tidal-and-ocean-stream-power-concepts-scandinavia*

[2] "Key world energy statistic," International energy agency (IEA), 2012.

[3] International energy agency-Ocean energy systems (IEA-OES) Annual Report, 2009.

[4] IEA 2013, Medium-term renewable energy market report 2013, OECD/IEA, Paris.

[5] http://www.tennet.eu/de/en/grid-projects/offshore-projects/borwin1.html

[6] S. Teeuwsen, "Modeling the trans bay cable project as voltage-sourced converter with modular multilevel converter design," *in Proc. IEEE Power and Energy Society General Meeting*, San Diego, US, pp. 1-8, Jul. 2011.

[7] W. D. Qiao, Y. K. Mao, "Overview of Shanghai flexible HVDC transmission demonstration project," *East China Electric Power*, vol. 39, no. 7, pp. 1137-1140 , Jul. 2011.

[8] http://thesiemensgraduateprogram.tumblr.com/post/57698401454/inelfe-the-hvdc-plus-interconnection-between

[9] V. Hussennether, J. Rittiger, A. Barth, D. Worthington, G. Dell'anna, M. Rapetti, B. Huhnerbein, M. Siebert, "Projects BorWin2 and HelWin1-large scale multilevel voltage sourced converter technology for bundling of offshore wind power," presented at the Cigre, ser. B4-306, Paris, France, 2012.

[10] http://www.tennet.eu/de/netz-und-projekte/offshore-projekte/sylwin1.html

[11] M. Chen, H. Rao, L. C. Li, J. C. Guo, X. L. Li, S. K. Xu, "Analysis on the main wiring of Nan'ao VSC-HVDC transmission system," *Southern Power System Technology*, vol. 6, no. 6, pp. 1-5, 2012.

[12] Q. Gao, Y. Lin, L. C. Huang, W. Luo, "An overview of Zhoushan VSC-HVDC transmission project," *Power System and Clean Energy*, vol. 31, no. 2, pp. 33-38, 2015.

[13] http://new.abb.com/systems/hvdc/references/dolwin1

[14] http://new.abb.com/systems/hvdc/references/dolwin2

[15] http://www.tennet.eu/de/netz-und-projekte/offshore-projekte/helwin2.html

[16] http://www.tennet.eu/de/netz-und-projekte/offshore-projekte/dolwin3.html

[17] I. A. Gowaid, G. P. Adam, A. S. Ahmed, D. Holliday, B. W. Williams, "Analysis and design of a modular multilevel converter with trapezoidal modulation for medium and high voltage DC-DC transformers," *IEEE Trans. Power Electron.*, vol. 30, no. 10, pp. 5439-5457, 2015.

[18] F. Gao, D. C. Niu, H. Tian, C. J. Jia, N. Li, Y. Zhao, "Control of parallel-connected modular multilevel converters," *IEEE Trans. Power Electron.*, vol. 30, no. 1, pp. 372-386, 2015.

[19] G. Adam, I. Davidson, "Robust and generic control of full-bridge modular multilevel converter high-voltage DC transmission systems," *IEEE Trans. Power Electron.*, 2015, to be published.

[20] G. R. Liu, Z. Xu, Y. L. Xue, G. Tang, "Optimized control strategy based on dynamic redundancy for the modular multilevel converter," *IEEE Trans. Power Electron.*, vol. 30, no. 1, pp. 339-348, 2015.

[21] K. J. Ou, H. Rao, Z. X. Cai, H. P. Guo, "MMC-HVDC simulation and testing based on real-time digital simulator and physical control system," *IEEE Journal of Emerging and Selected Topics in Power Electronics*, vol. 2, no. 4, pp. 1109-1116, 2014.

[22] Y. L. Xue, Z. Xu, G. Tang, "Self-start control with grouping sequentially precharge for the C-MMC-based HVDC system," *IEEE Trans. Power Del.*, vol. 29, no. 1, pp. 187-198, 2014.

[23] F. Yu, W. X. Lin, X. T. Wang, D. Xie, "Fast voltage-balancing control and fast numerical simulation model for the modular multilevel converter," *IEEE Trans. Power Del.*, vol. 30, no. 1, pp. 220-228, 2015.

[24] C. Wang, B. T. Ooi, "Incorporation deadbeat and low-frequency harmonic elimination in modular multilevel converters," *IET Generation, Transmission & Distribution*, vol. 9, no. 4, pp. 369-378, 2015.

[25] J. P. Zhang, C. Y. Zhao, "The research of SM topology with DC fault tolerance in MMC-HVDC," *IEEE Trans. Power Del.*, vol. 30, no. 3, pp. 1561-1568, 2015.

[26] R. Zeng, L, Xu, L. Z. Yao, D. J. Morrow, "Precharging and DC fault ride-through of hybrid MMC-based HVDC systems," *IEEE Trans. Power Del.*, vol. 30, no. 3, pp. 1298-1306, 2015.

[27] R. Li, J. E. Fletcher, L. Xu, D. Holliday, B. W. Williams, "A hybrid modular multilevel converter with novel three-level cells for DC fault blocking capability," *IEEE Trans. Power Del.*, vol. 30, no. 4, pp. 2017-2026, 2015.

[28] G. J. Kish, M. Ranjram, P. W. Lehn, "A modular multilevel DC/DC converter with fault blocking capability for HVDC interconnects," *IEEE Trans. Power Electron.*, vol. 30, no. 1, pp. 148-162, 2015.

[29] R. Li, G. P. Adam, D. Holliday, J. E. Fletcher, "Hybrid cascaded modular multilevel converter with DC fault ride-through capability for the HVDC transmission system," *IEEE Trans. Power Del.*, vol. 30, no. 4, pp. 1853-1862, 2015.

[30] A. A. Elserougi, A. M. Massoud, S. Ahmed, "A switched-capacitor sub-module for modular multilevel HVDC converters with DC-fault blocking capability and a reduced number of sensors," *IEEE Trans. Power Del.*, vol. 31, no. 1, pp. 313-322, 2016.

[31] C. Chen, G. P. Adam, S. Finney, J. Fletcher, B. Williams, "H-bridge modular multilevel converter: control strategy for improved DC fault ride-through capability without converter blocking," *IET Power Electronics*, vol. 8, no. 10, pp. 1996-2008, 2015.

[32] I. A. Gowaid, G. P. Adam, A. M. Massoud, S. Ahmed, D. Holliday, B. W. Williams, "Quasi two-level operation of modular multilevel converter for use in a high-power DC transformer with DC fault isolation capability," *IEEE Trans. Power Electron.*, vol. 30, no. 1, pp. 108-123, 2015.

[33] X. J. Shi, Z. Q. Wang, B. Liu, Y. Q. Liu, L. M. Tolbert, F. Wang, "Characteristic investigation and control of a modular multilevel converter-based HVDC system under single-line-to-ground fault conditions," *IEEE Trans. Power Electron.*, vol. 30, no. 1, pp. 408-421, 2015.

[34] Q. R. Tu, Z. Xu, Y. Chang, L. Guan, "Suppressing DC voltage ripples of MMC-HVDC under unbalanced grid conditions," *IEEE Trans. Power Del.*, vol. 27, no. 3, pp. 1332-1338, 2012.

[35] T. Li, C. Zhao, "Recovering the modular multilevel converter from a cleared or isolated fault," *IET Generation, Transmission & Distribution*, vol. 9, no. 6, pp. 550-559, 2015.

[36] L. A. Gregoire, H. F. Blanchette, W. Li, A. Antonopoulos, L. Angquist, K. Al-Haddad, "Modular multilevel converters overvoltage diagnosis and remedial strategy during blocking sequences," *IEEE Trans. Power Electron.*, vol. 30, no. 5, 2015.

[37] R. Li, L. Xu, D. Holliday, F. Page, S. J. Finney, B. W. Williams, "Continuous operation of radial multi-terminal HVDC systems under DC fault," *IEEE Trans. Power Del.*, vol. 31, no. 1, pp. 351-361, 2016.

[38] J. Mei, Y. Ji, J. Tian, C. Huang, X. Du, Y. Xie, Q. Hu, T. Ma, "Balancing control schemes for modular multilevel converters using virtual loop mapping with fault-tolerance capabilities," *IEEE Trans. Industrial Electron.*, 2015, to be published.

[39] G. T. Son, H. J. Lee, T. S. Nam, Y. H. Chung, U. H. Lee, S. T. Baek, K. Hur, J. W. Part, "Design and control of a modular multilevel HVDC converter with redundant power modules for noninterruptible energy transfer," *IEEE Trans. Power Del.*, vol. 27, no. 3, pp. 1611-1619, 2012.

[40] J. Xu, P. Zhao, C. Zhao, "Reliability analysis and redundancy configuration of MMC with hybrid sub-module topologies," *IEEE Trans Power Electron.*, vol. 31, no. 4, pp. 2720-2729, 2016.

[41] G. Konstantinou, J. Pou, S. Ceballos, V. G. Agelidis, "Active redundant submodule configuration in modular multilevel converters," *IEEE Trans. Power Del.*, vol. 28, no. 4, pp. 2333-2341, 2013.

[42] B. B. Li, Y. Zhang, R. F. Yang, R. Xu, "Seamless transition control for modular multilevel converters when inserting a cold-reserve redundant submodule," *IEEE Trans. Power Del.*, vol. 30, no. 8, pp. 4052-405, 2015.

[43] Q. Yang, J. Qin, M. Saeedifard, "A post-fault strategy to control the modular multilevel converter under submodule failure," *IEEE Trans. Power Del.*, 2015, to be published.

[44] P. F. Hu, D. Z. Jiang, Y. B. Zhou, Y. Q. Liang, J. Guo, Z. Y. Lin,, "Energy-balancing control strategy for modular multilevel converters under submodule fault conditions," *IEEE Trans. Power Electron.*, vol. 29, no. 9, pp. 5021-5030, 2014.

[45] ZVEL, Handbook for robustness validation of automotive electrical/electronic modules, Jun. 2008.

[46] J. Due, S. Munk-Nielsen, R. Nielsen, "Lifetime investigation of high power IGBT modules," *in Proc. of EPE*, Birmingham, pp. 1-8, Sept. 2011.

[47] K. Ma, M. Liserre, F. Blaabjerg, T. Kerekes, "Thermal loading and lifetime estimation for power device considering mission profile in wind power converter," *IEEE Trans. Power Electron.*, vol. 20, no. 2, pp. 590-602, 2015.

[48] H. Huang, P. A. Mawby, "A lifetime estimation technique for voltage source inverters," *IEEE Trans. Power Electron.*, vol. 28, no. 8, pp. 4113-4119, Dec. 2012.

[49] A. Isidori, F. M. Rossi, F. Blaabjerg, K. Ma, "Thermal loading and reliability of 10 MW multilevel wind power converter at different wind roughness classes," *IEEE Trans. Ind. Appl.*, vol. 50, no. 1, pp. 484-494, Jun. 2013.

[50] Y. M. T. Bina, B. Eskandari, "Efficiency of three-level neutral-point clamped converters: analysis and experimental validation of power losses, thermal modelling and lifetime prediction," *IEEE Power Electron. Lett.*, vol. 7, no. 1, pp. 204-214, Jan. 2014.

[51] C. Busca, R. Teodorescu, F. Blaabjerg, S. Munk-Nielsen, L. Helle, T. Abeyasekera, P. Rodriguez, "An overview of the reliability prediction related aspects of high power IGBTs in wind power applications," *Microelectronics Reliability*, Vol. 51, no. 9-11, September-November 2011, pp. 1903-1907.

[52] A. Wintrich, U. Nicolai, T. Reimann, "Semikron Application Manual," pp. 128, 2011.

[53] I.F. Kovacevic, U. Drofenik, J.W. Kolar, "New physical model for lifetime estimation of power modules," *in Proc. IPEC'10*, pp. 2106-2114, 2010.

[54] ABB Application Note, Load-cycling capability of HiPak IGBT modules, 2012.

[55] R. Marquardt, "Modular multilevel converter topologies with DC-short circuit current limitation," *in Proc. International Conference on Power Electronics (ECCE)*, Korea, Asia, pp. 1425-1431, May 30- June 3, 2011.

[56] M. Hagiwara, H. Akagi, "PWM control and experiment of modular multilevel converters," *in Proc. Power Electronics Specialists Conf.*, Rhodes, Greece, pp. 154-161, Jun. 2008.

[57] B. Tuchband, N. Vichare and M. Pecht, "A method for implementing prognostics to legacy systems," *in Proc. IMAPS Military, Aerospace, Space and Homeland Security: Packaging Issues and Applications*, 2006.

[58] E. Wolfgang, "Examples for failures in power electronics systems," *presented at ECPE Tutorial on Reliability of Power Electronic Systems*, Nuremberg, Germany, Apr. 2007.

[59] S. Yang, A. T. Bryant, P. A. Mawby, D. Xiang, L. Ran, and P. Tavner, "An industry-based survey of reliability in power electronic converters," *IEEE Trans. Ind. Appl.*, vol. 47, no. 3, pp. 1441- 1451, May/Jun.,2011.

[60] E. Wolfgang, L. Amigues, N. Seliger and G. Lugert, "Building-in Reliability into Power Electronics Systems". *The World of Electronic Packaging and System Integration*, 2005, pp. 246-252.

[61] R. Teodorescu, F. Blaabjerg, J. K. Pedersen, E. Cengelci, P. N. Enjeti, "Multilevel inverter by cascading industrial VSI," *IEEE Trans. Ind. Electron.*, vol. 49, no. 4, pp. 832-838, Aug. 2002.

[62] H. Liu, P. C. Loh, F. Blaabjerg, "Review of fault diagnosis and fault-tolerant control of modular multilevel converter for HVDC," *in Proc. of IEEE 39th IECON Europe Conference*, Vienna, Austria, pp. 1242-1247, Sept. 2013.

[63] P. Lezana, R. Aguilera, J. Rodríguez, "Fault detection on multicell converter based on output voltage frequency analysis," *IEEE Trans. Ind. Electron.*, vol. 56, no. 6, pp. 2275-2283, Jun. 2009.

[64] A. Yazdani, H. Sepahvand, M. L. Crow, M. Ferdowsi, "Fault detection and mitigation in multilevel STATCOMs," *IEEE Trans. Ind. Electron.*, vol. 58, no. 4, pp. 1307-1315, Apr. 2011.

[65] S. Shao, P. W. Wheeler, J. C. Clare, A. J. Watson, "Fault detection for modular multilevel converters based on sliding mode observer," *IEEE Trans. Power Electron.*, vol. 28,no. 11, pp. 4867-4872, Nov. 2013.

[66] F. J. Deng, Z. Chen, M. R. Khan, R. W. Zhu, "Fault detection and localization of modular multilevel converter," *IEEE Trans. Power Electron.*, vol.50, no. 5, May 2015.

[67] S. Khomfoi, L. Tolbert, "Fault diagnosis and reconfiguration for multilevel inverter drive using AI-based techniques," *IEEE Trans. Ind. Electron.*, vol. 54, no. 6, pp. 2954-2968, Dec. 2007.

[68] S. Khomfoi, L. M. Tolbert, "Fault diagnosis system for a multilevel inverter using a neural network," *IEEE Trans. Industry Electron.*, vol. 22, no. 3, pp. 1062-1069, May 2007.

[69] W. Jiang, C. Wang, M. Wang, "Fault detection and Remedy of Multilevel Inverter based on BP Neural Network," *in Proc. Asia-Pacific Power and Energy Engineering Conference (APPEEC)*, Shanghai, China, pp. 1-4, Mar. 2012.

[70] S. Sedghi, A. Dastfan, A. Ahmadyfard, "Fault detection of a seven level modular multilevel inverter via voltage histogram and neural network," *in Proc. Energy Conversion Congress and Exposition (ECCE)*, Shilla Jeju, Korea, pp. 1005-1012, May 30-June 3, 2011.

[71] Y. Liu, Z. Chen, "A flexible power control method of VSC-HVDC link for the enhancement of effective short-circuit ratio in a hybrid multi-infeed HVDC system," *IEEE Trans. Power System*, vol. 28, no. 2, pp. 1568-1581, 2013.

[72] K. Ma, F. Blaabjerg, "Modulation methods for neutral-point-clamped wind power converter achieving loss and thermal redistribution under low-voltage ride-through," *IEEE Trans. Ind. Electron.*, vol. 61, no. 2, pp. 835-845, 2014.

[73] G. Bergna, J. A. Suul, E. Bernet, P. Egrott, P. Lefranc, J. C. Vannier, M. Molinas, "Mitigating DC-Side power oscillations and negative sequence load currents in modular multilevel converters under unbalanced faults- first approach using resonant PI," *in Proc. Annual Conference on IEEE Industrial Electronics Society (IECON)*, pp. 537-542, 2012.

[74] D. Schmitt, Y. Wang, T. Weyh, R. Marquardt, "DC-Side fault current management in extended multiterminal-HVDC-grids," *in Proc. International Multi-Conference on Systems, Signals and Devices (SSD)*, pp. 1-5, 2012.

[75] 75S. Y. Yang, A. Bryant, P. Mawby, D. W. Xiang, L. Ran, P. Tavner, "An industry-based survey of reliability in power electronic converters," *IEEE Trans. Ind. Applic.*, vol. 47, no. 3, pp. 1441-1451, 2011.

[76] M. Zhang, L. Huang, W. X. Yao, Z. Y. Lu, "Circulating harmonic current elimination of a CPS-PWM-Based modular multilevel converter with a plug-in repetitive controller," *IEEE Trans. on Power Electron.*, vol. 29, no. 4, pp. 2083-2097, Apr. 2014.

[77] K. Ma, M. Liserre, F. Blaabjerg, "Operating and loading conditions of a three-level neutral-point-clamped wind power converter under various grid faults," *IEEE Trans. Ind. Appl.*, vol. 50, no. 1, pp. 520-530, Jun. 2014.

[78] M. Matsuishi, T. Endo, "Fatigue of metals subjected to varying stress," *Jap Soc. Mech. Eng.*, Fukouka, Japan, Mar. 1968.

[79] S. S. Manson, *Thermal Stress and Low-Cycle Fatigue*. New York: Mc-Graw-Hill, 1966.

[80] K. C. Norris, A. H. Landzberg, "Reliability of controlled collapse interconnections," *IBM Journal of Research and Development*, vol. 13, no. 3, pp. 266-271, May 1969.

[81] R. Bayerer,T. Hermann, T. Licht, J. Lutz, M. Feller, "Model for power cycling lifetime of IGBT modules-various factors influencing lifetime", *in Proc. of CIPS'2008*, Nuremberg, Germany, March 11-13, 2008.

[82] M. A. Miner, "Cumulative damage in fatigue," *Journal of Applied Mechanics*, no. 12, A159-A164, 1945.

[83] M. Altin, O. Goksu, R. Teodorescu, P. Rodriguez, B. Bak-Jensen, L. Helle, "Overview of recent grid codes for wind power integration," in *Proc. OPTIM*, pp. 1152–1160, 2010.

[84] Grid Code. High and Extra High Voltage, E.ON Netz GmbH, Bayreuth, Germany, Apr. 2006.

[85] K. Ma, F. Blaabjerg, M. Liserre, "Thermal analysis of multilevel grid side converters for 10MWwind turbines under low voltage ride through," *IEEE Trans. Ind. Appl.*, vol. 49, no. 2, pp. 909-921, Mar./Apr. 2013.

[86] K. Ma and F. Blaabjerg, "Thermal optimized modulation method of three level NPC inverter for 10 MW wind turbines under low voltage ride through," *IET J. Power Electron.*, vol. 5, no. 6, pp. 920-927, Jul. 2012.

[87] P. Rodríguez, A. Luna, R. Muñoz-Aguilar, I. Etxeberria-Otadui, R. Teodorescu, F. Blaabjerg, "A stationary reference frame grid synchronization system for three-phase grid-connected power converters under adverse grid conditions," *IEEE Trans. Power Electron.*, vol. 27, no. 1, pp. 99-112, Jan. 2012.

[88] P. Rodriguez, A. V. Timbus, R. Teodorescu, M. Liserre, F. Blaabjerg, "Flexible active power control of distributed power generation systems during grid faults," *IEEE Trans. Ind. Electron.*, vol. 54, no. 5, pp. 2583-2592, Oct. 2007.

[89] Q. R. Tu, Z. Xu, Y. Chang, L. Guan, "Suppressing DC voltage ripples of MMC-HVDC under unbalanced grid conditions," *IEEE Trans. Power Del.*, vol. 27, no. 3, pp. 1332-1339, Jul. 2012.

[90] K. Ma, M. Liserre, F. Blaabjerg, "Reactive power control methods for improved reliability of wind power inverters under wind speed variations," in *Proc. ECCE*, pp. 3105-3112, 2012.

[91] A. Khlaief, M. Bendjedia, M. Boussak, M. Gossa, "A nonlinear observer for high-performance sensorless speed control of IPMSM drive," *IEEE Trans. on Power Electron.*, vol. 27, no. 6, pp. 3028- 3040, Jun. 2012.

[92] S. X. Du, J. J. Liu, T. Liu, "Modulation and closed-loop-based DC capacitor voltage control for MMC with fundamental switching frequency," *IEEE Trans. on Power Electron.*, vol. 30, no. 1, pp. 327-338, Jan. 2014.

Appendix

TABLE 1.1 SOME EXISTING OR PLANNED MMC-HVDC PROJECTS [5-16]

Project name	*Location*	*Power (MW)*	*DC voltage (kV)*	*AC voltage (kV)*	*Cable (km)*		*Commission time*	*Manufacture*
					Under sea	*Under ground*		
BorWin1	Germany	400	±150	Offshore: 156 Diele: 380	125	75	2009	ABB
Trans Bay Cable	US	400	±200	Pittsburg: 230 Portrero: 115	86	-	2010	Siemens
Nanhui	China	18	±30	Nanhui: 35 Shurou: 35	8	-	2011	State Grid Corporation of China
INELFE	France-Spain	2000	±320	Perpignan: 400 Figueras: 400	-	60	2013	Siemens
HelWin1	Germany	576	±250	Offshore: 155 Onshore: 250	85	45	2014	Siemens
SylWin1	Germany	864	±320	Dan Tysk: 155 Buttel: 380	160	45	2014	Siemens
Nanao	China	200	±160	Qingao: 110 Jinniu: 110 Sucheng: 110	32	-	2014	China Southern Power Grid
Zhoushan	China	400 300 100 100 100	±200	Dinghai:220 Daishan:220 Qushan:110 Yangshan:110 Sijiao:110	172.79	-	2014	State Grid Corporation of China
BorWin2	Germany	800	±300	Offshore: 155 Onshore: 400	125	75	2015	Siemens
DolWin1	Germany	800	±320	Offshore: 155 Dorpen: 155	75	90	2015	ABB
DolWin2	Germany	916	±320	Offshore: 155 Dorpen: 380	45	90	2015	ABB
HelWin2	Germany	690	±320	Offshore: 155 Buttel: 380	85	45	2015	Siemens
DolWin3	Germany	900	±320	Offshore: 155 Dorpen: 380	83	79	2017 (Expected)	Alstom

ISSN (online): 2246-1248
ISBN (online): 978-87-7112-567-2

AALBORG UNIVERSITY PRESS